

Fortschritt-Berichte VDI

VDI

Reihe 10

Informatik/
Kommunikation

Nr. 867

Dipl.-Math. techn. Aron Sommer,
Hannover

Backprojection Autofocus of Large Ships with Arbitrary Motion for Synthetic Aperture Radar



tnt

Institut für Informationsverarbeitung
www.tnt.uni-hannover.de

Backprojection Autofocus of Large Ships with Arbitrary Motion for Synthetic Aperture Radar

Von der Fakultät für Elektrotechnik und Informatik

der Gottfried Wilhelm Leibniz Universität Hannover

zur Erlangung des akademischen Grades

Doktor-Ingenieur

genehmigte

Dissertation

von

Dipl.-Math. techn. Aron Sommer

geboren am 7. November 1986 in Berlin

2019

Hauptreferent: Prof. Dr.-Ing. J. Ostermann
Korreferent: Prof. Dr.-Ing. J. Ender
Vorsitzender: Prof. Dr.-Ing. B. Rosenhahn

Tag der Promotion: 06. September 2019

Fortschritt-Berichte VDI

Reihe 10

Informatik/
Kommunikation

Dipl.-Math. techn. Aron Sommer,
Hannover

Nr. 867

Backprojection
Autofocus of Large
Ships with Arbitrary
Motion for Synthetic
Aperture Radar

tnt

Institut für Informationsverarbeitung
www.tnt.uni-hannover.de

Sommer, Aron

Backprojection Autofocus of Large Ships with Arbitrary Motion for Synthetic Aperture Radar

Fortschr.-Ber. VDI Reihe 10 Nr. 867. Düsseldorf: VDI Verlag 2019.

136 Seiten, 59 Bilder, 16 Tabellen.

ISBN 978-3-18-386710-3, ISSN 0178-9627,

€ 52,00/VDI-Mitgliederpreis € 46,80.

Keywords: Synthetic aperture radar (SAR) – inverse synthetic aperture radar (ISAR) – backprojection – fast factorized backprojection – imaging of moving objects – phase errors – autofocus – regularization – spotmode – stripmap-mode

Radar images of the open sea taken by airborne synthetic aperture radar (SAR) show typically several smeared ships. Due to their non-linear motions on a rough sea, these ships are smeared beyond recognition, such that their images are useless for classification or identification tasks. The ship imaging algorithm presented in this thesis consists of a fast image reconstruction using the fast factorized backprojection algorithm and an extended autofocus algorithm of large moving ships. This thesis analyzes the factorization parameters of the fast factorized backprojection algorithm and describes how to choose them near-optimally in order to reconstruct SAR images with minimal computational costs and without any loss of quality. Furthermore, this thesis shows how to estimate and compensate for the translation, the rotation and the deformation of a large arbitrarily moving ship in order to reconstruct a sharp image of the ship. The proposed autofocus technique generates images in which the ship type can be recognized, which was not possible by state-of-the-art autofocus techniques before.

Bibliographische Information der Deutschen Bibliothek

Die Deutsche Bibliothek verzeichnet diese Publikation in der Deutschen Nationalbibliographie; detaillierte bibliographische Daten sind im Internet unter www.dnb.de abrufbar.

Bibliographic information published by the Deutsche Bibliothek

(German National Library)

The Deutsche Bibliothek lists this publication in the Deutsche Nationalbibliographie (German National Bibliography); detailed bibliographic data is available via Internet at www.dnb.de.

© VDI Verlag GmbH · Düsseldorf 2019

Alle Rechte, auch das des auszugsweisen Nachdruckes, der auszugsweisen oder vollständigen Wiedergabe (Fotokopie, Mikrokopie), der Speicherung in Datenverarbeitungsanlagen, im Internet und das der Übersetzung, vorbehalten.

Als Manuskript gedruckt. Printed in Germany.

ISSN 0178-9627

ISBN 978-3-18-386710-3

VORWORT

Diese Dissertation habe ich während meiner Tätigkeit als wissenschaftlicher Mitarbeiter am Institut für Informationsverarbeitung der Gottfried Wilhelm Leibniz Universität Hannover verfasst.

Mein besonderer Dank gilt Herrn Prof. Dr.-Ing. Jörn Ostermann für seine engagierte Betreuung meiner Arbeit. Durch seine konstruktiven Anregungen und kritischen Fragen in fachlichen Diskussionen sowie durch seine freundliche Unterstützung hat er maßgeblich zur Realisierung dieser Arbeit beigetragen. Zudem möchte ich mich bei ihm für die hervorragenden Arbeitsbedingungen am Institut bedanken.

Herrn Prof. Dr.-Ing. Joachim Ender danke ich sehr herzlich für die fachliche Betreuung, seinen kritischen und anregenden Fragen sowie für die Übernahme des Korreferats. Für die Übernahme des Prüfungsvorsitzes bedanke ich mich bei Herrn Prof. Dr.-Ing. Bodo Rosenhahn.

Bei der Firma Hensoldt Sensors GmbH bedanke ich mich für die angenehme Zusammenarbeit sowie die Bereitstellung der Radardaten, die für die Entwicklung und die Evaluation der Algorithmen unabdingbar waren. Insbesondere gilt mein Dank Herrn Dr.-Ing. Martin Kirscht und Herrn Klaus Hoffmann für den förderlichen wissenschaftlichen Austausch und die konstruktive Zusammenarbeit mit Hensoldt Sensors GmbH und Airbus Defence and Space.

Frau Dr.-Ing. Ulrike Pestel-Schiller und Frau Dr.-Ing. Minh Phuong Nguyen danke ich sehr herzlich für die anregenden Gespräche und Diskussionen am Institut für Informationsverarbeitung.

Herrn Prof. Dr. Andreas Helfrich-Schkarbanenko danke ich dafür, dass er mich bei zukunftsweisenden Fragen strategisch beraten und unterstützt hat.

Mein Dank gilt darüber hinaus allen Kolleginnen und Kollegen am Institut für Informationsverarbeitung für die bereichernde Zeit und die ständige Hilfsbereitschaft. Für die technische sowie administrative Unterstützung möchte ich mich ausdrücklich bei den Administratoren und

den Mitarbeiterinnen und Mitarbeitern des Office bedanken.

Diese Dissertation wäre nicht ohne die Unterstützung meiner Freundin Ruth Schräder und meiner Eltern Gabriele Pfeiffer-Sommer und Günther Sommer sowie meinen Freunden möglich gewesen. Für das Mitleben und die erbrachte Geduld bedanke ich mich bei ihnen herzlich.

CONTENTS

1	INTRODUCTION	1
1.1	Synthetic Aperture Radar	2
1.2	Fast Factorized Backprojection	7
1.3	Autofocus of Large Ships	9
1.4	Structure of the Thesis	12
2	BASICS OF BACKPROJECTION IMAGE RECONSTRUCTION	13
2.1	Fundamentals of Synthetic Aperture Radar	13
2.2	Signal Model of a Static Scene	18
2.3	Global Backprojection	24
2.4	Image Quality Metrics	27
2.5	Backprojection Autofocus	31
2.6	Real Data Example	36
3	OPTIMIZATION OF FAST FACTORIZED BACKPROJECTION	40
3.1	Fast Factorized Backprojection	41
3.2	Computational Costs	44
3.3	Exact Range Error Computation	46
3.4	Image Error Estimation	51
3.5	Parameter Analysis and Optimization	53
3.6	Optimal Parameter Choice Rule	57
3.7	Experimental Results and Evaluation	59
3.7.1	Narrow Swath SAR using Gotcha data	60
3.7.2	Quinted SAR using SmartRadar data	69
4	AUTOFOCUS OF LARGE SHIPS WITH ARBITRARY MOTION	75
4.1	Ship Detection and Location Estimation	77
4.2	Signal Model of a Moving Ship	79
4.3	Effects of Arbitrary Motion on SAR Images	81
4.4	Optimal Focus Using True Motion	85
4.5	State-of-the-Art Autofocus of Ships	87
4.6	Extended Autofocus Algorithm of Large Ships	90
4.7	Experimental Results and Evaluation	97
4.7.1	Autofocus of a Large Tanker	98
4.7.2	Autofocus of a Large Bulk Carrier	101
4.7.3	Autofocus of a Self-Discharging Bulk Carrier	103
4.7.4	Autofocus of a Static Scene with Low-Cost INS	107
5	CONCLUSIONS	112
A	APPENDIX	117
	BIBLIOGRAPHY	119

ACRONYMS

ACC	Adaptive Cruise Control
ADC	Analog to Digital Converter
AIS	Automated Identification System
APC	Antenna Phase Center
ATC	Air Traffic Control
CFAR	Constant False Alarm Rate (Detector)
CPI	Coherent Processing Interval
DEM	Digital Elevation Map
FBP	Fast Factorized Backprojection
FFT	Fast Fourier Transform
FPGA	Field Programmable Gate Array
GBP	Global Backprojection
GMTI	Ground Moving Target Indication
GPS	Global Positioning System
ICBT	Image-Contrast-Based Technique
IMU	Inertial Measurement Unit
INS	Inertial Navigation System
ISAR	Inverse Synthetic Aperture Radar
ISLR	Integrated Side Lobe Ratio
PGA	Phase Gradient Autofocus
PPP	Prominent Point Processing
PRF	Pulse Repetition Frequency
PSLR	Peak Side Lobe Ratio
SAR	Synthetic Aperture Radar
UAV	Unmanned Aerial Vehicle
WGS84	World Geodetic System 1984

ABSTRACT

Radar images of the open sea taken by airborne *synthetic aperture radar* (SAR) show typically several smeared ships. Due to their non-linear motions on a rough sea, these ships are smeared beyond recognition, such that their images are useless for classification or identification tasks. The ship imaging algorithm presented in this thesis consists of a fast image reconstruction using the fast factorized backprojection algorithm and an extended autofocus algorithm of large ships with arbitrary motion.

In order to reconstruct a SAR image by the fast factorized backprojection algorithm with low computational costs and without any loss of quality, the factorization parameters must be set near-optimally. In this thesis, a rule for the choice of the factorization parameters is presented, which in the first step computes the exact range errors, which are the reason for the quality loss, instead of estimating them as in state-of-the-art rules. In the second step, the resulting maximum image error is estimated from the exact range errors. This precise estimation enables the evaluation of the factorization parameters with regard to the resulting costs and image quality before the algorithm is executed and thus to determine the near-optimal parameters. The evaluation using real X-band SAR data shows that the proposed parameter choice rule allows a significantly faster image reconstruction than current rules, where the resulting image quality loss is almost not visible.

This SAR image is used for the detection and the localization of all ships in the image. A local image is generated for each ship, which is smeared due to its non-linear motion on the rough sea. In order to compensate for the smearing and to reconstruct a sharp image, the developed autofocus technique estimates the motion of the ship and includes it into the reconstruction algorithm. For this motion estimation, the SAR image is divided into several subimages and a radial motion of each subimage, which maximizes image sharpness, is estimated. An iterative Gauss-Newton method is used for the estimation, which includes dependencies between the individual subimages by means of an additional regularization. This motion estimation of all subimages enables a robust estimation of the non-linear motion and deformation of a ship and a reconstruction of a sharp SAR image. It is shown by three real data examples that the presented autofocus technique provides significantly sharper images and better results than current SAR autofocus methods. State-of-the-art autofocus techniques lead to images in which the type of

the ship cannot be recognized. The proposed extended autofocus method provides SAR images where even the bollards on the deck of a large ship can be counted.

Additional experiments show that the developed autofocus technique is able to estimate and compensate large unknown changes in radial distance between the radar and the scene such that the use of expensive and highly accurate inertial navigation systems, which usually measure the flight path with high precision and thus enable the reconstruction of SAR images, is no longer necessary.

Keywords – Synthetic aperture radar (SAR), inverse synthetic aperture radar (ISAR), backprojection, fast factorized backprojection, imaging of moving objects, phase errors, autofocus, regularization, spotmode, stripmap-mode.

KURZFASSUNG

Radar-Luftbilder, welche mit einem flugzeuggestützten Radar mit synthetischer Apertur (engl. synthetic aperture radar (SAR)) über dem Meer aufgenommen wurden, zeigen typischerweise viele verschmierte Schiffe. Diese Schiffe werden wegen ihrer nichtlinearen Bewegungen bei rauer See bis zur Unkenntlichkeit verschmiert abgebildet, weswegen deren Bilder für eine Klassifikation, bzw. eine Identifikation unbrauchbar sind. Das in dieser Arbeit vorgestellte Autofokus-Verfahren besteht aus einer schnellen Bildgenerierung mittels Fast Factorized Backprojection Algorithmus und einer erweiterten Autofokussierung aller im SAR-Bild detektierten Schiffe.

Damit der Fast Factorized Backprojection Algorithmus ein SAR-Bild schnell und ohne hohen Qualitätsverlust generieren kann, müssen die Faktorisierungsparameter optimal eingestellt werden. In dieser Arbeit wird eine Regel zur Wahl der Faktorisierungsparameter vorgestellt, welche im ersten Schritt die für den Qualitätsverlust verantwortlichen Rangefehler exakt berechnet anstatt diese wie im Stand der Technik zu schätzen. Im zweiten Schritt wird der entstehende maximale Bildfehler auf Basis der exakten Rangefehler geschätzt. Durch diese präzise Schätzung können vor der Ausführung des Algorithmus die Faktorisierungsparameter bzgl. der entstehenden Kosten und der entstehenden Bildqualität bewertet und damit die optimalen Parameter ermittelt werden. Die Evaluation mittels realer X-Band SAR-Daten zeigt, dass die vorgeschlagene Regel eine deutlich schnellere Bildgenerierung als aktuelle Regeln zur Wahl der Faktorisierungsparameter ermöglicht, wobei die resultierenden Bildfehler fast nicht sichtbar sind.

Dieses deutlich schneller generierte SAR-Bild wird im weiteren Verlauf des vorgestellten Autofokus-Verfahrens für die Detektion und Lokalisierung der sich im Bild befindenden Schiffe verwendet. Pro Schiff wird nun ein lokales Bild generiert, welches aufgrund der nichtlinearen Schiffsbewegung bei rauer See stark verschmiert ist. Um diese Verschmierung zu kompensieren und ein scharfes Bild zu generieren, schätzt die erweiterte Autofokussierung die Schiffsbewegung und bezieht diese in den Rekonstruktionsalgorithmus mit ein. Im Rahmen dieser Bewegungsschätzung wird das SAR-Bild in mehrere Teilbilder unterteilt und für jedes Teilbild eine radiale Bewegung geschätzt, welche eine Bildschärfemetrik maximiert. Bei der Schätzung kommt ein iteratives Gauß-Newton Verfahren zum Einsatz, das mittels zusätzlicher Regularisierung Abhängigkeiten

zwischen den einzelnen Teilbildern miteinbezieht. Diese Bewegungsschätzung aller Teilbilder ermöglicht robust nichtlineare Bewegungen und Deformationen des Schiffes zu ermitteln und scharfe Bilder zu generieren. Anhand von drei Beispielen wird gezeigt, dass die vorgestellte Autofokussierung in realen Einsatzszenarien deutlich schärfere Bilder und bessere Ergebnisse liefert als aktuelle SAR-Schiffsautofokusverfahren. Aktuelle Autofokussierungsverfahren führen zu Bildern, bei denen der Typ des Schiffes nicht erkannt werden kann, wohingegen das entwickelte Verfahren SAR-Bilder liefert, in denen sogar die Poller an Deck eines großen Schiffes gezählt werden können.

Zusätzlich zeigen Experimente, dass die entwickelte Schiffs-Autofokussierung sogar in der Lage ist derartig große unbekannte Abstandsänderungen zwischen Radar und Szene zu schätzen und zu kompensieren, dass der Einsatz von teuren und hochgenauen inertialen Navigationssystemen, welche normalerweise die Flugbahn mit hoher Präzision messen und damit eine SAR-Bildgenerierung erst ermöglichen, nicht mehr notwendig ist.

Stichworte – Radar mit synthetischer Apertur (SAR), Inverses Radar mit synthetischer Apertur (ISAR), Backprojection, Fast Factorized Backprojection, Bildgebendes Verfahren für sich bewegende Objekte, Phasenfehler, Autofokussierung, Regularisierung, Spotmodus, Stripmap-Modus.

INTRODUCTION

Synthetic aperture radar (SAR) is a technique to generate radar images of the ground in all weather conditions and even by night. These days, SAR experiences a renaissance caused by the miniaturization and the improvement of hardware platforms together with the development of advanced signal processing algorithms over the last decade. Future applications and products seem to be possible that would have been inconceivable just a few years ago. Experts believe that SAR or especially radar sensors could be the dominating sensors in the near future. Radar sensors may replace optical sensors in autonomous vehicles and robots in extreme environments and for all weather conditions. However, autofocus algorithms are necessary for the reconstruction of sharp SAR images.

This thesis is an important contribution to the scientific research field of SAR autofocus algorithms. We propose an extended autofocus technique, which enables the reconstruction of sharp images of arbitrarily moving ships even on a rough sea with high waves. In addition, we show how to configure the *fast factorized backprojection* (FBP) algorithm [UHS03] in order to reconstruct large SAR images with low computational costs. Before going into detail, we begin this thesis with an introduction to radar and SAR as well as describe the problems, which are tackled by our proposals.

Heinrich Hertz¹ was the first scientist, who verified in 1886 the existence of electromagnetic waves in an experimental setup [Her87], proving the theory of James Clerk Maxwell², the inventor of the Maxwell equations [Max61]. The technology of radar, which is an acronym for *radio detection and ranging*, was invented by Christian Hülsmeier³ in 1904 in Germany. His system [Hüo4a; Hüo4b] used microwaves to measure the distance to a metallic object. The first commercial radar system was able to detect ships and airplanes in World War II. The same principle as in its early beginnings is used nowadays for example at airports to monitor the sky. Radar is a sensor, which measures distances to objects in a small angular view. It locates airplanes by transmitting an electromagnetic wave, i.e., a radar pulse, with a certain beamwidth in a certain direction. If the

¹ *February 22, 1857 in Hamburg, †January 1, 1894 in Bonn

² *June 13, 1831 in Edinburgh, †November 5, 1879 in Cambridge

³ *December 25, 1881 in Eydelstedt (Niedersachsen), †January 31, 1957, in Ahrweiler (Rheinland-Pfalz)

radar pulse hits an object, for example, an airplane, the antenna receives an echo after a short period of time. The distance between the antenna and the airplane can be calculated from the time difference between transmitting and receiving the pulse. By mechanically turning the radar around 360 degrees, the entire sky can be illuminated and the angular position of the airplane can be determined.

Especially in the last decade, the number of civil and military applications increased drastically. For example, airplanes are obliged to use the *air traffic control* (ATC) system, which consists of an onboard radar sensor to measure the distances to other airplanes in front of them for the sake of collision avoidance [Sti+14]. The same concept is used on ships and harbors to monitor their environment in bad-weather situations [Sch14]. Moreover, weather radars are used to detect and track clouds in the sky, to predict the type of precipitation and to do weather forecasting [RZ19]. However, the most common innovative radar application is autonomous driving. Such an autonomous vehicle uses a radar system to measure the distances to other cars in order to do *adaptive cruise control* (ACC), blind-spot monitoring and maybe 360 degrees environment monitoring in the future [Ber19].

The main advantage of radar is its capability to work reliably and independently from weather conditions, for example, by night, through rain, through fog and through clouds. Depending on their wavelength, the electromagnetic waves penetrate even thin materials like textiles as well as plastics and thin walls [Zha+18]. As a further advantage of radar, the resolution along line-of-sight depends only on the pulse-width of the electromagnetic wave and not on the distance to the illuminated object [CW05]. Hence, objects several thousand kilometers away from the sensor can be observed by only adjusting output power. Both advantages are reasons for the increasing number of radar applications.

Despite the broad use of radar applications, each system deals with the disadvantage of a poor angular resolution in far range, since the angular resolution on the ground depends on the beamwidth of the transmitted wave and on the range from the radar to the area of interest. For example, an electromagnetic wave with a beamwidth of one degree has a physical width of approximately 180 m in 10 km distance. Thus, a radar sensor cannot distinguish between two objects, which are close to each other and have the same distance to the radar.

1.1 SYNTHETIC APERTURE RADAR

Synthetic aperture radar is an advancement of traditional radar and solves lots of its problems. The technology of SAR has been invented

by the mathematician Carl A. Wiley⁴ in 1951 during his work at the Goodyear Aircraft Company in Arizona. The SAR principle enables the reconstruction of a radar image of an illuminated area like a landscape or a town and offers high angular resolution even in far range.

In contrast to optical sensors, SAR monitors wide areas in far range with high resolution independently of weather conditions. These advantages are reasons for the usage of SAR instead of optical cameras. Strictly speaking, cameras do not offer a wide-area coverage together with a high resolution in far range. Besides that, they do not work by night, through rain or through clouds. However, the temporal resolution is an advantage of optical cameras in comparison to radar sensors. An optical image can be taken within a fraction of a second, whereas SAR usually needs measurements from several seconds for the reconstruction of one single image. Furthermore, an optical image is always colored, whereas a radar image is often gray-scaled and visualizes only the reflectivity of materials.

Synthetic aperture radar has many civil and military applications. For example, satellites use multi-channel radar systems, which consist of multiple separated antennas, to measure the height of the earth's surface with a resolution of a few centimeters [Wes+18]. This technique is known as interferometry and yields a height profile of the earth, called a *digital elevation map* (DEM). At airports, full-body scanner equipped with small near-field SAR systems detect hidden firearms or metal objects for safety reasons [Mcm+09]. In maritime applications, SAR images are usually used to detect ships and to monitor the ship traffic on the open sea [Bru+11]. These are only a few applications of SAR, which are in most cases surveillance applications as well as remote sensing applications.

For this purpose, a side-looking radar is mounted on an airplane or a satellite, which flies along an almost straight flight path. This flight path is called *synthetic aperture*, which gives SAR its name and defines the *azimuth* direction as shown in Fig. 1.1. During the flight, the radar periodically transmits electromagnetic waves to measure the distances to all objects inside the illuminated area from different angles. Whenever an electromagnetic wave is transmitted, the current position of the antenna along the flight path is sampled. These discrete positions are called *aperture positions*. The sum of all echos from one transmitted electromagnetic wave measured at one aperture position is called *received data*. Applying the principle of *range compression* to the received data yields a *range profile*. The direction along line-of-sight is called *range* direction, see Fig. 1.1. All range profiles measured along the flight path

⁴ * December 30, 1918 in Princeton, New Jersey, † April 21, 1985 in Los Angeles

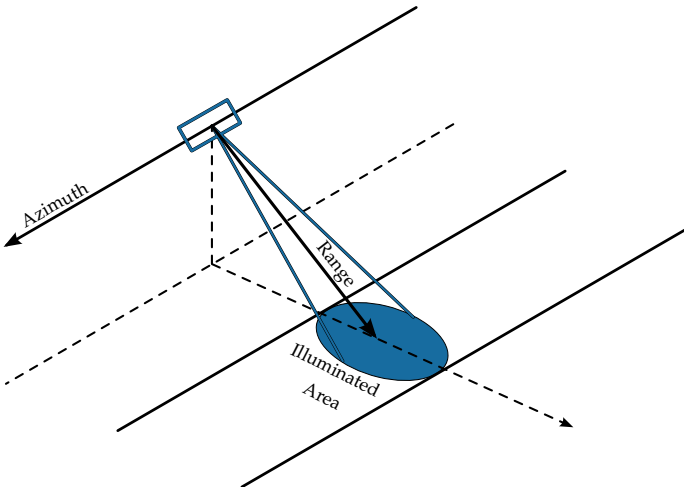


Figure 1.1: Visualization of side-looking radar geometry. This geometry describes the basic principal of SAR.

provide two-dimensional radar data instead of one-dimensional distance measurements from standard radar systems.

A SAR image reconstruction algorithm computes a radar image of the illuminated area from two-dimensional radar measurements. Such an image has, for example, a ground-resolution of 23 cm approximately 20 km away from the airborne sensor [Kir+16]. In the last decade, several SAR image reconstruction algorithms have been invented. Nowadays, two classes of algorithms are widely used: frequency-domain and time-domain algorithms. The Omega-K algorithm [CPR91] as the most common representative of the frequency-domain algorithms uses a two-dimensional *Fast Fourier transform* (FFT) to generate a radar image. Nevertheless, the Omega-K algorithm has a complexity of $O(N^2 \log N)$, where the radar image has $N \times N$ pixels and the synthetic aperture consists of N aperture positions. This algorithm is widely used to reconstruct radar images in real-time on special-purpose hardware [Pfi+13]. However, all frequency-domain algorithms can only process data measured along a perfectly straight flight path. Small deviations to this nominal track may be compensated by motion compensation techniques [NA13]. Curvy flight paths, where the maximal deviation to the nominal track is larger than 5 m, lead to poor image quality [SNO15]. Hence, Omega-K can only be used in

scenarios, where satellites or large airplanes with a stable flight carry the radar systems.

Nowadays, increasingly smaller SAR systems are mounted onto small aircrafts, drones or *unmanned aerial vehicles* (UAVs), which have non-stable and highly non-linear flight paths. In order to provide good image quality for arbitrary flight paths, the second class of image reconstruction algorithms has been invented, i.e., the time-domain algorithms. The most common time-domain algorithm is the *global backprojection* (GBP) algorithm [Faw85; And88; GM10]. This algorithm uses the flight path explicitly so that no additional motion compensation techniques are necessary. Even loops in the flight path are no problem for this algorithm [SO16]. Thus, it is suitable for platforms like drones or small UAVs, whose flight paths are exposed to wind gusts. Furthermore, the capability to reconstruct SAR images from data measured along arbitrary flight paths enables new SAR modes like the circular SAR scenario [Sou96], where an airplane flies along a circular trajectory around the area of interest. This capability is a good reason for the usage of the GBP algorithm, which works as follows: the N measured range profiles are projected from the corresponding aperture positions back to a predefined $N \times N$ grid on the ground. Accordingly, the computational costs are $O(N^3)$, which nowadays can not be processed in real-time for a standard 16 k by 16 k image. Such a reconstruction could take hours using a standard workstation [UHS03]. Nevertheless, this algorithm can be parallelized using, for example, a *field programmable gate array* (FPGA) [Cho+17]. We discuss in Chap. 3 how the computational costs of the image reconstruction algorithm can be reduced by the FBP algorithm [UHS03], while the image quality stays almost the same.

All image reconstruction algorithms, irrespective of whether they act in frequency- or in time-domain, need the true flight path to reconstruct a sharp image. To measure the flight path with high precision, very expensive *inertial navigation systems* (INSS) and *inertial measurement units* (IMUs) are used. Despite their high quality, these hardware systems have slight imperfections and provide noisy data with small errors like drifts. These errors are called *antenna position errors*. For example, a small antenna position error of 1 cm after the *observation time* of 10 s results in a loss of image quality [DL13] such that details in the SAR image are not visible anymore. Autofocus techniques have been invented in order to correct these image errors.

Traditionally, SAR is used to illuminate static scenes. However, a widely-used SAR application is maritime surveillance. Especially the monitoring of ship traffic, secure navigation, illegal activities and border control as well as the fight against piracy are typical maritime SAR applica-

tions [BMG16; Wat18]. For these applications, huge areas of the open sea are either be monitored regularly from space or instantly by airborne SAR sensors. Especially in airborne SAR images, moving ships appear usually smeared, because they are in motion during the observation time of several seconds [LDC14]. The reason for the smearing is the motion of the ship in azimuth-direction parallel to the flight path of the aircraft. The shift comes from the Doppler effect when the ship moves in range-direction directly to the radar sensor or away from the radar sensor along line-of-sight. Since a large ship has a specific size larger than a few meters, it is additionally deformed, which makes the situation even worse. Thus, in airborne SAR images, ships can often not be classified or even identified. This thesis was conducted to solve this problem.

For the identification of ships, the *automated identification system* (AIS) can be used. The AIS system is a wireless broadcast technology, where all ships transmit regularly information about their identity, their location and their destination using radio frequencies. However, illegal ships could turn off their AIS system or transmit fake information. Moreover, the transmitted AIS coordinates of the ship are not precise enough for SAR, since they do not transmit, for example, the rotations. Hence, a typical use case of airborne maritime SAR is the verification of AIS signals using high-quality SAR images of ships in all-weather conditions [Bru+11; Han+10].

This thesis proposes a ship imaging algorithm, which consists of two steps in order to reconstruct autofocus SAR images of large arbitrarily moving ships robustly in high quality. An overview of the concept is shown in Fig. 1.2. The first step of the ship imaging algorithm is the reconstruction of a SAR image of the entire illuminated area from single-channel raw data by the fast factorized backprojection algorithm [UHS03]. The advantage of this image reconstruction algorithm is its low computational costs in comparison to the GBP algorithm. Additionally, this algorithm has the capability to adjust the size and the number of pixels, which enables full flexibility and easy adjustments to the given applications. The reconstructed image is used to estimate the locations of all visible ships. We use a standard *constant false alarm rate* (CFAR) detector for the detection and localization of these ships because this part is not the main part of this thesis. The second step of the ship imaging algorithm consists of an extended autofocus algorithm of large ships. Based on the estimated locations of all detected ships and using the single-channel raw data, a local image of each ship is reconstructed by the GBP algorithm. The proposed autofocus technique is able to focus these images and to remove the smearings, since it estimates the motion of the ships and takes it into account during the image reconstruction process. The quality

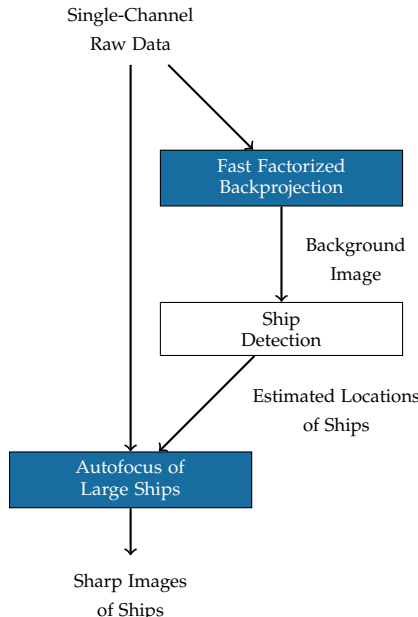


Figure 1.2: Flow diagram of proposed ship imaging algorithm. The blue boxes identify the contributions of this thesis.

of these images has to be good enough such that human expert SAR interpreters are able to classify the ships. In the following, we describe both steps, their problems, and our contributions in detail.

1.2 FAST FACTORIZED BACKPROJECTION

The first step of the proposed ship imaging algorithm, visualized in Fig. 1.2, is the reconstruction of the entire SAR image of an illuminated area from single-channel raw data using the FBP. In general, the illuminated area can be divided into two classes. On the one hand, the illuminated area may be a landscape with a ship driving along a river. In this case, the resolution of the entire SAR image has to be high with many small pixels, since every part of the image is of interest. On the other hand, the illuminated area may be the open sea with several ships. In this scenario, a low-resolution SAR image with less large pixels is enough to reconstruct an image, where all ships can be detected. The reduced

resolution saves a huge amount of computational time. However, the SAR image of the scene has to be reconstructed in both cases as fast as possible, since the faster the entire image is completely generated, the faster the ships can be detected. Hence, the used SAR image reconstruction algorithm should be flexible, such that the resolution and the quality of the image is adjustable during ongoing operation by only adapting some parameters in the algorithm. Additionally, it is desirable if all carrier platforms like drones or UAVs as well as all SAR modes like the stripmap, the spotmode or the circular SAR mode would be supported by only one algorithm. And of coarse, low computational costs is a must.

The fast factorized backprojection algorithm [UHS03] satisfies all of these requirements. It can be used in the case of curvy flight paths and for all SAR modes. Ulander et al. formulated the FBP algorithm [UHS03] as a generalized framework of different fast backprojection methods [MR96; Nil97; SHH98; Yeg99]. Each of these fast algorithms is a special case of the FBP and can be derived by using specific configurations. In order to decrease computational costs, the FBP algorithm combines similar neighboring range profiles, which contain approximately the same data. The number of combined range profiles is given by the *aperture factorization* parameters. This data combination process reduces the computational costs and causes *range errors*, which result in a loss of accuracy. To control the accuracy, the entire SAR image is divided into subimages, which again increases the computational costs. How often the image is divided into subimages is described by the *image factorization* parameter. The data combination process and the image division process is done iteratively in *stages*. The number of stages is critical because too many stages result in an increase in computational costs and besides that in a loss of accuracy. In order to reduce the run-time significantly and simultaneously guarantee small range errors and thus high image quality, the configuration of the FBP algorithm, i.e., the choice of the aperture factorization, the image factorization and the number of stages has to be near-optimal. However, these parameters can be variable in each stage such that the number of possible combinations is extremely large. Until today, no optimal solution of the parameter choice problem is known.

Some scientists give recommendations for useful factorization parameters. As the inventors of the FBP algorithm, Ulander et al. [UHS03] recommend using an aperture factorization of four in all stages. They additionally presented a rule to estimate the number of subimages in the first stage, which in general has to be large in order to minimize the range errors. However, their estimation is very conservative and overestimates the necessary number of subimages, which leads not to the fastest possible computation. Moreover, Ribalta [Rib12] analyzed the fac-

torization parameters as well and came to the conclusion that an aperture factorization of three in all stages optimizes the computational costs. He also presented a rule of how many stages are near-optimal. However, he considered the image quality and the computational costs separately, which are in general strongly related.

In this thesis, we aim to find a parameter choice rule for the factorization parameters of the FBP, which lead to minimized computational costs for a given image quality. To achieve this goal, we compute the exact range errors, which depend on the factorization parameters and cause the quality loss, instead of estimating them. Taking these exact range errors into account leads to a precise image quality estimation. This precise image quality estimation enables us to analyze many different factorization parameter constellations. Based on this parameter analysis, we derive a general rule, which leads to near-optimal factorization parameters. Experimental results with real data show that our estimated errors are closer to the true errors than state-of-the-art methods [UHS03; Rib12]. In summary, the proposed parameter choice rule, which takes the exact range errors into account, enables a fast reconstruction of the entire SAR image, where the image fulfills the quality requirements of the human operator.

With regard to this thesis, the FBP algorithm is used to reconstruct a large SAR image for example of the open sea with low computational costs in comparison to the GBP algorithm. This image is used to estimate the locations of all ships by a ship detector and to separate each ship from the others.

1.3 AUTOFOCUS OF LARGE SHIPS

The second step of our ship imaging algorithm shown in Fig. 1.2 is the ship autofocus step. Based on the output of the ship detector, the autofocus takes the locations of all detected ships and considers each ship on its own. For each arbitrarily moving ship an initial smeared SAR image, which contains the signature of only one ship, is reconstructed by the standard GBP algorithm from the single-channel raw data. The goal of the autofocus step is to remove the smearing in the image, such that in the end the ship is well focused and its class can be identified by a human operator or a SAR expert.

The reason why an arbitrarily moving ship is smeared, shifted and deformed is mainly its motion during the observation time of several seconds. Incidentally, the same problem exists when a picture is taken by an optical camera with a long exposure time. All static objects appear sharp in the picture, whereas moving objects are totally smeared and not

recognizable. In pictures only the smearing can be seen, whereas in SAR images a shift in azimuth direction and a deformation of large objects like ships occur in addition. The reasons for the smearing, the shift and the deformation can be explained in the following way: let us assume that a single point reflector moves with a constant velocity orthogonal to the flight path. Then, only the shift occurs, because the motion causes a linear frequency shift in data due to the Doppler effect and thus a shift in the SAR image. In other words, the distance from the orthogonally moving point reflector to the moving radar is the same as the distance from a shifted static point reflector to the moving radar. If this point reflector moves with a constant velocity parallel to the flight path, only the smearing occurs. The reason is that this parallel motion causes a quadratic frequency shift, which is actually a quadratic *phase error* and thus the smearing. If the point moves linearly in an arbitrary direction, both, the shift and the smearing occur. However, if for example the single point moves arbitrarily including accelerations, the reasons for the shift and the smearing can not be separated into azimuth- and range-motion anymore. If additionally, the moving object has a specific size instead of being a single point, the problem gets more complex. More complex means in this context that the object is additionally deformed. The reason is that, for example, in the case of a rotational motion the front of the ship has a different motion than the back of the ship and thus a slightly different shift in azimuth as well as a slightly different smearing.

In general, a ship moves in azimuth, in range and in height. It additionally turns around the pitch-, the roll- and the yaw-axis, which altogether are influenced by its velocity, its track and the sea waves. Furthermore, large ships are not rigid objects, since their deformations balance the forces from the sea waves. The arbitrary motion makes the autofocus problem of moving ships very complex.

In the literature, two different strategies to generate focused images of moving ships are well known. These strategies can be divided into *parametric* and *non-parametric* autofocus algorithms.

The parametric techniques model the phase errors as a time-dependent polynomial function [LDC14; NFM15; MBH05]. They use either the data or the unfocused image to estimate the coefficients of this mostly quadratic polynomial. This phase error function is then used to refocus the smeared image to improve its sharpness. Instead of estimating the phase errors, which come from object motion, some techniques estimate the motion parameters directly. Livingstone et al. [LDC14] estimate sine and cosine motions in the frequency-domain, which result in improvements of the SAR image quality. Noviello et al. [NFM15] estimate the Doppler parameters from the unfocused image to refocus it. Martorella et

al. [MBH05] estimate the model parameters of the motion by maximizing the image contrast, which is an indicator of the image quality.

The non-parametric autofocus strategies do not assume that the phase errors are modeled by a specific parametric function. Thus, arbitrary phase errors can be estimated and compensated. However, the estimated phase errors could have discontinuities.

The most common non-parametric autofocus methods are the *prominent point processing* (PPP) [CGM95] and the *phase gradient autofocus* (PGA) [HEGJJ89]. The PPP algorithm extracts the information of prominent points on a moving object from range-compressed data to estimate its motion parameters. The PGA algorithm uses prominent points, too. In contrast to the PPP, it benefits from the derivative property of the Fourier transform and computes the gradient of the phase to focus an unfocused image automatically. Another well-known non-parametric autofocus technique has been developed by Duersch et al. [DL13] for the GBP algorithm. Ash [Ash12] published an extension of this backprojection autofocus technique. Both find the motion parameters by optimizing an image sharpness metric, which means they reward pixels with high intensity. This backprojection autofocus by Duersch et al. [DL13] with the extension by Ash [Ash12] has the capability of focusing moving ships and will be discussed later in detail.

All of these parametric and non-parametric autofocus algorithms can only compensate linear motions and constant velocities. Hence, in the case of a smooth sea, these autofocus techniques yield sufficient results. However, if the sea is rough or if the azimuth resolution has to be increased by including data from a longer observation time, these classical autofocus techniques generate smeared images. The reason is that a non-linear motion yields phase errors, which depend on time and on the location of the pixel. A simple phase correction using one phase value per time sample for the entire image is no longer sufficient.

In this thesis, we propose an extended autofocus technique to reconstruct images of arbitrarily moving ships robustly with high quality. In contrast to others, we divide the image of a ship into subimages and estimate for each subimage its non-linear motion. Hence, for each subimage a phase error is estimated by maximizing image sharpness. Additionally, the algorithm forces the phase errors to be smooth between the subimages by using an iterative Gauss-Newton algorithm including a regularization technique. Thus, our autofocus algorithm is able to estimate and compensate time-dependent and location-dependent phase errors and thus arbitrary motions for example in the cases of a fast ship on a rough sea. This statement is confirmed by the evaluation of our proposed autofocus

technique of arbitrarily moving ships with simulated and experimental data.

1.4 STRUCTURE OF THE THESIS

Chap. 2 presents the concept of SAR. We begin this chapter with the description of the geometry, the data model, i. e., the process of taking radar measurements and the standard GBP algorithm, which generates a SAR image in Sec. 2.1 – 2.3. Several metrics to measure the resolution and the quality of such an image are given in Sec. 2.4 followed by an autofocus technique to improve the image quality in Sec. 2.5. This chapter ends with a real data example in Sec. 2.6.

In Chap. 3 the FBP algorithm and its computational costs are explained in detail. We compute the exact range errors and propose a new estimation of the maximal relative image error. The computational costs and the estimated image errors are discussed for different parameter constellations and several scenarios. A derived rule to choose the parameters optimally is presented. This chapter ends with two real data examples and the evaluation of the proposed parameter choice rule.

Chap. 4 shows how arbitrarily moving ships can be focused automatically. We begin this chapter with the description of a ship detector and show how their locations can be estimated in a SAR image. Afterwards, we extend the static signal model to the case, where one ship moves arbitrarily. We show the effects of different ship motions to SAR images generated by the standard GBP algorithm. That a sharp image of a moving ship can be reconstructed by taking the exact motion into account, is shown in Sec. 4.4. How state-of-the-art autofocus techniques estimate the motion of a ship is presented in Sec. 4.5. We propose an extended autofocus technique, which estimates one phase error per subimage and per pulse by maximizing subimage sharpness in Sec. 4.6. To demonstrate its robustness the proposed autofocus algorithm is evaluated with simulated and experimental data at the end of this chapter in Sec. 4.7. This thesis ends with the conclusions in Chap. 5.

2

BASICS OF BACKPROJECTION IMAGE RECONSTRUCTION

This chapter provides a detailed introduction to airborne *synthetic aperture radar* (SAR). All necessary definitions and further explanations for the understanding of this thesis are presented here. At the end of this chapter, the reader should know how radar data is mathematically described and how a sharp radar image is reconstructed from data using the backprojection autofocus technique by Ash [Ash12].

We begin this chapter with a brief introduction to SAR fundamentals including antenna phased arrays, SAR modes, flight paths described as space curves and the underlying geometries in Sec. 2.1. Afterwards, we explain in Sec. 2.2 which signal model is used and how the range compression leads to high range-resolution. The same section deals with the generalized signal model for arbitrary static scenes as well as with range filters for side-lobe suppression. Sec. 2.3 shows the concept, the equations and the implementation of the *global backprojection* (GBP) algorithm [And88]. How the quality of a reconstructed SAR image is measured is described in Sec. 2.4. An introduction to the backprojection autofocus technique by Ash [Ash12] is given in Sec. 2.5. Since all proposed algorithms are evaluated in this thesis using real experimental data, Sec. 2.6 shows experimental results of the GBP algorithm and of the autofocus by Ash. The description of the real airborne SAR system *SmartRadar* [Kir+16] is given in Sec. 2.6.

2.1 FUNDAMENTALS OF SYNTHETIC APERTURE RADAR

In airborne SAR, an airplane, which flies along an almost straight flight path, carries a radar sensor. The radar looks orthogonal to the flight direction and transmits periodically electromagnetic waves to the ground in order to illuminate a specific area from different angles. These electromagnetic waves are reflected by some objects on the ground or by the ground itself and reach the receiver after a short period of time. The sum of all measured echos is called *received data*. The *range compression* applied to the received data leads to the *range profile*. The range profile describes how strong the transmitted wave is reflected by objects in the

scene depending on its distances from the current radar position. Range profiles taken from various azimuth positions along the flight path contain information about the angular position of all scatterers. The azimuth resolution is specified by the following rule: the larger the processed angular interval, the higher is the resolution in azimuth. The size of the illuminated area and thus the maximal size of the reconstructed image depends mainly on the antenna radiation pattern and on the used SAR mode. Both are described in the following.

Most airborne radar systems use a patch antenna, which consists of multiple radiation elements to transmit and receive electromagnetic waves [Sti+14]. These radiation elements form a rectangular planar antenna with a specific height h_{apt} and length l_{apt} . The center of all elements is called *antenna phase center* (APC), which represents the entire antenna. This center is also called antenna reference point [CGM95]. A schematic representation of a rectangular planar antenna is shown in Fig. 2.1 (a).

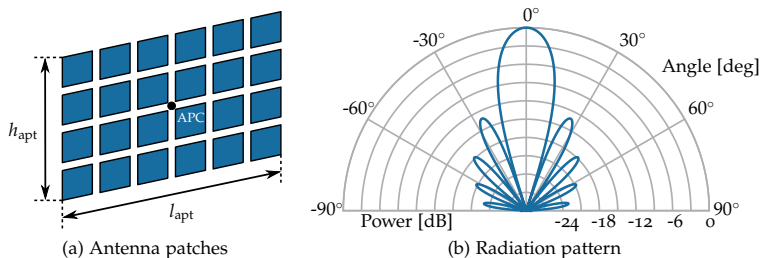


Figure 2.1: Characteristics of a phased array antenna.

However, the particular arrangement of all patches, or rather the height h_{apt} and the length l_{apt} of the rectangle, determine mainly the specific antenna radiation pattern. A typical antenna radiation pattern as well as the 3 dB beamwidth in azimuth is visualized in polar coordinates in Fig. 2.1 (b). The horizontal direction of the radiation pattern is called *azimuth* direction and the vertical direction is denoted by *elevation*. Especially the 3 dB azimuth beamwidth as well as the 3 dB elevation beamwidth define the edges of the antenna beam. At these edges, the power of the beam drops to -3 dB relating to the beam-center [Sti+14]. Both main lobe beamwidths can be approximately calculated by

$$\theta_{az} = \frac{0.886 \lambda}{l_{apt}} \quad \text{and} \quad \theta_{el} = \frac{0.886 \lambda}{h_{apt}},$$

where $\lambda = c/f_c$ is the wavelength, c the speed of light and f_c the carrier frequency of the electromagnetic wave [Sti+14; CW05]. However, an individually controlling of the transmitted and received phases of each radiation element adjusts the antenna beam and thus the 3 dB beamwidths θ_{az} and θ_{el} [Sti+14]. In practice, the beam pattern in elevation is often not considered or assumed to be constant for the illuminated area. Hence, the two-way beam pattern in azimuth, which governs the power of the received signal strength, is approximately a squared si-function [CW05]

$$E_{\text{ant}}(\theta) = \text{si}^2\left(\frac{0.886 \pi \theta}{\pi \theta_{az}}\right), \quad (2.1)$$

where the si-function is defined by $\text{si}(x) := \sin(x)/x$ for $x \in \mathbb{R} \setminus \{0\}$ and $\text{si}(0) := 1$. Here, the variable θ denotes the azimuth angle, where we assume that the look direction is orthogonal to the planar antenna and has zero degree. The physical antenna radiation pattern determines the radar *footprint* on the ground. It is often illustrated by an ellipse or a circle using the 3 dB beamwidth θ_{az} . An individual electrical control of the patch elements enables a steering of the antenna beam in a desired direction without using mechanically moving components. This development of the electrical beam steering enables a variety of SAR modes.

The two most common SAR modes are the *stripmap mode* [CW05] and the *spotmode* [CW05], see Fig. 2.2. In stripmap mode, the antenna has a permanent look direction orthogonal to the flight direction, such that its footprint moves uniformly over the ground. Altogether, the footprint illuminates a strip, which gives stripmap SAR its name. The advantage of the stripmap mode is the large illuminated area, whereas the resolution in azimuth is relatively low. The reason is that one point on the ground is illuminated only from a small angular section, which results in low resolution. In spotmode, a relatively small area of interest is illuminated from a large angular section. This can be done by electronically steering the antenna during the flight. Hence, the angular section is larger than in stripmap mode such that the resolution is higher.

Some other modes are for example the *scanning mode* and the *ground moving target indication* (GMTI) mode. In scanning mode, which is similar to the stripmap mode, the antenna look-direction varies in range to evaluate a wider strip. Moreover, the GMTI mode uses usually multiple channels of the antenna to separate the data, which contains information about moving objects from the data, which contains the static background. These four classical SAR modes are only a few of all modes mentioned in literature [Sti+14]. In general, it is desirable that the system is able to switch immediately from one mode to the other during the flight to

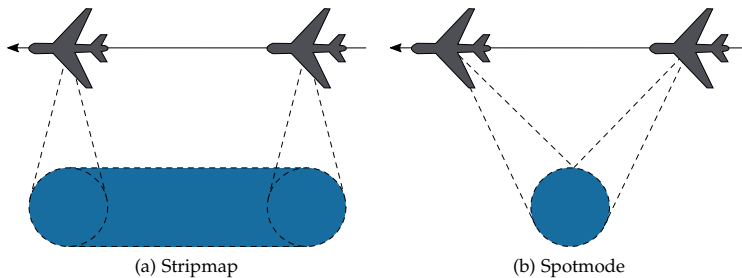


Figure 2.2: Visualization of the two classical SAR modes.

provide full flexibility. However, this thesis focuses mainly on the classical SAR modes, the stripmap- and the spotmode.

The concept of SAR requires a straight flight path. To realize this, the airplane tries to fly almost with constant velocity straight ahead, such that the APC follows exactly a straight line. This nominal track is described by a three-dimensional curve $\bar{\gamma} : \mathcal{L} \rightarrow \mathbb{R}^3$ in global Cartesian coordinates. This coordinate system has its origin at the center of the illuminated area on the ground. The space curve $\bar{\gamma}$ is parametrized by slow-time $s \in \mathcal{L}$ with $\mathcal{L} := [0, T_{\text{obs}}]$. The SAR observation time $T_{\text{obs}} \in \mathbb{R}_+$ corresponds to the length $L_{\text{obs}} \in \mathbb{R}_+$ of the synthetic aperture and defines how long the system takes measurements of the scene for one SAR image.

In practice, an airplane is not able to fly exactly along a straight line. Environmental circumstances like wind gusts or strong winds cause deviations to the nominal track $\bar{\gamma}$. These deviations are denoted by $\tilde{\gamma} : \mathcal{L} \rightarrow \mathbb{R}^3$, such that the true flight path is $\gamma = \bar{\gamma} + \tilde{\gamma}$. Since all image reconstruction algorithms need the true flight path γ exactly including all curvy deviations to compute a sharp image, the track has to be measured with high precision. Typically, a *global positioning system* (GPS) and an *inertial navigation system* (INS) equipped with an *inertial measurement unit* (IMU) are mounted next to the antenna to measure the true flight path. The GPS provides coarse global positions of the APC, whereas the IMU measures the local curvy track precisely. Despite their high quality, these IMUs exhibit small measurement errors due to hardware imperfections. For the observation time T_{obs} of several seconds, these small errors accumulate and result in deviations and drifts of up to a few centimeters [DL13]. We denote the accumulated

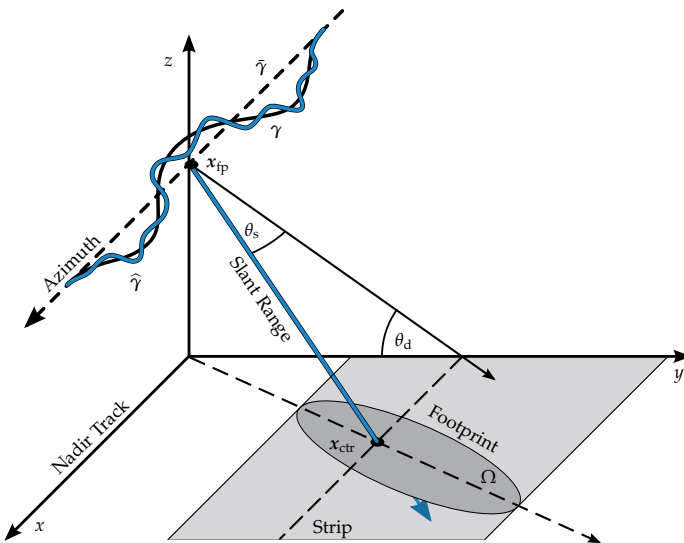


Figure 2.3: Geometry of stripmap SAR scene.

measurement errors of the IMU by the *antenna position error* $\gamma^\epsilon : \mathcal{L} \rightarrow \mathbb{R}^3$, such that the measured flight path

$$\hat{\gamma}(s) = \underbrace{\bar{\gamma}(s) + \tilde{\gamma}(s)}_{=\gamma(s)} + \gamma^\epsilon(s)$$

is available for all $s \in \mathcal{L}$ for further computations. The curve $\hat{\gamma}$ is also called estimated flight path. Usually, the GPS measurements have to be transferred from the *World Geodetic System 1984* (WGS84) to Cartesian coordinates. How the antenna position errors of the INS are estimated and corrected is discussed in Sec. 2.5.

In the following, we present the basic geometry of a standard stripmap scenario and some elementary definitions visualized in Fig. 2.3. The nominal flight path $\bar{\gamma}$ defines the azimuth direction. Its orthogonal projection on the ground is called *nadir track*. Fig. 2.3 also depicts the true flight path γ and the measured flight path $\hat{\gamma}$. The center of the nominal flight path, located at x_{fp} , is called *flight path center* and serves as the reference point of the entire flight path. The x -, y - and z -axis of the global Cartesian coordinate system are defined by the azimuth direction, the ground plane and the height axis, respectively. The origin of the Cartesian coordinate system is located at the center x_{ctr} of the entire strip. In a

spotlight scenario, this center is called *spot center*. The squint angle θ_s describes basically how far the antenna steers to the front with respect to the orthogonal side-look direction, see Fig. 2.3. The depression angle θ_d is mainly the incident angle of the transmitted electromagnetic wave with respect to the ground plane. The further away the antenna looks, the lower is the depression angle. The direction from x_{fp} to x_{ctr} is called *slant range* direction, whereas its orthogonal projection on the ground is called *ground range* direction. Frequency-domain algorithms reconstruct images in the slant range plane, which is spanned by the azimuth direction and the slant range direction, whereas the GBP algorithm reconstructs images on the ground. The union of all areas on the ground, which are illuminated by at least one beam during the observation time, is denoted by $\Omega \subset \mathbb{R}^3$. We describe the surface Ω by three dimensions such that the topography of the ground can be taken into account. The reflectivity function $\mathcal{R} : \Omega \rightarrow \mathbb{C}$ lives on the surface Ω and models how strong the electromagnetic waves are reflected by all objects on the ground or by the ground itself.

2.2 SIGNAL MODEL OF A STATIC SCENE

We explain in this section the radar signal model by considering at first only one perfect point reflector and a static antenna. Afterwards, we generalize this signal model to arbitrary scenes, moving antennas and arbitrary reflectivities.

Let us assume that the APC is located at x_{fp} and one infinitesimal small perfect point reflector is located at x_{ctr} . The antenna transmits a short electromagnetic pulse and receives its echo after the two-way round-trip time $\tau = 2/c \cdot \|x_{fp} - x_{ctr}\|_2$, where c is the speed of light. The pulse-width of the transmitted pulse defines the resolution of the radar system. In order to obtain high range-resolution, the radar should transmit a very short pulse with an extremely high peak power, which is technically spoken difficult to implement.

To avoid transmitting a small pulse-width with high output power, all high-end radar-systems use the principle of *range compression*, also known as *pulse compression*. The range compression utilizes the fact that the auto-correlation of a frequency modulated chirp-pulse is approximately a si-function with a significantly smaller width of its main lobe in comparison to the pulse-width itself. This is known as *matched-filter*, which achieves additionally maximal signal-to-noise ratio. The principle of range compression can be applied to any kind of frequency modulated signals. However, we focus in this thesis on linear frequency-modulated signals, because they are used in many classic radar applications. Such

a linear frequency modulated chirp-pulse, which is transmitted by the antenna, is described for $t \in \mathbb{R}$ by the signal [CW05]

$$p(t) = \text{rect}\left(\frac{t}{T}\right) \exp(2\pi i f_c t) \exp(i\pi\kappa t^2), \quad (2.2)$$

where rect is the rectangular function, i the imaginary unit, f_c the carrier frequency, $\kappa = B/T$ the chirp rate with the chirp bandwidth B and the pulse duration T . The signal in Eq. (2.2) is composed of a rectangular pulse with a width of T , a modulation by the carrier-frequency f_c and a linear frequency modulated chirp. Scattered at the perfect point reflector, the electromagnetic wave p reaches the receiver after the two-way round-trip time τ . The delayed echo

$$s_{\text{rec}}(t) = \text{rect}\left(\frac{t-\tau}{T}\right) \exp(2\pi i f_c(t-\tau)) \exp(i\pi\kappa(t-\tau)^2) \quad (2.3)$$

is for $t \in \mathcal{T}$ measured within the sampling time interval \mathcal{T} , also known as fast-time interval, and has high frequency components. The signal s_{rec} is sampled down to its baseband representation by a hardware mixer and a low-pass filter, which is mathematically described by a modulation, such that

$$\begin{aligned} s_{\text{raw}}(t) &= s_{\text{rec}}(t) \cdot \exp(-2\pi i f_c t) \\ &= \text{rect}\left(\frac{t-\tau}{T}\right) \exp(-2\pi i f_c \tau) \exp(i\pi\kappa(t-\tau)^2) \end{aligned} \quad (2.4)$$

is the received baseband signal called *raw signal*. The raw signal s_{raw} is sampled by an *analog to digital converter* (ADC) with a sampling frequency $f_s > B$ to fulfill the sampling theorem and the Nyquist criterion. In practice, a sampling frequency of $f_s = B$ is sufficient, since *range windows*, which are described later in this section, suppress range ambiguities. To get high resolution, the concept of range compression is applied in software. A cross-correlation of the received signal s_{raw} with the discretized baseband reference chirp $p_{\text{ref}}(t) = \text{rect}\left(\frac{t}{T}\right) \exp(i\pi\kappa t^2)$ leads to the range-compressed signal

$$\begin{aligned} s_d(t) &= s_{\text{raw}}(t) * p_{\text{ref}}^*(-t) \\ &\approx \text{si}(\pi B(t-\tau)) \exp(-2\pi i f_c \tau) \end{aligned} \quad (2.5)$$

of a perfect point reflector. The operation $*$ denotes the convolution and $(\cdot)^*$ is the complex conjugation. The principle of stationary phase leads to the approximation of the range-compressed data in terms of si-functions in Eq. (2.5). The signal s_d and especially the peak of the si-function provide information about the distance from x_{fp} to x_{ctr} . This clarifies why the signal s_d was introduced before as range profile. The

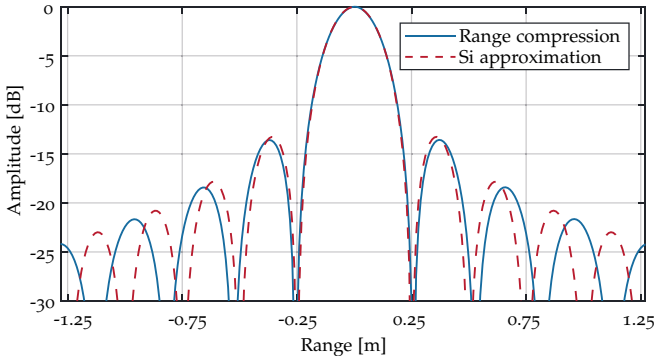


Figure 2.4: Approximation of envelope/point spread function as si-function. The blue curve is the envelope of the original range-compressed signal and the red dashed function represents the si-approximation. Their main lobes and their two side lobes coincide well.

3 dB width of the main lobe of the si-function in Eq. (2.5) defines the range-resolution

$$\delta_r = \frac{c}{2B}.$$

Moreover, Fig. 2.4 shows that the approximation of the point spread function by a si-function is very good, since often only the main lobe and one or two side lobes are visible in the resulting SAR image. However, the si-approximation is used in this thesis only for visualization. In the digital SAR processor, the range compression is implemented by the matched filter without approximations. In the following, we extend the signal model of a static antenna and a single reflector to the general case of a moving antenna and arbitrary reflectivity functions.

Let us assume that the aircraft flies along an arbitrary flight path such that the APC follows γ . The radar antenna transmits periodically chirp pulses p described by Eq. (2.2) with a *pulse-repetition frequency* f_{prf} to illuminate the ground from different angles. The illuminated area $\Omega \subset \mathbb{R}^3$, specifically each coordinate $x \in \Omega$, models the ground surface. This ground surface is the support of the complex reflectivity function $\mathcal{R} : \Omega \rightarrow \mathbb{C}$, which characterizes how strong the electromagnetic waves are reflected at each $x \in \Omega$. The part of the area Ω , which is currently illuminated by the antenna, is described by the antenna footprint function $F_{\text{ant}} : \Omega \times \mathcal{L} \rightarrow [0, 1]$, which depends on slow-time $s \in \mathcal{L}$ and includes the

two-way antenna radiation pattern from Eq. (2.1). The antenna footprint is modeled by

$$F_{\text{ant}}(\mathbf{x}, s) = \text{si}^2 \left(\frac{0.886 \pi \theta_{\text{rel}}(\gamma(s), \mathbf{x}_{\text{ant}}(s), \mathbf{x})}{\pi \theta_{\text{az}}} \right),$$

where θ_{az} is the 3 dB azimuth beamwidth of the antenna and

$$\theta_{\text{rel}}(\gamma(s), \mathbf{x}_{\text{ant}}(s), \mathbf{x}) = \arccos \left(\frac{(\mathbf{x}_{\text{ant}}(s) - \gamma(s))^T (\mathbf{x} - \gamma(s))}{\|\mathbf{x}_{\text{ant}}(s) - \gamma(s)\|_2 \|\mathbf{x} - \gamma(s)\|_2} \right)$$

the relative look angle to the antenna pointing $\mathbf{x}_{\text{ant}} : \mathcal{L} \rightarrow \Omega$ [Sti+14]. Here, $(\mathbf{x}_{\text{ant}}(s) - \gamma(s))$ for $s \in \mathcal{L}$ is the instantaneous look direction from the aperture position $\gamma(s)$ to the antenna pointing $\mathbf{x}_{\text{ant}}(s)$ on the ground and $(\mathbf{x} - \gamma(s))$ is the current vector from the aperture to the coordinate \mathbf{x} . We derive the generalized signal model similar to Cheney [CB09] by using the principle of superposition. The measured data consist of the superposition of all time-delayed echos from Eq. (2.3) and is described by

$$d_{\text{rec}}(t, s) = \int_{\Omega} F_{\text{ant}}(\mathbf{x}, s) \mathcal{R}(\mathbf{x}) p(t - 2/c \cdot \|\gamma(s) - \mathbf{x}\|_2) d\mathbf{x} \quad (2.6)$$

for $t \in \mathcal{T}$ and $s \in \mathcal{L}$. Following the procedure explained above, the data d_{rec} is sampled down to its baseband resulting in the raw data

$$d_{\text{raw}}(t, s) = d_{\text{rec}}(t, s) \cdot \exp(-2\pi i f_c t). \quad (2.7)$$

An ADC samples the raw data and forwards it to the digital SAR processing unit, where all digital algorithms are implemented.

The first step in the digital processing chain is the range compression. As described above, the sampled raw data is matched filtered and results in the range-compressed data [CW05]

$$d(t, s) = d_{\text{raw}}(t, s) * p_{\text{ref}}^*(-t) \quad (2.8)$$

$$\approx \int_{\Omega} F_{\text{ant}}(\mathbf{x}, s) \mathcal{R}(\mathbf{x}) \text{si}(\pi B(t - 2/c \cdot \|\gamma(s) - \mathbf{x}\|_2)) \\ \cdot \exp(-4\pi i f_c / c \cdot \|\gamma(s) - \mathbf{x}\|_2) d\mathbf{x} \quad (2.9)$$

for $t \in \mathcal{T}$ and $s \in \mathcal{L}$. We implement the range compression according to Eq. (2.8). However, the principle of stationary phase applied to Eq. (2.8) yields a better understanding of the range-compressed data approximated by si-functions visualized in Eq. (2.9). Fig. 2.5 visualizes the two-dimensional range-compressed data for the simple case of one perfect point reflector. Each column of the two-dimensional range-compressed

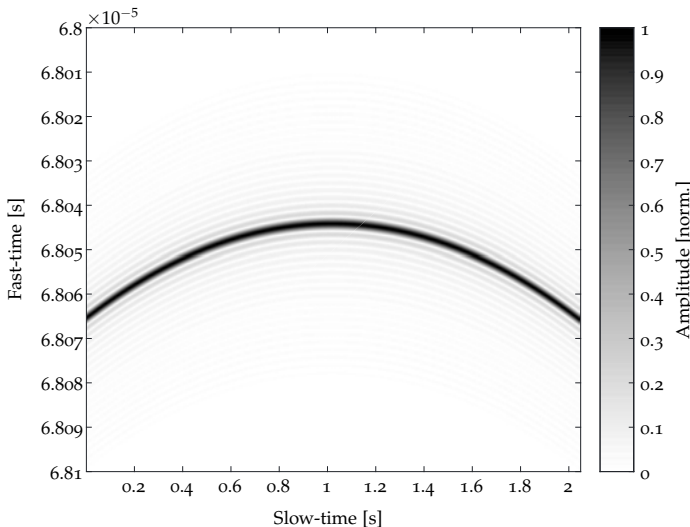


Figure 2.5: Range compressed data d of a perfect point reflector. The data is stored in a matrix. The range-migration can be seen.

data matrix is a range profile. The varying distance from the APC to the perfect point reflector on the ground is called *range-migration* and can clearly be seen in Fig. 2.5. Eq. (2.8) and its visualization in Fig. 2.5 illustrate the entire process of taking SAR measurements in the noiseless case.

In practice, the raw data is overlaid by noise. In radar applications, typically two noise sources are considered. The first one is standard thermal noise in hardware components, which is modeled by complex Gaussian white noise. The second is the speckle noise, which can typically be seen in radar images. The speckle noise comes from constructive and destructive interferences of electromagnetic waves, because they are scattered at a surface, which is rough in comparison to the wavelength. Similar interferences are caused by the existence of multiple scatterers inside a single image cell, which also leads to the speckle noise in radar images.

To reduce the speckle in SAR images as well as the noise in radar measurements, the range-compressed data is usually low-pass filtered. In the literature, two different filters are mainly used: the Kaiser window and the Taylor window. The Kaiser window [CW05] with a parameter of $\beta = 2.5$ offers a good compromise between sidelobe suppression and

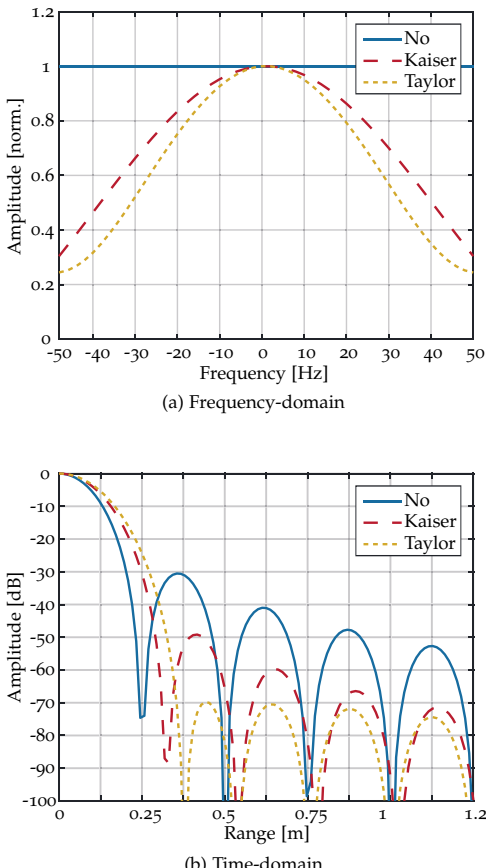


Figure 2.6: Low-pass filter in range compression. The blue line corresponds to the original range-compressed signal. The yellow dotted line shows the side lobe suppression and the main lobe broadening of the Taylor window. The red dashed line is a good compromise using the Kaiser window.

main lobe broadening. The Taylor window [CGM95] provides strong, selectable sidelobe suppression with a minimum broadening of the main lobe. Typical values for the Taylor window are $n = 4$ with $SLL = -30$ dB and $n = 5$ with $SLL = -35$ dB. Both, the Kaiser window and the Taylor window are visualized in Fig. 2.6.

2.3 GLOBAL BACKPROJECTION

The *global backprojection* (GBP) algorithm, which has been invented by Andersson [And88], is an image reconstruction technique to reconstruct a SAR image from range-compressed data. It is the most common time-domain algorithm and was originally used for computed tomography image reconstruction [Nato01] before it was applied to SAR.

The main advantage in comparison to frequency-domain algorithms is its ability to work with arbitrary flight paths. No additional motion compensation is necessary. Thus, the algorithm enables the usage of platforms with non-linear flight paths like UAVs. Another advantage of the GBP algorithm is its ability to project the data directly onto an irregular image grid, onto three-dimensional voxels or onto the topography of a landscape named *digital elevation model* (DEM). The algorithm can easily be adapted to non-static image grids like time-depending moving and deforming grids. The main disadvantage of the GBP is its high computational costs of $O(N^3)$, where N measured range profiles are projected onto an image with $N \times N$ pixels. One way to reduce computational time is to reconstruct only a relatively small image or to parallelize the computations using, for example, a *field programmable gate array* (FPGA) [Cho+17]. In Chap. 3 we discuss a fast backprojection variant, which speeds-up the algorithm by using approximations.

In detail, the GBP algorithm projects the M measured range profiles from the M aperture positions back to a predefined $N_x \times N_y$ image grid on the ground as shown in Fig. 2.7. All range profiles are sequentially processed and accumulated coherently in image-domain. With an increasing number of backprojected range profiles, the reflectivity at a pixel of a true target sums up more significantly than the reflectivity at a pixel without a target. A non-coherent processing would result in very poor azimuth resolution because the main information is in the phase.

In the initialization of the algorithm, an image grid is defined on the ground. Its center is often the origin of the global Cartesian coordinate system, i.e., the spot center. All $N_{\text{pix}} = N_x \cdot N_y$ pixels are represented by their center coordinates $x_i \in \Omega$ for $i = 1, \dots, N_{\text{pix}}$. The observation time interval \mathcal{L} is sampled with PRF resulting in M slow-time samples s_1, \dots, s_M . Similarly, the flight path γ is discretized. Thus, the aperture positions $\gamma_m := \gamma(s_m)$ are available in global coordinates for $m = 1, \dots, M$.

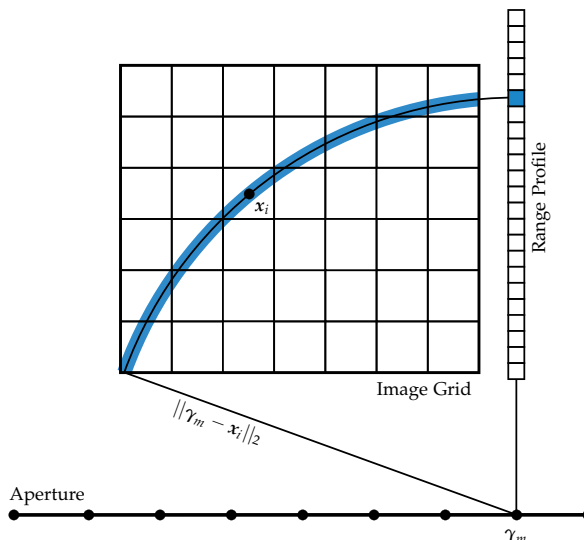


Figure 2.7: Backprojection of one range profile from the aperture position γ_m back to the image grid on the ground, especially on the pixel located at x_i .

The core of the GBP algorithm, the backprojection of the range-compressed data, can be mathematically described by one single equation. The complex valued reflectivity \mathcal{R} of a pixel at x_i is reconstructed by

$$\mathcal{R}(x_i) = \sum_{m=1}^M d_m (2/c \cdot \| \gamma_m - x_i \|_2) \cdot \exp(4\pi i f_c/c \cdot \| \gamma_m - x_i \|_2). \quad (2.10)$$

This has to be done for all $i = 1, \dots, N_{\text{pix}}$ pixels. The range-compressed data d , especially each range profile $d_m := d(\cdot, s_m)$ is projected for $m = 1, \dots, M$ from the corresponding aperture position γ_m back to all pixels x_i on the ground. Therefore, the distances $\| \gamma_m - x_i \|_2$ for $m = 1, \dots, M$ and $i = 1, \dots, N_{\text{pix}}$ have to be computed and transferred to the two-way round-trip time by multiplying them by the factor $2/c$.

In order to obtain the value $d_m (2/c \cdot \| \gamma_m - x_i \|_2)$ for a specific m and a specific i , we have to interpolate the data d_m , since it is discrete in practice, compare Fig. 2.7. We usually use linear interpolation. Nevertheless, other kinds of interpolations are possible. The interpolated data has to be transferred back to its high frequency band by multiplying d_m by an

exponential term. The sum of all M range profiles yields the reflectivity $\mathcal{R}(x_i) \in \mathbb{C}$ for $i = 1, \dots, N_{\text{pix}}$.

The complex valued reflectivity image \mathcal{R} is difficult to interpret. Thus, the image is often described by its real valued amplitude $\mathcal{A} = |\mathcal{R}|$ together with its real valued phase $\mathcal{P} = \arg(\mathcal{R})$. In principle, the amplitude image contains the main information, whereas the phase is usually not considered. Since the dynamic range of a SAR image is very large, the amplitude is usually visualized in decibel. Another frequently used real valued representation is the intensity image $\mathcal{I} = \mathcal{A}^2 = \mathcal{R} \cdot \mathcal{R}^*$, which is the power of the reflectivity.

In literature, the filtered backprojection [Nato1; DBM16] algorithm is often used for airborne SAR applications. It uses a ramp filter to weight linearly the amplitude of the data depending on the range. The purpose of this weighting procedure is to compensate the decreasing azimuth resolution with increasing range. Since at near-range the samples are closer together than at far-range, the amplitude of a reflector spreads over more pixels in far-range [DBM16]. The ramp filter does not compensate the range-depending loss in signal strength of an electromagnetic wave. This filter is important in near-filed applications. However, it has usually no visible effects in airborne SAR images and can be neglected [DBM16].

Table 2.1: Pseudocode of the GBP algorithm [And88; GM10].

Algorithm in pseudocode

Input: d, γ, Ω

Output: \mathcal{A}

- 01: Initialize image pixel grid $x_i \in \Omega$ for all $i = 1, \dots, N_{\text{pix}}$
- 02: Initialize reflectivity image $\mathcal{R}(x_i)$ for all $i = 1, \dots, N_{\text{pix}}$ with zeros
- 03: **for** each slow-time sample m **do**
- 04: **for** each pixel i **do**
- 05: Get distance $r_{m,i} = \|\gamma_m - x_i\|_2$ from γ_m to x_i
- 06: Interpolate range profile $d_m(\cdot)$ to sample $d_{m,i} = d_m(2/c \cdot r_{m,i})$
- 07: Get phase modulation $p_{m,i} = \exp(4\pi i f_c / c \cdot r_{m,i})$
- 08: Accumulate image $\mathcal{R}(x_i) = \mathcal{R}(x_i) + d_{m,i} \cdot p_{m,i}$
- 09: **endfor**
- 10: **endfor**
- 11: Compute Amplitude $\mathcal{A} = -20 \log_{10} |\mathcal{R}|$ in dB
- 12: **return** amplitude image \mathcal{A}

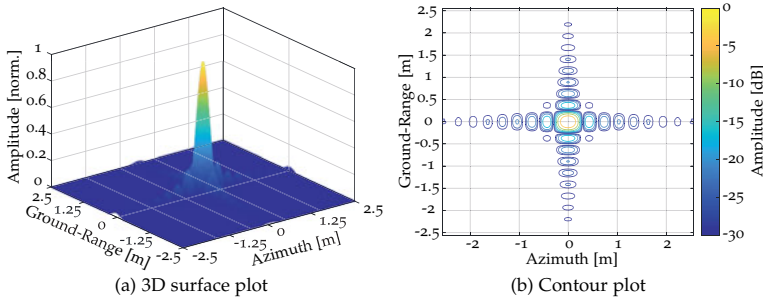


Figure 2.8: SAR image of perfect point reflector.

Our Matlab implementation of the GBP algorithm is based on Gorham's implementation [GM10]. The implementation of the GBP algorithm is written in pseudocode in Tab. 2.1. For visualization, a perfect image response, i.e., the point spread function of a perfect point reflector is shown in Fig. 2.8. The typical two-dimensional si-function can clearly be seen in the figure. Such an image response of a point reflector is usually used to evaluate the quality of a SAR image and the reconstruction algorithm as well.

2.4 IMAGE QUALITY METRICS

The output of every SAR image reconstruction algorithm is a complex-valued reflectivity image \mathcal{R} . To measure its quality, several technical metrics are widely recommended in literature [MM93]. All of these image quality metrics help to evaluate and compare SAR image reconstruction algorithms.

In the case of simulated data or if real data of a corner reflector is available, the *integrated side lobe ratio* (ISLR) and the *peak side lobe ratio* (PSLR) can be applied for this purpose [MM93]. In both metrics, the reconstructed image is compared with an optimal signal response of a perfect point reflector to identify quality degradations. Both metrics can also be used to verify if a reconstruction was successful. Furthermore, the *peak power*, the *image sharpness*, the *image contrast* and the *image entropy* indicate the quality of a SAR image reconstructed from real data. The actual values of these metrics depend highly on the content of the image itself. That is why these metrics are used to compare different image reconstruction algorithms and to identify which algorithm leads to the sharpest image using the same data. Moreover, if one image is chosen to

be the reference image, the *maximal relative image error*, which measures the maximal amplitude difference to the reference image, can be used. In the following, we explain each metric in detail.

Integrated Side Lobe Ratio

The *integrated side lobe ratio* (ISLR) characterizes the ratio between the intensity of the area under the main lobe and the intensity of the area under the side lobes along azimuth, see Fig. 2.9(a). It is defined by

$$\text{ISLR} = 10 \log_{10} \left(\frac{\bar{\mathcal{I}}(-20 \delta_{az}, -\delta_{az}) + \bar{\mathcal{I}}(\delta_{az}, 20 \delta_{az})}{\bar{\mathcal{I}}(-\delta_{az}, \delta_{az})} \right),$$

where δ_{az} is the system resolution in azimuth and

$$\bar{\mathcal{I}}(a, b) = \int_a^b |\mathcal{R}((x_0 + x, y_0, z_0)^T)|^2 dx$$

the mean intensity between a and b along one azimuth line. The coordinate $x_0 = (x_0, y_0, z_0)^T$ is the location of the peak amplitude. This metric considers only the image quality degradation in azimuth direction. This is useful, since whenever an image is smeared, it is smeared in azimuth. However, the ISLR metric can be directly applied in range direction or in a two-dimensional manner. Further readings and extended metrics can be found in the report of Martinez [MM93]. A perfect point reflector has an ISLR value of -9.8 dB [KH99]. In the case of side-lobe suppression in azimuth direction using a Kaiser window, which suppresses the speckle and broadens the main lobe, see Sec. 2.2, the ISLR value is -18.2 dB [CW05].

Peak Side Lobe Ratio

The *peak side lobe ratio* (PSLR) compares characteristics of an reconstructed point reflector along one azimuth line with the theoretical optimum. In contrast to the ISLR, it measures the ration between the maximal peak power of the main lobe $\mathcal{I}_{\text{main}}$ and the maximal peak power of the first side lobe $\mathcal{I}_{\text{side}}$ in decibel. It is defined by

$$\text{PSLR} = 10 \log_{10} \left(\frac{\mathcal{I}_{\text{side}}}{\mathcal{I}_{\text{main}}} \right).$$

Both power values are visualized in Fig. 2.9(b). This metric can be extended to the range direction and to the two-dimensional case. Perfect values are -13.2 dB [KH99] without any side lobe suppression and -21.0 dB [CW05] applying the Kaiser window.

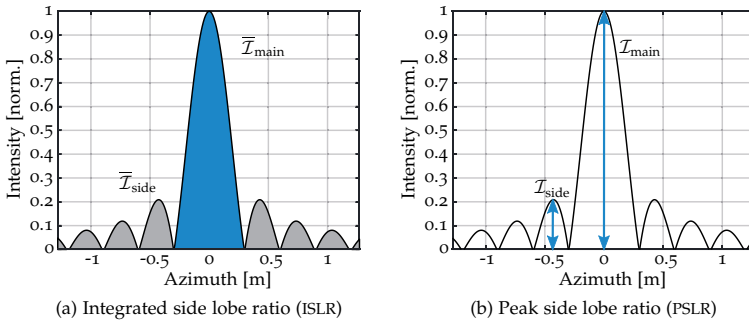


Figure 2.9: The ISLR in (a) includes the main lobe power with the side lobe power. The PSLR in (b) compares the peak value of the main lobe with the side lobe.

Peak Power

The *peak power* value is a good indicator of image focus, because in the case of a smeared image, the intensity of a single scatterer is spread over a few pixels and thus lower than the peak power value of a well focused scatterer. It is defined by

$$\text{PEAK} = \max_{x \in \Omega} \mathcal{I}(x),$$

where the intensity $\mathcal{I}(x)$ is equal to $|\mathcal{R}(x)|^2$ for $x \in \Omega$.

Image Sharpness

The *image sharpness* metric rewards high intensity values similar to the peak power metric. By computing the squared of the pixel intensity and the sum over all pixels, the image sharpness can be computed by

$$S = \sum_{i=1}^{N_{\text{pix}}} |\mathcal{I}(x_i)|^2 = \sum_{i=1}^{N_{\text{pix}}} |\mathcal{R}(x_i)\mathcal{R}^*(x_i)|^2. \quad (2.11)$$

This metric is applied in many sharpness based autofocus techniques like the backprojection autofocus by Ash [Ash12] and the autofocus technique proposed in Chap. 4 of this thesis.

Image Contrast

The *image contrast* is defined by the ration between the standard deviation of the pixel intensities and the mean value. It is calculated by

$$IC = \frac{\sqrt{\frac{1}{N_{\text{pix}}} \sum_{i=1}^{N_{\text{pix}}} (\mathcal{I}(x_i) - \bar{\mathcal{I}})^2}}{\bar{\mathcal{I}}} \quad (2.12)$$

using the mean value of the pixel intensities

$$\bar{\mathcal{I}} = \frac{1}{N_{\text{pix}}} \sum_{i=1}^{N_{\text{pix}}} \mathcal{I}(x_i).$$

A well focused image has a large contrast, which means that the difference between dark and bright pixels is large. This metric is used in maritime autofocus applications [MBH05].

Image Entropy

In information theory, the *entropy* is known as the average amount of information in a message. In the case of uniformly distributed symbols, the entropy is maximal. The entropy is minimal and equal to zero if one symbol has the probability equal to one and all others zero.

This concept is often used as a quality metric in SAR. By minimizing the entropy of a normalized intensity image, less pixels with high intensity as well as simultaneously many pixels with low intensity are rewarded. An image, where all pixels are grey is penalized. To compute the entropy of a SAR image, the intensity has to be normalized firstly to

$$\mathcal{I}^*(x_i) = \frac{\mathcal{I}(x_i)}{\sum_{j=1}^{N_{\text{pix}}} \mathcal{I}(x_j)}$$

for all $i = 1, \dots, N_{\text{pix}}$ pixels. The entropy is then measured by

$$E = - \sum_{i=1}^{N_{\text{pix}}} \mathcal{I}^*(x_i) \ln(\mathcal{I}^*(x_i)).$$

A low entropy indicates a well focused image. The logarithmic term makes an integration of the image entropy metric in an autofocus framework with a closed-form solution difficult.

Maximal Relative Image Error

The *maximal relative image error* is a metric, which compares two SAR images to each other. The quality of a reconstructed image is measured

by comparing it with the reference image. The maximal relative image error is defined by

$$e_{\max} = \frac{\max_{x \in \Omega} (|\mathcal{R}_{\text{ref}}(x) - \mathcal{R}(x)|)}{\max_{x \in \Omega} (|\mathcal{R}_{\text{ref}}(x)|)}. \quad (2.13)$$

This metric is used later to make sure that the fast factorized backprojection algorithm does not cause large image errors related to the reference GBP algorithm.

2.5 BACKPROJECTION AUTOFOCUS

If the true flight path γ is available, the backprojection algorithm reconstructs a perfectly focused SAR image. In practice, only the measured flight path $\hat{\gamma}$ instead of the true flight path γ is known. The flight path is measured by an INS, which integrates the acceleration- and rotation-measurements of an IMU. A typical IMU, which is used for navigation applications, costs more than 100 000 \$ and weighs more than 3 kg [DL13]. Despite its high-quality components, it has usually a time-depending increasing horizontal drift called antenna position error of up to approximately 0.12 mm in 1 s and 0.44 m in 60 s [DL13]. However, this is not precise enough for SAR, since a typical airborne X-band radar system requires antenna position errors of less than 1 cm in 60 s for the reconstruction of a sharp SAR image. The reason is that the antenna position error $\gamma^e = \hat{\gamma} - \gamma$ leads in general to a phase error ϕ^e , which smears the image in the azimuth direction. In addition to the antenna position error, varying atmospheric propagation delays, imperfections of several hardware components and phase noise ψ^e result in radar system timing errors [DL13]. These timing errors can be modeled by independent phase errors. The range-compressed data is phase corrupted, where the phase error ϕ^e consists of a slow varying part, which comes from the antenna position error γ^e and an independent fast varying part ψ^e , which comes from system timing errors. If the slow varying phase errors are approximately less than $\lambda/4$, where λ is the wavelength, the SAR image remains well focused [CGM95]. In practice, the antenna position errors are much greater than $\lambda/4$, which is approximately 75 mm for an X-band radar system. Such an error results in a smeared image.

The task of autofocus techniques is the estimation of the phase error ϕ^e from data in order to correct the resulting smearing in the SAR image automatically. All state-of-the-art autofocus techniques estimate a one-dimensional phase error function $\phi^e : \mathcal{L} \rightarrow \mathbb{R}$ as an approximation of the three-dimensional antenna position error $\gamma^e : \mathcal{L} \rightarrow \mathbb{R}^3$ instead

of estimating the antenna position error itself. The reason is that the estimation of a phase error is sufficient if the antenna position error is not too large and if the reconstructed scene is far away from the radar. Both conditions are typically fulfilled in the case of an airborne far-field SAR scenario using high-end navigation systems.

In the following, we show which conditions have to be fulfilled so that the correction of the phase error ϕ^ϵ instead of the correction of the antenna position error γ^ϵ is sufficient. Let us assume that all errors including the discrete timing phase errors ψ_m^ϵ are available for $m = 1, \dots, M$. Then, a sharp image can theoretically still be reconstructed by

$$\begin{aligned}
 \mathcal{R}(\mathbf{x}_i) &= \sum_{m=1}^M d_m (2/c \cdot \|\gamma_m - \mathbf{x}_i\|_2) \\
 &\quad \cdot \exp(4\pi i f_c/c \cdot \|\gamma_m - \mathbf{x}_i\|_2) \exp(-i\psi_m^\epsilon) \\
 &= \sum_{m=1}^M d_m (2/c \cdot \|\hat{\gamma}_m - \gamma_m^\epsilon - \mathbf{x}_i\|_2) \\
 &\quad \cdot \exp(4\pi i f_c/c \cdot \|\hat{\gamma}_m - \gamma_m^\epsilon - \mathbf{x}_i\|_2) \exp(-i\psi_m^\epsilon) \\
 &= \sum_{m=1}^M d_m (2/c \cdot \|\hat{\gamma}_m - \mathbf{x}_i\|_2 - 2/c \cdot r_m^\epsilon(\mathbf{x}_i)) \\
 &\quad \cdot \exp(4\pi i f_c/c \cdot \|\hat{\gamma}_m - \mathbf{x}_i\|_2) \\
 &\quad \cdot \exp(-4\pi i f_c/c \cdot r_m^\epsilon(\mathbf{x}_i)) \exp(-i\psi_m^\epsilon). \tag{2.14}
 \end{aligned}$$

We define the range error by

$$r_m^\epsilon(\mathbf{x}_i) := \|\hat{\gamma}_m - \mathbf{x}_i\|_2 - \|\gamma_m - \mathbf{x}_i\|_2,$$

which is the correct one-dimensional representation of the three-dimensional antenna position error γ_m^ϵ , since the range error $r_m^\epsilon(\mathbf{x}_i) \in \mathbb{R}$ depends for all $m = 1, \dots, M$ on \mathbf{x}_i , see Fig. 2.10.

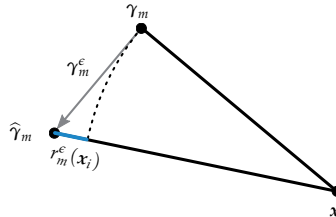


Figure 2.10: Visualization of range error $r_m^\epsilon(\mathbf{x}_i)$, where γ_m is the true aperture position, $\hat{\gamma}_m$ the measured aperture position and \mathbf{x}_i the pixel position.

Moreover, all state-of-the-art autofocus techniques use the following assumptions in order to simplify Eq. (2.14). At first, they assume that the range errors $r_m^\epsilon(x_i)$ have to be less than approximately one-half of the range-resolution δ_r for all $m = 1, \dots, M$ and for all $i = 1, \dots, N_{\text{pix}}$. This allows the simplification

$$d_m(2/c \cdot \|\hat{\gamma}_m - x_i\|_2 - 2/c \cdot r_m^\epsilon(x_i)) = d_m(2/c \cdot \|\hat{\gamma}_m - x_i\|_2)$$

for all $m = 1, \dots, M$ and for all $i = 1, \dots, N_{\text{pix}}$. This first assumption is true if and only if the measured flight path $\hat{\gamma}$ is measured with high precision using a high-quality INS, such that $\hat{\gamma}$ is a good estimate of the true flight path γ .

A second assumption, which all state-of-the-art autofocus algorithms make, is that the range errors $r_m^\epsilon(x_i)$ do not depend on the pixel location x_i . This allows the simplification

$$r_m^\epsilon(x_i) = r_m^\epsilon$$

for all $m = 1, \dots, M$ and all $i = 1, \dots, N_{\text{pix}}$. Hence, for one arbitrary but fixed m , the range errors are equal for all pixels in the image. This assumption is true in most far-field scenarios with an illuminated area of a few kilometers away from the radar sensor. Both assumptions simplify Eq. (2.14) to

$$\begin{aligned} \mathcal{R}(x_i) &= \sum_{m=1}^M \underbrace{d_m(2/c \cdot \|\hat{\gamma}_m - x_i\|_2) \exp(4\pi i f_c/c \cdot \|\hat{\gamma}_m - x_i\|_2)}_{=: \hat{b}_m(x_i)} \\ &\quad \cdot \exp(-4\pi i f_c/c \cdot r_m^\epsilon) \exp(-i\psi_m^\epsilon) \\ &= \sum_{m=1}^M \hat{b}_m(x_i) \exp(-i\phi_m^\epsilon) \end{aligned} \quad (2.15)$$

with the phase term

$$\phi_m^\epsilon = \frac{4\pi f_c}{c} \cdot r_m^\epsilon + \psi_m^\epsilon.$$

Now, only M phase errors ϕ_m^ϵ instead of $M \cdot N_{\text{pix}}$ range errors $r_m^\epsilon(x_i)$ as well as M timing phase errors ψ_m^ϵ have to be estimated in order to correct the smeared SAR image. Moreover, Eq. (2.15) clarifies that in the case of inaccurately measured antenna positions, the original backprojected data $b_m(x_i)$ becomes phase corrupted $\hat{b}_m(x_i) = b_m(x_i) \exp(i\phi_m^\epsilon)$ for $m = 1, \dots, M$ and $i = 1, \dots, N_{\text{pix}}$. To correct this disturbing phases the following autofocus problem has to be solved:

Estimate the corrupt phase ϕ_m^ϵ for all $m = 1, \dots, M$ and use it to generate a focused SAR image

$$\mathcal{R}(x_i, \phi^\epsilon) = \sum_{m=1}^M \hat{b}_m(x_i) \exp(-i\phi_m^\epsilon). \quad (2.16)$$

The exponential term $\exp(-i\phi_m^\epsilon)$ in Eq. (2.16) is called phase correction and $\phi^\epsilon = (\phi_1^\epsilon, \dots, \phi_M^\epsilon)^\top$ is called the stacked phase error vector. The main question is how to estimate the phases ϕ_m^ϵ for all $m = 1, \dots, M$. All state-of-the-art autofocus techniques have a different approach.

Backprojection Autofocus by Ash

One of the most common time-domain autofocus techniques is the backprojection autofocus by Ash [Ash12]. He estimates one phase error $\phi_m^\epsilon \in (-\pi, \pi]$ per pulse by maximizing image sharpness. In particular, his autofocus algorithm [Ash12] uses a coordinate descent framework to estimate all phase errors ϕ_m^ϵ for $m = 1, \dots, M$ separately. During a single turn, one ϕ_m^ϵ is optimized, while the others stay fixed. This procedure can be done a few times to compensate dependencies between the phase errors. In each turn, considering an arbitrary m , the algorithm solves the non-linear least squares problem

$$\hat{\phi}_m^\epsilon = \arg \max_{\phi_m^\epsilon \in (-\pi, \pi]} S(\phi_m^\epsilon), \quad (2.17)$$

where $S : (-\pi, \pi] \rightarrow \mathbb{R}_+$ is the simple but effective *image sharpness* cost function

$$S(\phi_m^\epsilon) = \sum_{i=1}^{N_{\text{pix}}} |\mathcal{R}(x_i, \phi_m^\epsilon) \mathcal{R}^*(x_i, \phi_m^\epsilon)|^2, \quad (2.18)$$

equivalent to the image sharpness function in Eq. (2.11) in Sec. 2.4. This metric works well in autofocus frameworks on a variety of scene types [FM03]. Ash [Ash12] showed that the image sharpness metric in Eq. (2.18) is equivalent to the formulation

$$S(\phi_m^\epsilon) = ||\mathbf{a}_m \cos(\phi_m^\epsilon) + \mathbf{b}_m \sin(\phi_m^\epsilon) + \mathbf{v}_m||^2 \quad (2.19)$$

for $\phi_m^e \in (-\pi, \pi]$, $\mathbf{a}_m = (a_m^{(1)}, \dots, a_m^{(N_{\text{pix}})})^T$, $\mathbf{b}_m = (b_m^{(1)}, \dots, b_m^{(N_{\text{pix}})})^T$ and $\mathbf{v}_m = (v_m^{(1)}, \dots, v_m^{(N_{\text{pix}})})^T$ using the real-valued parameters

$$\begin{aligned} a_m^{(i)} &= 2 \operatorname{Re}(\mathcal{R}_m^C(\mathbf{x}_i) \mathcal{R}_m^*(\mathbf{x}_i)), \\ b_m^{(i)} &= -2 \operatorname{Im}(\mathcal{R}_m^C(\mathbf{x}_i) \mathcal{R}_m^*(\mathbf{x}_i)), \\ v_m^{(i)} &= |\mathcal{R}_m^C(\mathbf{x}_i)|^2 + |\mathcal{R}_m(\mathbf{x}_i)|^2 \end{aligned} \quad (2.20)$$

for $i = 1, \dots, N_{\text{pix}}$, where $\operatorname{Re}(\cdot)$ gets the real value and $\operatorname{Im}(\cdot)$ gets the imaginary component. The image \mathcal{R}_m^C is defined by the phase corrected reflectivity image without the backprojected reflectivity from pulse m , compare Eq. (2.16). The term \mathcal{R}_m represents the backprojected reflectivity only from pulse m without any phase corrections. Details and the proof of the equivalence of Eq. (2.18) and Eq. (2.19) can be found in the appendix A or in the work done by Ash [Ash12]. The non-linear Eq. (2.17) can be solved by many different, mostly iterative algorithms. However, Ash [Ash12] was able to solve Eq. (2.17) in closed-form, which improves the precision of the phase error estimation and the computational costs.

After the phase error $\hat{\phi}_m^e$ has been estimated for a specific m , the reflectivity image can be updated by Eq. (2.16) and m can be incremented. In general, the flow of the algorithm is as follows: sequentially, a back-projected range profile is subtracted from the smeared reconstructed SAR image. Afterwards, the autofocus estimates the phase error and corrects the considered range profile. This phase corrected range profile is again backprojected and added back to the SAR image. Then, the $(m + 1)$ th pulse is considered. This autofocus is widely used for backprojection and yields good results, if the antenna position error is less than one-half of the range-resolution of the SAR system. The effect of the backprojection autofocus by Ash [Ash12] is visualized in Fig. 2.11. In Sec. 2.6 we demonstrate how this autofocus technique performs on real data. With regard to the autofocus of moving ships, it is not sufficient to estimate one phase correction $\phi_m^e \in (-\pi, \pi]$ per pulse m for the entire image, i.e., for the entire ship, since ships move more than one-half of the range-resolution during the observation time of several seconds and they have rotational motions due to the sea waves. We propose to use location-depending phase corrections for one slow-time sample in Chap. 4.

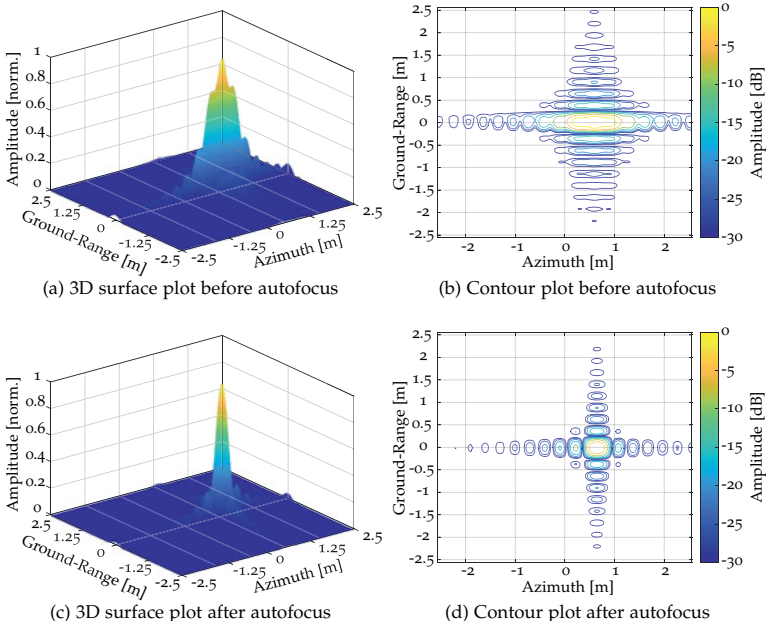


Figure 2.11: Autofocus of a simulated perfect point reflector. In (a) and (b) the point reflector is visualized in a surface plot and a contour plot before the autofocus. The subfigures (c) and (d) show the same point reflector after the autofocus is applied.

2.6 REAL DATA EXAMPLE

In this section, we show a real data example of the GBP algorithm and the backprojection autofocus by Ash [Ash12]. The real data was recorded by the *SmartRadar*¹ (scalable modular aero-space radar technology) [Kir+16] system. It is an airborne X-band system with a chirp bandwidth of 660 MHz and thus a range resolution of $\delta_r = 23$ cm. Some parameters of the data set are listed in Tab. 2.2. The radar sensor was mounted under the wing of a Learjet 35 and it was operating in spotmode.

The data set provides lots of additional information, which is necessary for the reconstruction of a SAR image. For example, the GPS coordinates of the airplane in WGS84 domain as well as the three-dimensional IMU velocities of the sensor are available for each slow-time sample. The

¹ Data was kindly provided by the Hensoldt Sensors GmbH (formerly AIRBUS - Defence and Space)

Table 2.2: Parameters of the real X-band SAR system *SmartRadar* [Kir+16].

Parameter	Value
Carrier Frequency	9.6 GHz
Chirp Bandwidth	660 MHz
Pulse Duration	$15 \mu\text{s}$
Pulse Repetition Frequency	830 Hz
Squint Angle	27.3°
Depression Angle	10.9°
Slant Range	21 200 m
Observation Time	10 s
Platform Velocity	116 m/s
Sampling Frequency	1.2 GHz

flight path in Cartesian x -, y -, z -coordinates is computed by numerically integrating the velocities measured by the IMU sensor. Each component is shown in Fig. 2.12. The SAR geometry is built from GPS data and from the antenna pointing coordinate on the ground, both transferred from WGS84 to Cartesian coordinates.

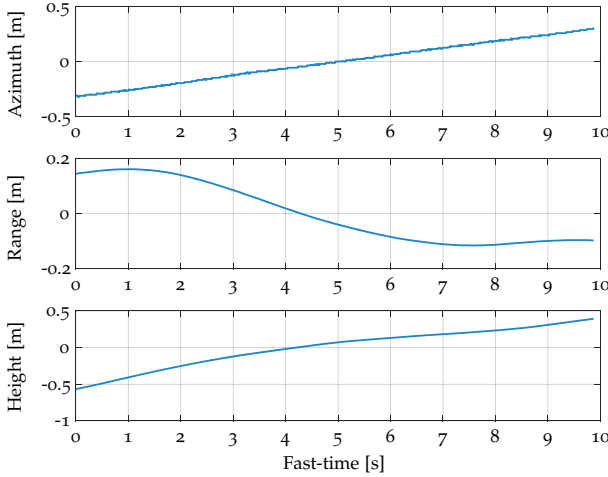


Figure 2.12: Deviations of the measured flight path to the nominal straight line in three dimensions.

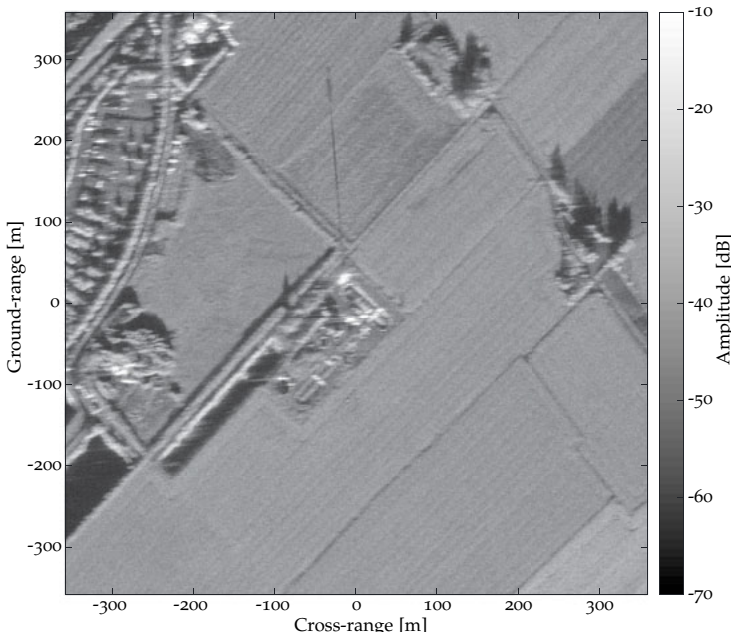


Figure 2.13: Amplitude SAR image reconstructed from real data [Kir+16]. The GBP image reconstruction algorithm without an autofocus leads to a smeared image.

In the preprocessing of the GBP algorithm, we initialized the image grid on the ground. We choose 8192×8192 regular pixels with a pixel spacing of 8.75 cm in each dimension. The pixel size is related to the radar system resolution and should be approximately between 1/3 and 1/2 of the range resolution. The spot center is located in the origin of the image coordinate system. We use 8192 range profiles, which corresponds approximately to the observation time of 10 s. The SAR image in Fig. 2.13 is reconstructed by the GBP algorithm as explained above using Eq. (2.10). A sewage treatment plant, some fields, a few houses and some parking cars can be seen in the focused image. However, since the true flight path is not perfectly measured by the INS, this image is smeared.

Using the Ash autofocus technique [Ash12] described in Sec. 2.5 results in the SAR image visible in Fig. 2.14 and improves the image quality immensely. This is proven by the peak power value, the image contrast

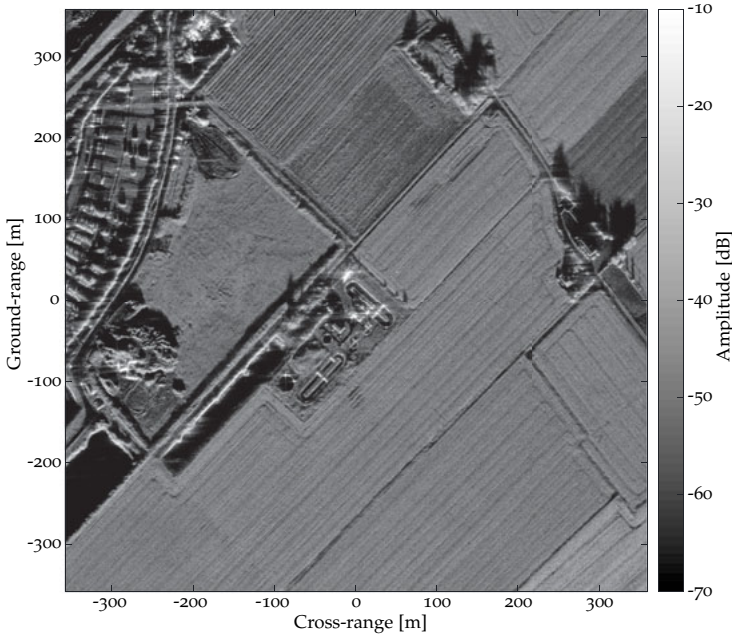


Figure 2.14: Amplitude SAR image reconstructed from real data [Kir+16]. The backprojection autofocus method by Ash [Ash12] improves image quality in comparison to Fig. 2.13.

and the image entropy listed in Tab. 2.3. The Matlab reconstruction of the full image took 11 h and 20 min on a work station with a 3.6 GHz 8-Core processor and 64 GB RAM in single-thread mode. The Ash autofocus additionally needs 25 h and 55 min for the reconstruction of a focused image resulting in 37 h and 15 min.

Table 2.3: Numerical results of GBP and Ash autofocus [Ash12].

	GBP	Ash
Peak Power	962	2753
Contrast	1.22	1.35
Entropy	14.82	14.01

3

OPTIMIZATION OF FAST FACTORIZATED BACKPROJECTION

The *global backprojection* (GBP) algorithm [Faw85; And88; GM10] is the most common time-domain SAR image reconstruction algorithm. It has the advantage of providing perfect image quality even for arbitrary flight paths. However, the computational costs of the GBP algorithm are $O(N^3)$, since it projects N measured range profiles back to a predefined $N \times N$ image grid. In comparison, a frequency-domain algorithm like the Omega-K algorithm [CPR91] has only costs of $O(N^2 \log N)$. A GBP reconstruction of a typical 16 k by 16 k image could take hours using a standard workstation. Ulander et al. invented the *fast factorized backprojection* (FBP) algorithm [UHS03] as a generalized framework of several fast backprojection methods [MR96; Nil97; SHH98; Yeg99]. It combines similar range profiles to reduce the number of finally processed range profiles, which reduces the computational costs to $O(N^2 \log N)$. However, combining range profiles causes range errors, which result in a loss of accuracy. The range errors and thus the image accuracy can be controlled by dividing the entire SAR image into subimages and by reconstructing each of them individually. With an increasing number of subimages, the loss of accuracy decreases, but the computational costs increase as well. In order to reduce the run-time significantly and simultaneously preserve image accuracy, the following factorization parameters of the FBP algorithm have to be chosen in a clever way: the aperture factorization, the image factorization and the number of stages. The aperture factorization describes how many apertures are combined to a new subaperture in each stage. The image factorization in range and in azimuth defines the number of subimages in each stage. The number of stages specifies how often apertures are combined and how often images are divided. These parameters have a significant impact on the computational costs and on the image quality and have to be adjusted for each SAR image reconstruction individually. Until today, it is not clear how these parameters should be chosen optimally.

As the inventor of the FBP algorithm, Ulander et al. [UHS03] provide a conservative estimate of the range errors and thus of the image quality taking the subaperture size and the subimage width into account. They

additionally recommend using many subimages in the first stage to minimize the loss of image quality. Moreover, Ribalta [Rib12] came to the conclusion that near-optimal computational costs can be achieved if an aperture factorization as well as an image factorization of three is used in all stages. Only the number of stages remains adjustable in his rule. We discuss in this chapter both rules, which still do not find the optimum. Additionally, both rules do only make statements about the image factorization in range.

The objective of this chapter is to analyze the factorization parameters of the FBP algorithm in detail in order to propose an optimized parameter choice rule. For this purpose, we propose a way to compute the range errors exactly. By considering the exact range errors instead of estimates of them, we are able to predict the image quality more precisely than state-of-the-art rules [UHS03; Rib12]. In contrast to state-of-the-art rules, we allow a variable aperture factorization, which brings us closer to the optimum. Our parameter choice rule leads to near-optimal factorization parameters and thus to minimal costs for a given image quality, which is often predefined by the application or by the human operator.

This chapter is organized as follows: we explain every step of the FBP algorithm in Sec. 3.1. Afterwards, a detailed analysis of its computational costs is given in Sec. 3.2. The concept of the range error, which is the main reason for the image quality degradation, is introduced in Sec. 3.3. We show in the same section how the range errors can be calculated exactly. Sec. 3.4 describes how the maximal relative image error as an indication of image quality can be estimated from the previously computed exact range errors. In Sec. 3.5, we compare and analyze feasible factorization parameter sets and derive a parameter choice rule in Sec. 3.6. Experimental results of two real data scenarios in Sec. 3.7 show that our proposed factorization parameters lead to a faster computation in comparison with state-of-the-art rules. Furthermore, we estimate the quality more precisely.

3.1 FAST FACTORIZED BACKPROJECTION

The main idea of the *fast factorized backprojection* (FBP) algorithm invented by Ulander et al. [UHS03] is the combination of similar range profiles, which reduces the number of finally processed aperture positions and thus the computational costs. The original aperture positions are denoted by $\gamma_m^{(0)} := \gamma_m$ and the original range-compressed data d is stored in $d^{(0)}$. In every stage $l = 1, \dots, L$, the aperture positions $\gamma_m^{(l-1)}$ for $m = 1, \dots, N_{\text{apt}}^{(l)}$ from the previous stage $(l-1)$ are combined to a

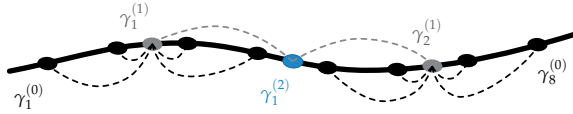


Figure 3.1: Aperture factorization process of a curvy flight path. In the first stage, four aperture positions are combined to a new one. In the second stage, two apertures are merged to one subaperture, described in total by $F_{\text{apt}} = (4, 2)$.

new subaperture position $\gamma_n^{(l)}$ as shown in Fig. 3.1. The new subaperture range profiles

$$d_n^{(l)}(t) \approx \sum_{m=1}^{N_{\text{apt}}^{(l)}} d_m^{(l-1)}(t + \Delta t) \cdot \exp(2\pi i f_c \Delta t) \quad (3.1)$$

are approximated by the sum of $N_{\text{apt}}^{(l)}$ interpolated and phase corrected range profiles $d_m^{(l-1)}$ from the previous stage. This data combination process is the core of the FBP algorithm and can be understood as an approximation of the angular interpolation. In practice, the range profiles $d_m^{(l-1)}$ are discrete and have to be interpolated to get the values $d_m^{(l-1)}(t + \Delta t)$. Often, nearest-neighbor interpolation is used for the interpolation in Eq. (3.1) [UHS03]. However, Frörlind [FU06] found out that cubic interpolation leads to much better image quality. The fast-time correction Δt adjusts the samples of the previous subaperture range profiles, such that they match to the fast-time samples of the new subaperture position. This correction is performed in local polar coordinates as visualized in Fig. 3.2. The fast-time correction Δt is assembled by the law of cosines

$$\Delta t = \sqrt{t^2 + ||\vec{u}_{nm}^{(l)}||_2^2 - 2 t ||\vec{u}_{nm}^{(l)}||_2 \cos \vartheta_{nm}^{(l)} - t}$$

using the angles

$$\cos \vartheta_{nm}^{(l)} = \frac{(\vec{t}_n^{(l)})^T \cdot \vec{u}_{nm}^{(l)}}{||\vec{t}_n^{(l)}||_2 ||\vec{u}_{nm}^{(l)}||_2}$$

and the vectors

$$\begin{aligned} \vec{t}_n^{(l)} &= \vec{x}_{\text{ctr}}^{(l)} - \gamma_n^{(l)}, \\ \vec{u}_{nm}^{(l)} &= \gamma_m^{(l-1)} - \gamma_n^{(l)}. \end{aligned}$$

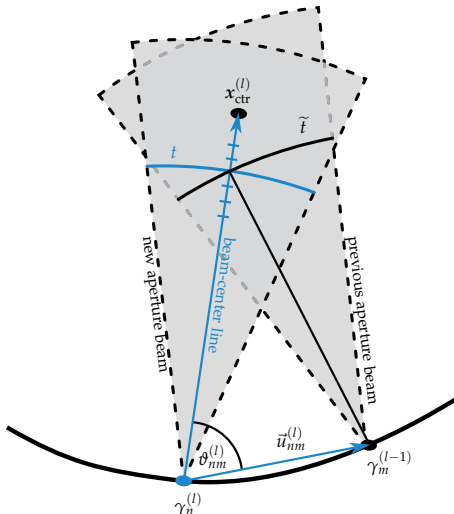


Figure 3.2: Visualization of the angular data approximation process. Here $x_{ctr}^{(l)}$ is the center of the subimage. The new subaperture position is $\gamma_n^{(l)}$. The beam-center line is the blue arrow pointing from $\gamma_n^{(l)}$ to $x_{ctr}^{(l)}$.

The adjusted fast-time vector $(t + \Delta t)$ is used to resample the range profiles from the previous stage $(l - 1)$, see Fig. 3.2. The number of apertures that are combined in each stage is defined by the aperture factorization parameters $F_{apt} = (N_{apt}^{(1)}, \dots, N_{apt}^{(L)})$ with $N_{apt}^{(l)} \in \mathbb{N}$. The number of finally remaining subapertures in the entire flight path, called blocks, is denoted by $N_{blk}^{(L)}$. This data assembling process can be implemented blockwise to save memory. In a far-field scenario, not every fast-time sample has to be corrected individually. Often, one correction Δt is enough for all fast-time samples in a range profile.

After the FBP algorithm has completed the final stage L , the calculated data matrix $d^{(L)}$ is projected column-wise back to each pixel at $x_i \in \Omega$ for $i = 1, \dots, N_{pix}$ by the GBP algorithm. This yields the complex valued reflectivity image

$$\begin{aligned} \mathcal{R}(x_i) = \sum_{m=1}^{N_{blk}^{(L)}} & d_m^{(L)} \left(2/c \cdot \| \gamma_m^{(L)} - x_i \|_2 \right) \\ & \cdot \exp \left(4\pi i f_c / c \cdot \| \gamma_m^{(L)} - x_i \|_2 \right). \end{aligned} \quad (3.2)$$

The angular data interpolation described in Eq. (3.1) yields only $N_{\text{blk}}^{(L)}$ subaperture positions instead of the original M aperture positions with $N_{\text{blk}}^{(L)} \ll M$, which brings the major speed-up of the FBP algorithm. This combination of several range profiles to a new range profile is exact along the beam-center line, which points from the new subaperture position to the center of a new subimage. With an increasing beamwidth, the interpolated range profiles become less accurate compared to the original range profiles. The loss in data accuracy and the accompanying loss in image quality can be described by the range error, which is discussed in Sec. 3.3. This quality loss can be reduced by dividing the image into subimages, such that the beamwidths in each stage are reduced. In every stage $l = 1, \dots, L$, a subimage of the previous stage ($l - 1$) is divided into $N_{\text{az}}^{(l)} \in \mathbb{N}$ subimages in azimuth and in $N_{\text{rg}}^{(l)} \in \mathbb{N}$ subimages in ground-range. Altogether, $N_{\text{img}}^{(l)} = \prod_{i=1}^l N_{\text{rg}}^{(i)} \cdot N_{\text{az}}^{(i)}$ subimages arise per stage and result in the number of subimages $N_{\text{img}} = (N_{\text{img}}^{(1)}, \dots, N_{\text{img}}^{(L)})$, i.e., in the azimuth image factorization $F_{\text{img}}^{\text{az}} = (N_{\text{az}}^{(1)}, \dots, N_{\text{az}}^{(L)})$ and in the ground-range image factorization $F_{\text{img}}^{\text{rg}} = (N_{\text{rg}}^{(1)}, \dots, N_{\text{rg}}^{(L)})$. Each subimage center is denoted by $x_i^{(l)}$ for $i = 1, \dots, N_{\text{img}}^{(l)}$. The more subimages are used, the smaller is the subimage size.

Ulander et al. [UHS03] divide the image into equidistant rectangular subimages, which was introduced as block-FBP in the original paper. In comparison to the polar-FBP algorithm, which divide subaperture beams instead of subimages, the block-FBP is computational more effective. Hence, we consider only the block-FBP algorithm in this thesis. The process of dividing an image into subimages and combining apertures to subapertures is visualized in Fig. 3.3. It can be seen in Fig. 3.3 that the range profiles in the subsequent stage contain less fast-time samples than the range profiles in the previous stage.

3.2 COMPUTATIONAL COSTS

The FBP algorithm reduces the computational costs by combining similar range profiles in each stage. Thus, less aperture positions have to be processed in the final reconstruction of the entire SAR image. The GBP algorithm, which is the reference algorithm, has strictly speaking computational costs of $O(MN_x N_y)$, where M is the number of original aperture positions and $N_x \times N_y$ is the number of pixels in azimuth and in ground-range. Typically, the number of pixels in a SAR image in each dimension coincides with the number of aperture positions, such that

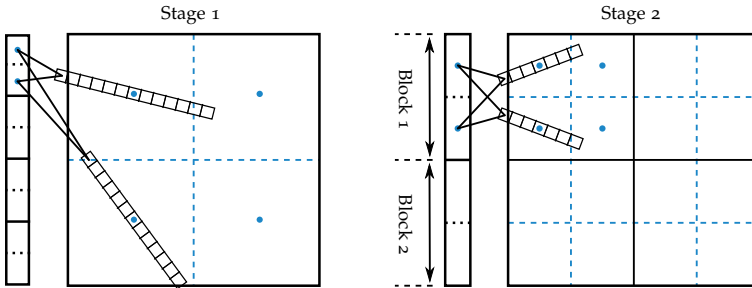


Figure 3.3: Example of image factorization $F_{\text{az}} = (2,2)$ and $F_{\text{rg}} = (2,2)$ resulting in $F_{\text{img}} = (4,4)$ as well as an aperture factorization of $F_{\text{apt}} = (2,2)$. Visualization is based on [UHS03].

$M \approx N_x \approx N_y$ holds. Ulander et al. [UHS03] show that the FBP algorithm has costs of $O(N_x N_y \log M)$, where the number of range profiles reduces from M to $\log M$, while the number of pixels stays the same.

We analyze the computational costs of the FBP algorithm in detail and remind that $N_{\text{blk}}^{(l)}$ describes the resulting number of aperture blocks in stage l , see Fig. 3.3. The number of subimages in ground-range and in azimuth are denoted by $N_{\text{rg}}^{(l)}$ and $N_{\text{az}}^{(l)}$. We define one operation as one interpolation, one phase correction and one summation. Thus, the iterative angular interpolation in Eq. (3.1) has

$$\begin{aligned} \text{OP}^{(l)} &= N_{\text{apt}}^{(l)} N_{\text{blk}}^{(l)} N_{\text{az}}^{(l)} N_{\text{rg}}^{(l)} N_y / N_{\text{rg}}^{(l)} \\ &= N_{\text{apt}}^{(l)} N_{\text{blk}}^{(l)} N_{\text{az}}^{(l)} N_y \end{aligned}$$

operations in each stage l . We assume that the number of range samples in the original range profiles is equal to N_y , which is typical for SAR. Theoretically, the range image division has no influence to the number of operations, since if the image is divided into $N_{\text{rg}}^{(l)}$ range subimages, the number of fast-time samples of a range profile reduces as well by the factor $N_{\text{rg}}^{(l)}$. In practice, this is not always true, since all range profiles usually have a short part, which overlaps as shown in Fig. 3.3. However, this assumption was also made by Ulander et al. [UHS03].

After the L aperture combination stages have been completed, the GBP scheme is used to reconstruct each of the $N_{\text{img}}^{(L)}$ subimages, which

have $N_x^{(L)} \times N_y^{(L)}$ pixels, from the pre-calculated data of the reduced $N_{\text{blk}}^{(L)}$ subaperture positions. Hence, Eq. (3.2) counts

$$\begin{aligned}\text{OP}_{\text{final}} &= N_{\text{blk}}^{(L)} N_{\text{img}}^{(L)} N_x^{(L)} N_y^{(L)} \\ &= N_{\text{blk}}^{(L)} N_x N_y\end{aligned}$$

operations. For large L , the approximation $N_{\text{blk}}^{(L)} \approx \log M$ holds. The summarized number of operations of the FBP algorithm evaluating Eq. (3.1) and (3.2) is

$$\text{OP}_{\text{FBP}} = N_{\text{blk}}^{(L)} N_x N_y + N_y \sum_{l=1}^L N_{\text{apt}}^{(l)} N_{\text{blk}}^{(l)} N_{\text{az}}^{(l)}. \quad (3.3)$$

For a better validation of the FBP speed-up related to the GBP, we define the relative number of operations

$$\text{OP}_{\text{rel}} := \frac{\text{OP}_{\text{FBP}}}{\text{OP}_{\text{GBP}}}, \quad (3.4)$$

where the GBP algorithm has $\text{OP}_{\text{GBP}} = M N_x N_y$ operations. We additionally define the speed-up factor $S := 1/\text{OP}_{\text{rel}}$. Our formulation allows a variable aperture factorization and a variable image factorization in each stage. If only constant aperture factorizations and constant image factorizations are considered, our cost formulation coincides with the formulation of the computational costs by Ulander et al. [UHS03] and Ribalta [Rib12].

3.3 EXACT RANGE ERROR COMPUTATION

Combining several aperture positions to a new subaperture increases the spacing between the new subaperture positions in comparison to the spacing between the original aperture positions, see Fig. 3.1 or Fig. 3.3. This is equivalent to do a subsampling of the data in azimuth, which violates the sampling theorem and the Nyquist criterion [UHS03]. Hence, aliasing occurs in angular dimension, which causes two visual effects. The first one is a loss of peak amplitude and an increase of sidelobe energy. Secondly, multiple ghost targets of each object appear in the scene due to ambiguities. These ghost targets are often visible as widespread noise artifacts in the SAR image. By dividing the image into subimages and by generating range profiles for each subimage individually, the loss of peak amplitude can be reduced and the amplitude of the ghost targets can be suppressed. However, the true reason of both artifacts are

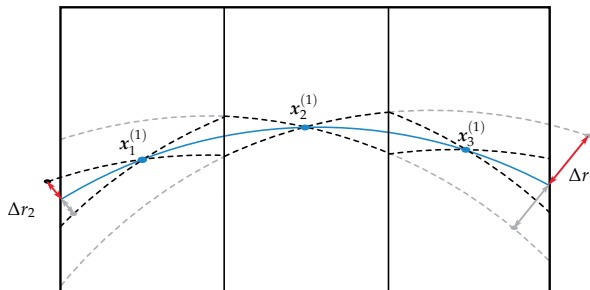


Figure 3.4: Visualization of range errors of an aperture factorization $F_{\text{apt}} = (2)$. The gray circles represent no image factorization resulting in the range error Δr_1 . The much smaller range error Δr_2 comes from $F_{\text{img}}^{\text{az}} = (3)$ and is represented by the black circles evaluated at subimage boundary along line-of-sight.

systematic phase errors, which arise from the data combination process in Eq. (3.1). As mentioned in Sec. 3.1, the interpolated subaperture range profiles are exact only along each beam-center line, which points from the new subaperture position to the considered subimage center, see Fig. 3.2. The larger the angular distances from the pixel of interest to the beam-center lines, the larger are the phase errors. These phase errors can be described by $\exp(4\pi i f_c/c \cdot \Delta r_i)$, where Δr_i denote the corresponding range errors.

We consider the range errors Δr_i as the specific parameters, which connect the image quality with the factorization parameters of the FBP algorithm. To illustrate the concept of the range error, it is visualized in the case of two combined apertures in Fig. 3.4. It can clearly be seen that if the image is divided into three subimages, the range errors reduce immensely from Δr_1 to Δr_2 , which improves image quality. Fig. 3.4 clarifies additionally that the range error can only be maximal at one of the four corners of the entire image. The remaining question is, how many subimages have to be used to keep the image error below a desired level.

Similar to Ulander et al. [UHS03], we measure the image quality by the maximal relative image error

$$e_{\max} = \frac{\max_{x \in \Omega} (|\mathcal{R}_{\text{GBP}}(x) - \mathcal{R}_{\text{FBP}}(x)|)}{\max_{x \in \Omega} (|\mathcal{R}_{\text{GBP}}(x)|)}, \quad (3.5)$$

which was introduced in Eq. (2.13) in Sec. 2.4. Its reference is the image, which is reconstructed by the GBP algorithm. In order to make statements

about the image error before the image is reconstructed, e_{\max} has to be estimated a-priory. Ulander et al. [UHS03] estimate the relative image error using a single point reflector at x_0 and the approximation

$$\frac{|\mathcal{R}_{\text{GBP}}(x_0) - \mathcal{R}_{\text{FBP}}(x_0)|}{|\mathcal{R}_{\text{GBP}}(x_0)|} \approx 4\pi f_c/c \cdot \langle \Delta r(x_0) \rangle, \quad (3.6)$$

where the average of all absolute range errors from all subapertures and all stages at the pixel coordinate x_0 is defined by

$$\langle \Delta r(x_0) \rangle := \frac{1}{N_{\text{apt}}^{(L)}} \sum_{m=1}^{N_{\text{apt}}^{(L)}} |\Delta r_m(x_0)|. \quad (3.7)$$

They give conservative estimates of the range error

$$|\Delta r(x_0)| \leq \begin{cases} \frac{d D}{4 r(x_0)}, & \text{for } d \leq 2 r(x_0), \\ \frac{D}{2}, & \text{for } d > 2 r(x_0), \end{cases} \quad (3.8)$$

where d is the subaperture width, D the subimage width and r the range to the pixel x_0 of interest. Ulander et al. [UHS03] use the Eqs. (3.6) – (3.8) to choose the factorization parameters, which lead to a maximal range error of 0.28 radians in each stage resulting in a maximal relative image error of 1 db. However, their conservative estimation is based on the estimation of the range error in Eq. (3.8).

Ribalta's parameter choice rule [Rib12] recommends to use an aperture factorization of $N_{\text{apt}}^{(l)} = 3$ for all $l = 1, \dots, L$ and an image factorization in azimuth of $N_{\text{az}}^{(l)} = 3$ for all $l = 2, \dots, L$. The image factorization in the first stage can be chosen by the user according to $N_{\text{az}}^{(1)} = 3 N_0$, whereas the factor $N_0 \in \mathbb{R}$ with $N_0 \geq 1$ represents the trade-off between accuracy and efficiency. He also proposed to calculate the number of stages by

$$L_3 = \log_3 \left(\frac{N_{\text{az}} \ln(3)}{3 N_{\text{az}}} \right), \quad (3.9)$$

where $L^* \in \{\lfloor L_3 \rfloor, \lfloor L_3 \rfloor + 1\}$ is an integer next to L_3 . We propose to use the exact range errors instead of coarse estimates from Eq. (3.7) and (3.8) to get a precise prediction of the maximal relative image error in Eq. (3.5). In the following, we present a new method to compute the exact range errors depending on the factorization parameters, the flight path, the depression angle and the image size.

A range error, which is visualized in Fig. 3.4, is basically the distance between two circles, one centered at the original aperture position and one centered at the aperture position of the last stage, evaluated along line-of-sight to the pixel of interest. In order to calculate all exact range errors, the aperture and the image factorization process is used in a reversed way. Thus, we begin with the last stage and move to the first one. In the following, we describe the process of computing the exact range errors. It is also summarized in pseudocode in Tab. 3.1 as well as visualized in Fig. 3.5.

We begin the computation of all exact range errors $\Delta r_m(x_0)$ for $m = 1, \dots, M$ by choosing an arbitrary but fixed x_0 . The range errors are calculated by considering the reference circle segment $C_1^{(L)}$, which goes through x_0 and has its center at the aperture position $\gamma_1^{(L)}$ of the last stage. This circle segment $C_1^{(L)}$ is colored in blue in Fig. 3.5(a) and represents one data sample of a subaperture range profile of the last stage. In the next step, we define the reference point $x_{\text{ref},1}^{(L)}$, which is the intersection

Table 3.1: Pseudocode of exact range error calculation per block.

Algorithm in pseudocode

Input: $x_0, \gamma, x_{\text{ctr}}$

Output: $\Delta r(x_0)$

- 01: Set first reference point $x_{\text{ref},0}^{(L)}$ as x_0
- 02: **for** each stage l **do**
- 03: **for** each subaperture m in block **do**
- 04: Get circles $C_m^{(l)}$ centered at $\gamma_m^{(l)}$ through $x_{\text{ref},m}^{(l+1)}$
- 05: Get line from $\gamma_m^{(l)}$ to $x_{\text{ctr}}^{(l)}$
- 06: Get point $x_{\text{ref},m}^{(l)}$
- 07: **endfor**
- 08: **endfor**
- 09: **for** each aperture m in block **do**
- 10: Get circles $C_m^{(0)}$ centered at $\gamma_m^{(0)}$ through $x_{\text{ref},m}^{(1)}$
- 11: Get line from $\gamma_m^{(0)}$ to x_0
- 12: Get point $x_{\text{ref},m}^{(0)}$
- 13: Get distance Δr_m from x_0 to $x_{\text{ref},m}^{(0)}$
- 14: **endfor**
- 15: **return** range errors $\Delta r(x_0) = (\Delta r_1(x_0), \dots, \Delta r_M(x_0))$

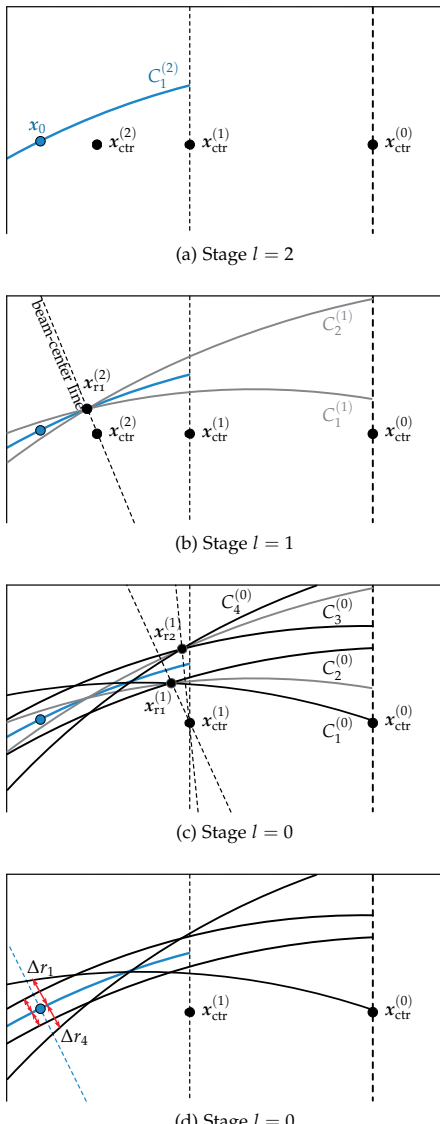


Figure 3.5: Calculation of range errors for the aperture factorization of $F_{\text{apt}} = (2, 2)$ and the image factorization of $F_{\text{img}}^{\text{az}} = (2, 2)$.

of the line from $\gamma_1^{(L)}$ to the subimage center $x_{\text{ctr}}^{(L)}$ and the circle $C_1^{(L)}$, see Fig. 3.5(b).

This data sample was created by combining two samples from the subaperture range profile from the previous stage, see Eq. (3.1), which are represented by the circle segments $C_1^{(L-1)}$ and $C_2^{(L-1)}$. This procedure can be repeated for each stage by calculating the reference points $x_{\text{ref},1}^{(L-1)}$ and $x_{\text{ref},2}^{(L-1)}$ and the new circle segments $C_1^{(L-2)}, \dots, C_4^{(L-2)}$, see Fig. 3.5(c). After stage one is finished, the range errors can be calculated by computing the distances between each circle segment $C_1^{(L-2)}, \dots, C_4^{(L-2)}$ to the considered pixel x_0 along line-of-sight. In summary, the blue circle segment in Fig. 3.5(c), which represents the subaperture range profile from the last stage, was found by combining the aperture range profiles represented by the four black circle segments. A more generalized program flow of the range error calculation of $\Delta r(x_0) = (\Delta r_1(x_0), \dots, \Delta r_M(x_0))$ is given in Tab. 3.1. Since the maximal range errors occur at the corners of the entire image, it is sufficient to compute the range errors only for these four pixels. In the following, we illustrate the relation between the range errors and the image quality.

3.4 IMAGE ERROR ESTIMATION

Aliasing occurs in angular dimension due to the data approximation process in Eq. (3.1) such that the peak amplitude of an object decreases and ghosts targets appear in the final FBP image. We use simulated data from a point scatterer to estimate the peak amplitude loss and the arising amplitude of appearing ghosts in order to measure the resulting maximal relative image error. The number of ghost targets of the point scatterer is

$$N_{\text{gho}} = \prod_{l=1}^L N_{\text{apt}}^{(l)}$$

The location of each ghost target can be calculated preliminary to estimate their amplitude effectively. We assume that the point scatterer is located in the spot center $x_{\text{pt}} = (0, 0, 0)^T$. We use the sampling theorem as well as the mean distance d_{apt} between two original aperture posi-

tions to compute the location of each ghost for the given geometry. The $k = 1, \dots, N_{\text{gho}}$ ghosts are located at $\mathbf{x}_{\text{gho}}^{(k)} = (x_{\text{gho}}^{(k)}, y_{\text{gho}}^{(k)}, 0)^T$ with

$$\begin{aligned} x_{\text{gho}}^{(k)} &= \frac{k\lambda r_0}{2d_{\text{apt}} N_{\text{gho}}}, \\ y_{\text{gho}}^{(k)} &= r_0 - \sqrt{r_0^2 - (x_0^{(k)})^2}. \end{aligned} \quad (3.10)$$

If the squint angle is non-zero, Eq. (3.10) has to be adopted. In order to compute the amplitude of the ghosts effectively, we simplify the GBP algorithm for the case of a single simulated point scatterer analytically using the approximation of the range-compressed data in Eq. (2.9) in terms of si-functions. Hence, we could provide a fast way to compute the true GBP reflectivity

$$\begin{aligned} \mathcal{R}_{\text{GBP}}(\mathbf{x}) &= \sum_{m=1}^{N_{\text{apt}}} \text{si}(2\pi\kappa T/c \cdot r_m(\mathbf{x})) \\ &\quad \cdot \exp(4\pi i f_c/c \cdot r_m(\mathbf{x})) \end{aligned} \quad (3.11)$$

and the phase corrupted FBP amplitude

$$\begin{aligned} \mathcal{R}_{\text{FBP}}(\mathbf{x}) &= \sum_{m=1}^{N_{\text{apt}}} \text{si}(2\pi\kappa T/c \cdot (r_m(\mathbf{x}) + \Delta r_m(\mathbf{x}))) \\ &\quad \cdot \exp(4\pi i f_c/c \cdot (r_m(\mathbf{x}) + \Delta r_m(\mathbf{x}))), \end{aligned} \quad (3.12)$$

where the distance is

$$r_m(\mathbf{x}) = \|\gamma_m - \mathbf{x}\|_2 - \|\gamma_m - \mathbf{x}_{\text{pt}}\|_2.$$

Both reflectivity values computed by Eq. (3.11) and (3.12) are used to estimate the maximal relative image error by Eq. (3.5). This maximal image error has only to be evaluated at the point \mathbf{x}_{pt} to compute the loss of peak amplitude. It must additionally be evaluated at the ghost target positions $\mathbf{x}_{\text{gho}}^{(k)}$ for $k = 1, \dots, N_{\text{gho}}$ to compute the amplitude of the ghosts. This formulation includes the exact range errors as well as the flight path, the depression angle and the image size. It is a reliable metric for the comparison of the factorization parameter sets.

In general, the amplitude of ghost targets decreases with increasing flight path length, because their amplitude spreads over a few pixels in range due to the observation angle. However, for large observation angles the loss of peak amplitude dominates the image error. In summary, this precise image errors estimation together with the estimate of the

computational costs presented in Sec. 3.2 enable us to compare feasible factorization parameter sets.

3.5 PARAMETER ANALYSIS AND OPTIMIZATION

To derive a parameter choice rule, which leads to near-optimal factorization parameters F_{apt} , $F_{\text{img}}^{\text{az}}$, $F_{\text{img}}^{\text{rg}}$ and to the optimal number of stages L , we compare sensible factorization parameter sets regarding computational costs and image quality. The computational costs are described by the relative number of operations OP_{rel} presented in Eq. (3.4). The image quality is specified as the maximal relative image error e_{max} from Eq. (3.5). Both metrics are related to the GBP algorithm as the reference algorithm. In general, the number of sensible factorization parameter sets is too large to compare all of them in a realistic amount of time. For example, only $L = 5$ stages result in approximately 10^{22} possible parameter sets. Hence, we analyze each factorization parameter individually and reduce the number of sensible parameter sets step-by-step.

For this parameter analysis, we use an X-band spotmode SAR scenario, where the geometry is taken from the public Gotcha data set [MS+09]. This data set is very useful, because its swath width is very small. The narrow swath allows us to consider a constant image factorization $N_{\text{rg}}^{(l)} = 1$ in range in the first stages, which reduces the degrees of freedom and simplifies the analysis of the factorization parameters initially. The data set provides an X-band SAR system with a chirp bandwidth of 640 MHz. More information about the data set can be found in Sec. 3.7.

We begin our analysis with the image factorization $F_{\text{img}}^{\text{az}}$ in azimuth by considering $L = 3$ stages and a fix aperture factorization $F_{\text{apt}} = (4, 4, 4)$ as well as 8192 aperture positions. The image factorization in range is set to $F_{\text{img}}^{\text{rg}} = (1, 1, 1)$ due to the narrow swath. The predefined image grid has 2048×8192 pixels with a spacing of 11×7 cm. We vary only the azimuth image factorization and compare the estimated computational costs and the estimated maximal relative image error on the basis of the previously computed exact range errors.

The results are visualized in a scatter plot in Fig. 3.6. The x -axis represents the maximal relative image error e_{max} from Eq. (3.5) and the y -axis describes the relative number of operations OP_{rel} from Eq. (3.4). Every dot in the scatter plot belongs to one specific factorization. For the sake of clarity, we show only the results of significant factorization parameter sets, which are a subset of all investigated sets. Fig. 3.6 shows that the lower blue boundary, which describes the optimal compromise between image quality and computational costs, are those dots, which belong to

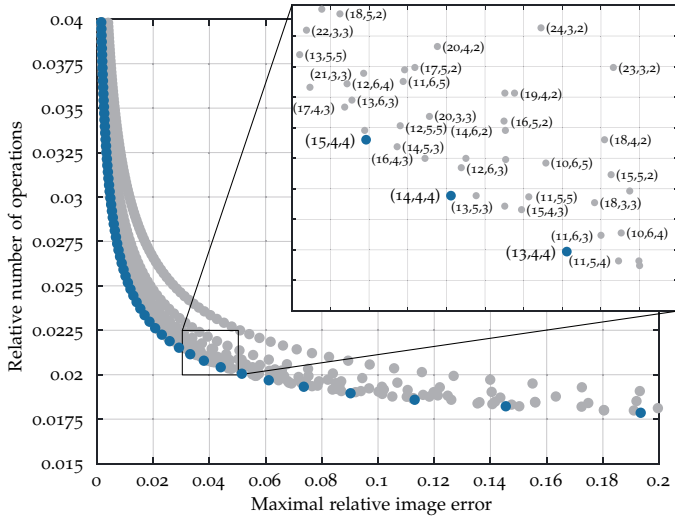


Figure 3.6: Results of factorization parameter sets $F_{\text{apt}} = (4, 4, 4)$, $F_{\text{img}}^{\text{az}} = (\cdot, \cdot, \cdot)$, $F_{\text{img}}^{\text{rg}} = (1, 1, 1)$ and $L = 3$ in the case of 8192 apertures positions for a narrow swath.

the image factorizations of four in the second and in the third stage. The image factorization in azimuth in the first stage determines the maximal relative image error and the computational costs along this lower blue boundary. This result confirms the assumption by Ulander et al. [UHS03] that the image factorization in azimuth is strongly related to the chosen aperture factorization in the same stage. The more subimages are used in the first stage, the lower is the maximal image error and the higher are the computational costs. Our results confirm in addition that the azimuth image factorization in the first stage, i.e., the ratio between the aperture factorization and the azimuth image factorization, has the important task to reduce the range errors and thus to control the image quality. By choosing the image factorization in azimuth equal to the aperture factorization in all stages after the first one, the range errors in all stages are approximately equal. Thus, the best compromise between costs and quality is achieved if and only if the range errors have the same magnitude from stage to stage. These two results of our parameter analysis, which were only possible by considering exact range errors instead of estimates, lead to a better understanding of the factorization parameters

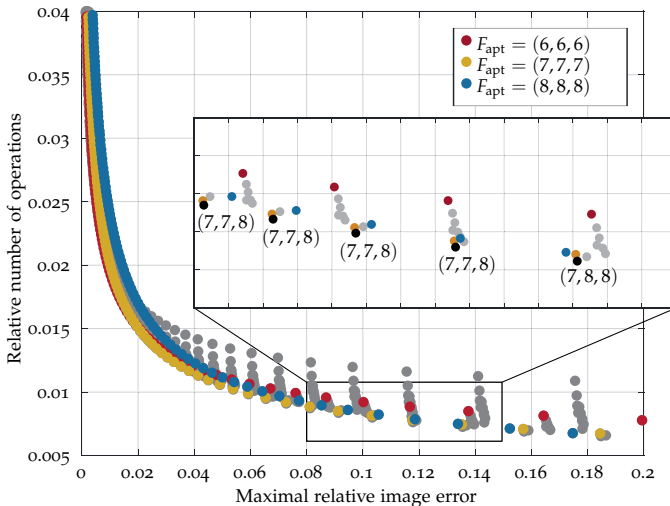


Figure 3.7: Results of factorization parameter sets $F_{\text{apt}} = (\cdot, \cdot, \cdot)$, $F_{\text{img}}^{\text{az}} = (\cdot, N_{\text{apt}}^{(2)}, N_{\text{apt}}^{(3)})$, $F_{\text{img}}^{\text{rg}} = (1, 1, 1)$ and $L = 3$ in the case of 8192 aperture positions.

given in the following: the parameters of the first stage define the image quality and have to be adjusted to the geometry as well as to the image size. The image factorization in azimuth in the subsequent stages should be equal to the aperture factorization and defines in general the speed-up factor.

Next, we analyze different aperture factorizations F_{apt} for $L = 3$ stages again for the narrow swath. We use the interim results from above and consider only sensible factorization parameter sets with variable aperture factorizations $(N_{\text{apt}}^{(1)}, N_{\text{apt}}^{(2)}, N_{\text{apt}}^{(3)})$ as well as a variable image factorization $N_{\text{az}}^{(1)}$ in the first stage. The image factorization in the second and in the third stage are equal to the aperture factorization. We compare these sets regarding the computational costs and the maximal relative image error using the exact range errors as above. The results are visualized in a scatter plot in Fig. 3.7. This figure has to be interpreted the same way Fig. 3.6 was interpreted. It turned out that near-optimal factorization parameters, i.e., the parameter sets, which lie on the lower boundary, are those sets, which are ordered according to an aperture factorization of, for example, $(7,7,7)$, $(7,7,8)$, $(7,8,8)$ and $(8,8,8)$. However, we found out that per-

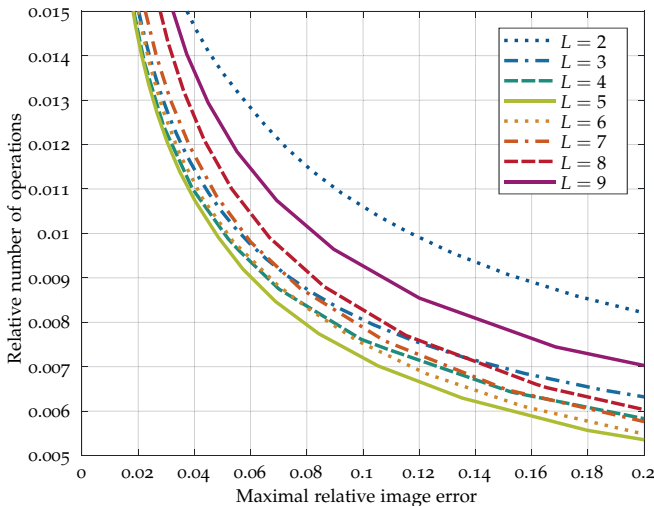


Figure 3.8: Results of different number of stages L .

mutations of an aperture factorization F_{apt} require indeed individually adjusted image factorizations in azimuth, but lead approximately to the same image error and the same costs. The aperture factorization with step-wise increased values leads to marginal better results than other permutations. This result shows that a variable aperture factorization yields better results than a static aperture factorization. In practice, it could make sense to consider only a constant aperture factorization in all stages, since this reduces the degrees of freedom immensely and leads to acceptable results, since the related dots in Fig. 3.7 lie close to the lower boundary line.

In the following, we analyze the effects of different stages L on the computational costs and on the maximal relative image error. For this task, we consider only a few azimuth lines, since the narrow swath needs to be divided into range subimage for stages $L > 3$. For each stage, we compute the costs and the quality of all sensible factorization parameter sets and identify those sets, which describe the lower boundary of all dots. We compare several lower boundaries of sensible stages in Fig. 3.8. It can clearly be seen that the curve, which represents $L = 5$ stages, is the lowest curve and thus represents the optimal factorization parameter sets for this X-band scenario. However, the differences between the optimal

boundary for $L = 5$ and the boundaries for $L = 3, \dots, 8$ are rather small, such that, for example, an aperture factorization of $N_{\text{apt}} = 3$, which mainly describes the line for $L = 5$ and an aperture factorization of $N_{\text{apt}} = 4$, which mainly defines the line for $L = 4$, lead approximately to the same results. This finding is confirmed in Sec. 3.7 by experimental results.

Finally, we analyze the image factorization $F_{\text{img}}^{\text{rg}}$ in ground-range for a narrow swath. The purpose of the range factorization is to ensure that the range errors inside a subimage are similar to each other along line-of-sight. If the image would not be divided in range direction into several subimages, the range errors would be very large at the lower and the upper boundary of the image. In a squinted SAR scenario, this image division is absolutely necessary. Even in the zero-squint case, the image has to be divided into subimages in range. However, using many subimage in range is not advisable. Theoretically, the image factorization in range has no impact on the computational costs, since the range profiles are divided the same way, the image is divided in range. However, many subimages in range let the computational costs increase in practice, since the range profiles have to be longer than the subimage length in range, see Fig. 3.3. In the case of a circular SAR scenario, the image factorization in range should be equal to the image factorization in azimuth. Strictly speaking, the size of the subimages has to be the same in azimuth and in range direction. In the case of a standard side-looking SAR geometry, the image factorization in range may be less than the image factorization in azimuth. Hence, the number of range subimages has to be adapted to the swath-width in the first stage, whereas this number has to be equal to the azimuth image factorization in the subsequent stages.

In summary, our parameter analysis confirms that the factorization parameters in the first stage essentially reduce and control the range errors in all stages and thus specify mainly the image quality [UHS03]. Additionally, the relation between image quality and computational costs is optimal, if each factorization parameter is constant in the subsequent stages $L \geq 2$. This is explained by the fact that the ratio between aperture factorization and image factorization has to be constant, which means the range error in each stage is constant. We summarize the results of our parameter analysis in the following parameter choice rule.

3.6 OPTIMAL PARAMETER CHOICE RULE

This parameter choice rule describes how the factorization parameters, which lead to minimal computational costs for a given upper bound \bar{e}_{max} of the maximal relative image error, can be found. We propose to

estimate the computational costs by the relative number of operations OP_{rel} presented in Eq. (3.4) in Sec. 3.2. The maximal relative image error e_{max} is defined in Eq. (3.5). In order to find the optimal aperture factorization F_{apt} and the optimal image factorization F_{img}^{az} in azimuth as well as the optimal number of stages L , only the first azimuth line of the SAR image grid has to be considered. The image factorization in range can afterwards be determined by considering the entire image grid.

The parameters $N_{apt}^{(1)}, \dots, N_{apt}^{(L)}$, N_{az} , N_{rg} and L are variable and result in the aperture factorization $F_{apt} = (N_{apt}^{(1)}, \dots, N_{apt}^{(L)})$, in the azimuth image factorization $F_{img}^{az} = (N_{az}, N_{apt}^{(2)}, \dots, N_{apt}^{(L)})$ and in the range image factorization $F_{img}^{rg} = (N_{rg}, N_{apt}^{(2)}, \dots, N_{apt}^{(L)})$. Typical values for the variable aperture factorization are $N_{apt}^{(l)} \in \{3, 4\}$ for $l = 1, \dots, L$. However, the variable aperture factorization has to be piecewise constant with one increasing step. The near-optimal factorization parameters can be found by testing feasible parameter sets for one azimuth line. The parameter set, which has minimal computational costs for a given error \bar{e}_{max} , is the optimal one. An initial guess of N_{az} and L can be done using Eqs. (3.6) – (3.8) and Eq. (3.9) by [UHS03; Rib12], respectively. In most cases, $L = 5$ for $N_{apt}^{(l)} = 3$ and $L = 4$ for $N_{apt}^{(l)} = 4$ is a good initialization.

The near-optimal image factorization in range can be determined in the following way: starting with quadratic subimages, the range image factorization has to be reduced step-by-step in the first stage until the image error increases drastically. A drastically increased image error might be reached, if the image error considering the entire grid is approximately 10% larger than the image error in the case of one azimuth line. If the squint angle is large or if the data was received in circular SAR mode, quadratic subimages should be used.

To keep it simple in practice, our parameter choice rule might be simplified in the following way: in order to find an acceptable speed-up factor instead of the optimal one, a constant aperture factorization in all stages might be sufficient. Hence, only the four parameters N_{apt} , N_{az} , N_{rg} and L remain adjustable and result in the aperture factorization $F_{apt} = (N_{apt}, \dots, N_{apt})$ and in the image factorizations $F_{img}^{az} = (N_{az}, N_{apt}, \dots, N_{apt})$ as well as $F_{img}^{rg} = (N_{rg}, N_{apt}, \dots, N_{apt})$. The ratio between N_{apt} and N_{az} in the first stage mainly controls the range errors in all stages and thus the image quality. Both parameters N_{apt} and L mainly determine the speed-up factor of the computational costs in comparison to the GBP algorithm. Again, only $N_{apt} \in \{3, 4\}$ has to be considered. This simplified rule is similar to the state-of-the-art rules [UHS03; Rib12].

3.7 EXPERIMENTAL RESULTS AND EVALUATION

The following two examples demonstrate that our proposed parameter choice rule suggests factorization parameters, which lead to minimized computational costs in terms of the number of operations OP_{rel} for a given upper bound \bar{e}_{max} of the maximal relative image error e_{max} . The first scenario of our numerical evaluation is the spotmode SAR scenario, which was used for the parameter analysis in Sec. 3.5. We use the provided geometry of the public Gotcha X-band data set [MS+09] including its narrow swath. For the numerical evaluation we simulate synthetic data of many perfect point reflectors located equidistantly in the entire scene, since otherwise the results would depend highly on the content of the image and the interpretation of those results would be almost impossible. We compare the aperture factorization F_{apt} , the image factorization F_{img}^{az} in azimuth, the image factorization F_{img}^{rg} in range and the number of stages L from our parameter choice rule with the factorization parameters from Ulander et al. [UHS03] and Ribalta [Rib12]. To be precise, we compare our estimated maximal relative image error \hat{e}_{som} using Eq. (3.5) and the estimated maximal relative image error \hat{e}_{ula} by Ulander et al. with the true maximal relative image error e_{true} . For the comparison of the computational costs we consider the theoretical speed-up factor $\hat{S} = 1/OP_{rel}$ from Eq. (3.4).

After the comparison presented in tabular form, we contrast our estimation errors with Ulander's estimation errors of the maximal relative image errors as well as their variances by considering several FBP reconstructions. These different reconstructions are related to the same simulated data. However, the image grid was shifted a few centimeters in azimuth and in range direction in each FBP reconstruction. This guarantees that the simulated perfect point reflectors do not lie exactly in the center of the subimages, since the error in the middle of a subimage is less than at its boundary. We used 16 different FBP reconstructions for each statistical evaluation. The results are visualized in box plots for each scenario.

In order to show that our method works well with real data, we consider the real data from the public SAR Gotcha X-band data set [MS+09] for a visual comparison of the FBP image with the GBP image. For the FBP reconstruction, we use the factorization parameters suggested by our proposed parameter choice rule. We additionally present two corresponding error images, one in decibel and one in absolute values, which visualize the relative image errors. In these error images, the wide spread noise and the arising ghost targets can clearly be seen.

Table 3.2: Parameters of both airborne X-band SAR systems and scenario.

Parameter	Gotcha [MS+09]	SmartRadar [Kir+16]
Carrier Frequency	9.6 GHz	9.6 GHz
Chirp Bandwidth	640 MHz	660 MHz
Pulse Duration	30 μ s	15 μ s
Sampling Frequency	640 MHz	1.2 GHz
Pulse Repetition Frequency	2.170 Hz	830 Hz
Squint Angle	0.13°	27.18°
Depression Angle	45°	9.6°
Slant Range	10 218 m	22 857 m
Observation Time	4 s	10 s
Mean Altitude	7 251 m	3 872 m
Image Size in Azimuth	901 m	716.80 m
Image Size in Range	143 m	716.80 m

The second example of this numerical evaluation is the real X-band scenario with the *SmartRadar* [Kir+16] data, which was used in Sec. 2.6 and which will be used in Sec. 4.7 for the evaluation of the proposed autofocus technique of large moving ships. We again consider the geometry and the specification of the real X-band radar sensor and simulate synthetic data from many equidistantly located perfect point reflectors in order to avoid the dependencies of the results on the content of the image. We also compare the estimation errors of several FBP reconstructions and present a real data example at the end of this section in order to show that the true image error of a real data example is usually lower than the estimated error. All system parameters of both real X-band systems are listed in Tab. 3.2.

In the following, we discuss the results of each scenario in detail. Keep in mind that the factorization parameters are very scene dependent, such that the recommended factorization parameters differ in each scenario and the results depend strongly on the data.

3.7.1 Narrow Swath SAR using Gotcha data

In this example, we consider the Gotcha data set published by Scarborough et al. [MS+09]. They observed an area of Dayton City in Ohio, USA, with an airborne X-band SAR system in spotmode. Some characteristic parameters of the data set, which provides a narrow swath with 384

azimuth lines, are listed in Tab. 3.2. We use 8192 range profiles from the aperture, where the aperture positions have a spacing of 5.75 cm. The reconstructed image has 8192×2048 pixels, each with a spacing of 11×7 cm. The GBP image of all simulated perfect point reflectors is shown in Fig. 3.10 (a). Its FBP image is presented in Fig. 3.10 (b). The original GBP image using real data is presented in Fig. 3.11 (a). Its reconstruction takes 1 h and 2 min on a work station with a 3.6 GHz 8-Core processor and 64 GB RAM using a multi-thread Matlab implementation.

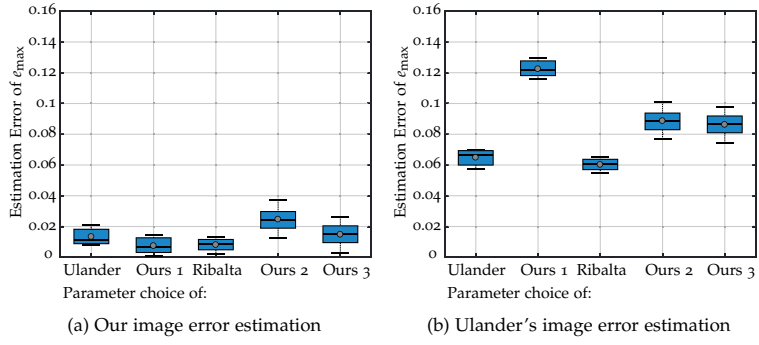
Ulander et al. [UHS03] chose the factorization parameter corresponding to a maximal range error of 0.28 radians in each stage at center frequency. This means that the range errors should be less than 0.7 mm for an X-band system. Such a range error is equivalent to a maximal relative image error of 0.15 computed by Eq. (3.6). This is the given upper bound \bar{e}_{\max} of the relative image error and all FBP reconstruction errors should be less than this upper bound. Thus, we chose those factorization parameters by the rules by Ulander et al., Ribalta and our parameter choice rule, which allow a maximal relative image error of 0.15. Consequently, by using an aperture factorization of $N_{\text{apt}}^{(l)} = 4$ in all $l = 1, \dots, 4$ stages, the azimuth image factorization in the first stage has to be $N_{\text{az}}^{(1)} = 10$ using Ulander's Eqs. (3.6) – (3.8). The remaining factorization parameters are listed in the first column in Tab. 3.3. Ulander et al. [UHS03] estimate for these factorization parameters the maximal relative image error $\hat{e}_{\text{ula}} = 0.1524$, which is approximately $\bar{e}_{\max} = 0.15$. Our estimation \hat{e}_{som} is 0.0739 and thus closer to the real maximal relative image error of $e_{\text{true}} = 0.0872$. These factorization parameters result in a theoretical speed-up factor of $\hat{S} = 113$, see Tab. 3.3.

Ribalta [Rib12] uses an aperture factorization of constantly $N_{\text{apt}}^{(l)} = 3$ in all stages and an image factorization of $N_{\text{az}}^{(l)} = 3$ in all stages except the first one. His rule in Eq. (3.9) yields $L = 5$ as the optimal number of stages. Since he does not propose a rule to determine the image factorization in the first stage, we apply the rule by Ulander et al. [UHS03] for this purpose. Ulander's estimation using Eqs. (3.6) – (3.8) leads to $N_{\text{az}}^{(1)} = 7$ azimuth subimages in the first stage as shown in the third column of Tab. 3.3. Comparing the estimated images error from Ulander with our estimated error shows that our estimation is again much closer to the true value. Tab. 3.3 shows also that Ribalta's factorization parameters lead to a slightly faster computation with $\hat{S} = 118$ in comparison to Ulander's parameters.

For the sake of a better comparison, we apply our parameter choice rule to both cases, where the aperture factorization is constantly four and three. Consequently, we use only an azimuth image factorization

Table 3.3: Results of synthetic scenario [MS+09] with $\bar{e}_{\max} = 0.15$.

	Ulander	Ours 1	Ribalta	Ours 2	Ours 3
F_{apt}	(4, 4, 4, 4)	(4, 4, 4, 4)	(3, 3, 3, 3, 3)	(3, 3, 3, 3, 3)	(3, 3, 3, 4, 4)
$F_{\text{img}}^{\text{az}}$	(10, 4, 4, 4)	(6, 4, 4, 4)	(7, 3, 3, 3, 3)	(5, 3, 3, 3, 3)	(5, 3, 3, 4, 4)
$F_{\text{img}}^{\text{tg}}$	(4, 4, 4, 4)	(1, 4, 4, 4)	(3, 3, 3, 3, 3)	(1, 3, 3, 3, 3)	(1, 3, 3, 4, 4)
\hat{e}_{ula}	0.1524	0.2540	0.1452	0.2032	0.2134
\hat{e}_{som}	0.0739	0.1386	0.0927	0.1388	0.1416
e_{true}	0.0872	0.1312	0.0847	0.1142	0.1269
\hat{S}	113	146	118	138	173

Figure 3.9: Box plots of our estimation errors in (a) and of Ulander's estimation errors in (b). The box plots visualize the mean, the median, the minimum, the maximum and the variance of the estimation errors. Both figures are related to the Tab. 3.3 and to the case $\bar{e}_{\max} = 0.15$.

of $N_{\text{az}}^{(1)} = 6$ instead of $N_{\text{az}}^{(1)} = 10$ in the first stage in comparison to Ulander's recommended factorization parameters as well as $N_{\text{az}}^{(1)} = 5$ instead of $N_{\text{az}}^{(1)} = 7$ in comparison to Ribalta, see column two and four in Tab. 3.3. Additionally, our parameter choice rule reduces the number of subimages in range, which is sensible, since the swath is narrow and both other rules lead to unnecessarily too many subimages in range.

For both factorization parameter sets our estimations of the maximal relative image errors are again more accurate than Ulander's estimations, see Tab. 3.3. The main advantage of our proposed parameter choice rule is the improved speed-up factor of $\hat{S} = 146$ and $\hat{S} = 138$, which is approximately 17–29 % faster than the reconstructions of Ulander

and Ribalta. This is only possible, because we are able to estimate the image error more accurately by taking the exact range errors into account instead of estimating them. Furthermore, the last column in Tab. 3.3 considers a non-constant aperture factorization, which was not discussed by Ulander et al. and Ribalta. Our parameter choice rule recommends to use the optimal $L = 5$ stages, see Fig. 3.8, and an aperture factorization of $F_{\text{apt}} = (3, 3, 3, 4, 4)$ as well as an image factorization in azimuth of $F_{\text{img}}^{\text{az}} = (5, 3, 3, 4, 4)$. Because of the narrow swath, an image factorization in range of $F_{\text{img}}^{\text{rg}} = (1, 3, 3, 4, 4)$ is sufficient. These parameters lead to a slightly faster computation, whereas the image error remains still below the given $\bar{e}_{\text{max}} = 0.15$.

These results are confirmed by the box plots of the estimation error of the maximal relative image errors in Fig. 3.9. In all five cases, the estimation errors of our estimates considering the exact range errors instead of their estimates lead to more precise results. This verifies that our estimation is closer to the true values than the estimation by Ulander et al. [UHS03], even if the image content varies.

Moreover, the results using real data coincide with the results of the numerical evaluation with synthetic data. Fig. 3.11 (b) shows the FBP reconstruction of the real SAR image with our non-constant factorization parameters from the last column in Tab. 3.3. The original GBP image is presented in Fig. 3.11 (a). Both images seem to be equal. However, by looking at the corresponding error images in Fig. 3.12 (a) and Fig. 3.12 (b), some differences can be seen. The first error image is depicted in decibel, where the colormap is equal to the colormap in Fig. 3.11 (a) and Fig. 3.11 (b). This simplifies the comparison between the GBP image, the FBP image and the first error image. The second error image in Fig. 3.12 (b) is visualized without the decibel presentation. Here, the color gray indicates no error and the positive and negative differences to the original GBP image come from a non-coherent error computation in Eq. (3.5). In other words, in Fig. 3.12 (b), only the amplitude of the FBP and the GBP images are compared. Both error images show clearly the peak amplitude loss as well as the arising ghost targets like the white patches on the left hand side of the image, which come from the range profile combination process described in Sec. 3.3. These ghost targets can be reduced by increasing the number of subimages in azimuth. However, the true maximal error of the FBP image using the real data is only 0.0877, whereas our estimation is 0.1416. This indicates that the true error is usually lower than the estimated one.

As mentioned above, the computation of the GBP image needs 1 h and 2 min on our work station. The FBP reconstruction needs only 3 min and 50 s. This is only a speed-up factor of 16, since our non-optimal Matlab implementation uses multiple loops for the reconstruction of all subim-

ages and Matlab is an interpreted language, which has a computational overhead on loops. Additionally, we use overlapping range profiles for each subimage as described in Sec. 3.5. In order to reach real-time capability and to get the theoretical speed-up in practice, specific hardware like a field programmable gate array (FPGA) can be used [Cho+17]. In such a case, the values at unit powers of two are preferred in hardware implementations [Wie19]. Ulander’s parameters can be used, which leads to the image errors shown above.

In summary, this example shows that our parameter choice rule recommends factorization parameters, which lead to a faster computation than state-of-the-art parameter choice rules [UHS03; Rib12] for a given upper bound $\bar{e}_{\max} = 0.15$ of the maximal relative image error.

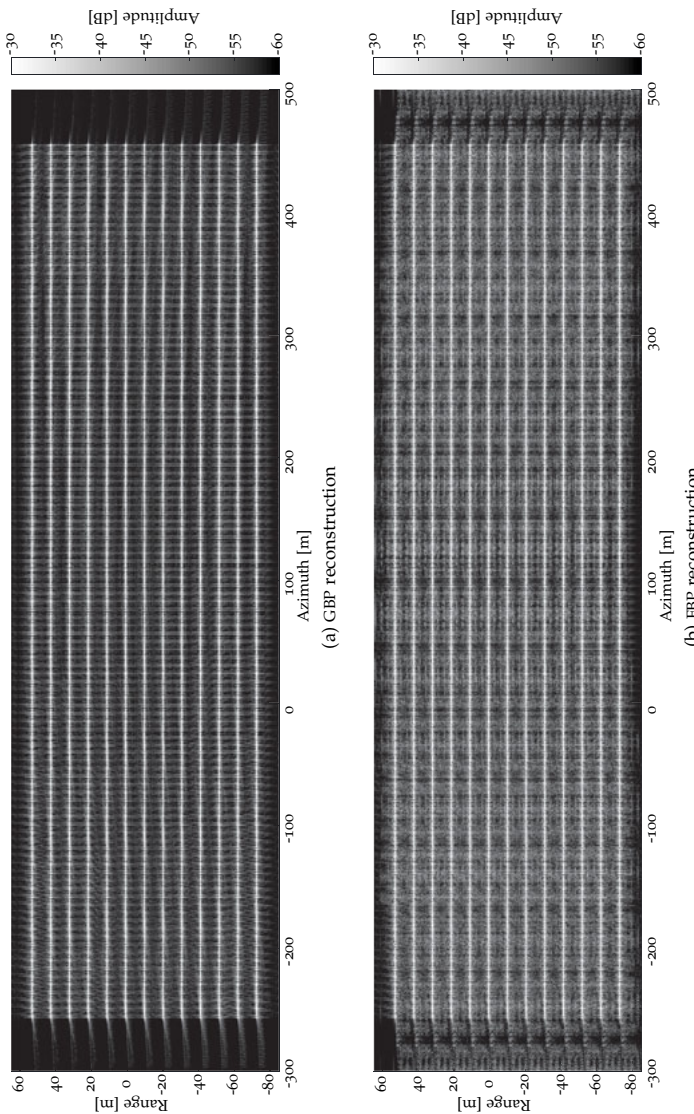


Figure 3.10: Original SAR image reconstructed by the GBP algorithm in (a) and the FBP reconstruction in (b). The scene consists of several equidistant distributed perfect point reflectors.

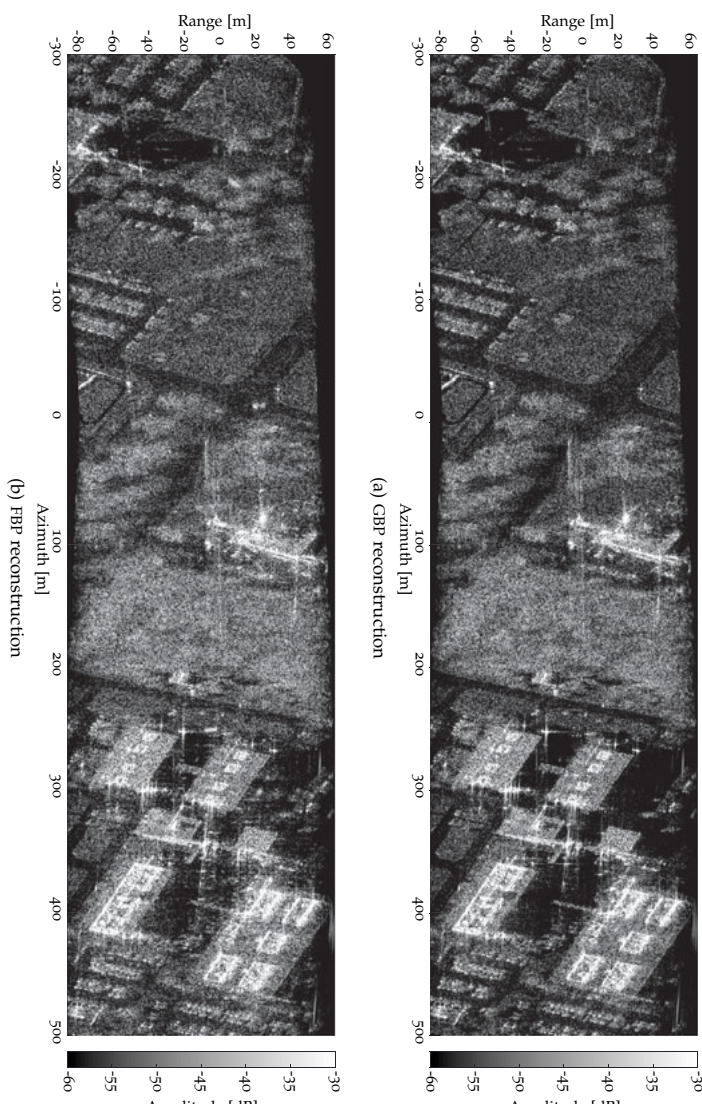


Figure 3.11: Original SAR image reconstructed by the GBP algorithm in (a) and the FBP reconstruction using $F_{\text{opt}} = (3, 3, 3, 4, 4)$, $F_{\text{img}}^{\text{az}} = (5, 3, 3, 4, 4)$ and $F_{\text{img}}^{\text{sg}} = (1, 3, 3, 4, 4)$ in (b). The airborne X-band SAR data is taken from the public Gotcha data set [MS+09].

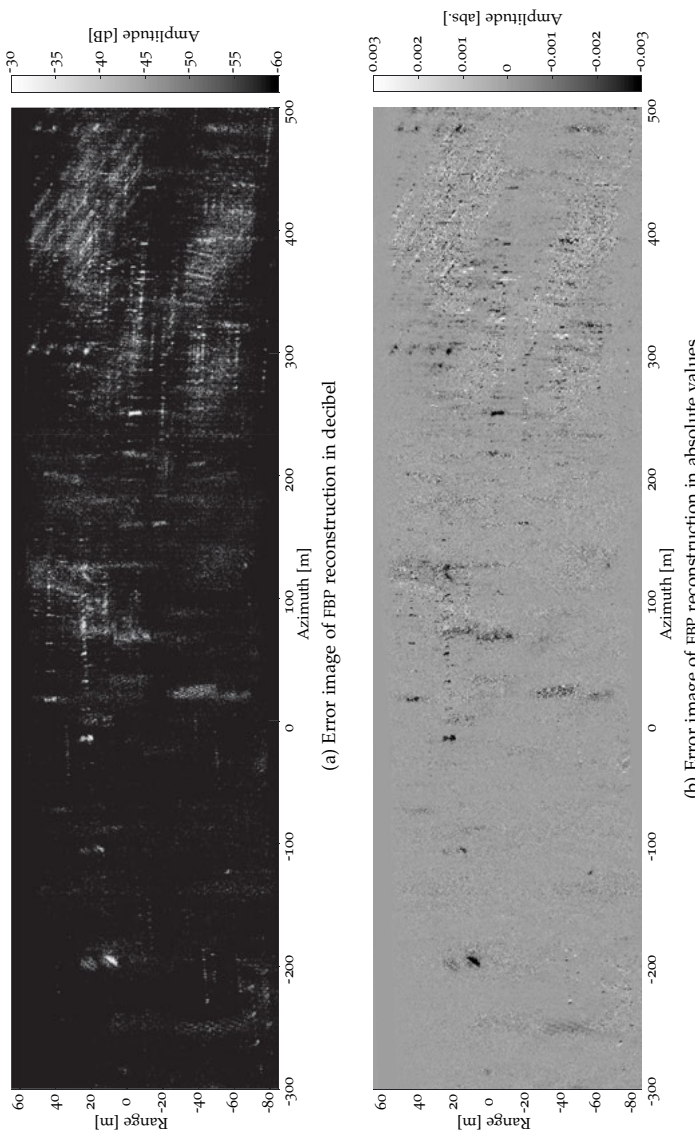
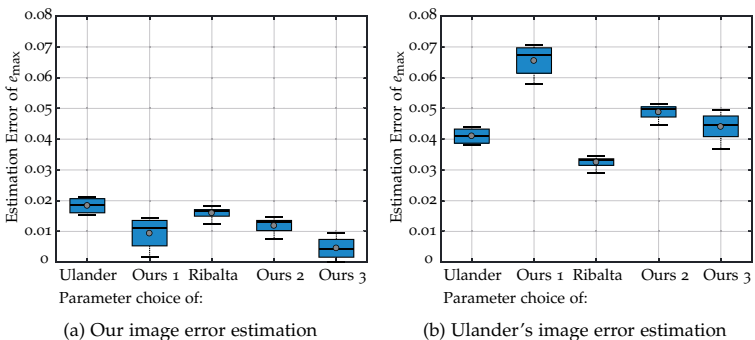


Figure 3.12: Error images of FBP reconstruction in decibel in (a) and in absolute values in (b). In (b) the colormap is cropped in order to visualize the true error more clearly. Our factorization parameters result in a maximal relative image error of 0.087.

Table 3.4: Results of synthetic scenario [MS+09] with $\bar{\epsilon}_{\max} = 0.10$.

	Ulander	Ours 1	Ribalta	Ours 2	Ours 3
F_{apt}	(4, 4, 4, 4)	(4, 4, 4, 4)	(3, 3, 3, 3, 3)	(3, 3, 3, 3, 3)	(3, 3, 3, 4, 4)
$F_{\text{az}}^{\text{img}}$	(16, 4, 4, 4)	(10, 4, 4, 4)	(11, 3, 3, 3, 3)	(8, 3, 3, 3, 3)	(8, 3, 3, 4, 4)
$F_{\text{img}}^{\text{rg}}$	(4, 4, 4, 4)	(1, 4, 4, 4)	(3, 3, 3, 3, 3)	(1, 3, 3, 3, 3)	(1, 3, 3, 4, 4)
$\hat{\epsilon}_{\text{ula}}$	0.0953	0.1524	0.0924	0.1270	0.1334
$\hat{\epsilon}_{\text{som}}$	0.0728	0.0964	0.0760	0.0902	0.0934
ϵ_{true}	0.0598	0.0870	0.0647	0.0783	0.0894
$\hat{\epsilon}$	85	113	91	110	127

Figure 3.13: Box plots of our estimation errors in (a) and of Ulander's estimation errors in (b). The box plots visualize the mean, the median, the minimum, the maximum and the variance of the estimation errors. Both figures are related to the Tab. 3.4 and to the case $\bar{\epsilon}_{\max} = 0.10$.

Ulander et al. [UHS03] assumed in their work that a peak amplitude loss of 1 dB compared to the original GBP reconstruction, which is equivalent to a relative estimation error of 0.10, is a preferable image quality. We do the entire evaluation including the comparison with Ulander's and Ribalta's factorization parameter choice rules for the given maximal relative image error of 0.10. The resulting factorization parameter sets from Ulander et al. [UHS03] and Ribalta [Rib12] as well as ours are listed in Tab. 3.4. Since the image factorization in azimuth in the first stage has the most impact on the image quality, only this parameter changes in comparison the the 0.15 error case. Tab. 3.4 shows that our estimation of the maximal relative image errors are again more accurate than the esti-

mates by Ulander et al. The results are similar to the previous case. Our estimation leads to a lower estimation error and to a similar estimation error variance, see Tab. 3.4 and Fig. 3.13. This second evaluation shows that our estimation is valid for different levels of the relative image error.

3.7.2 Squinted SAR using SmartRadar data

In this example, we evaluate the factorization parameters for the same X-band spotmode scenario as considered in Sec. 2.6. Some parameters of the airborne *SmartRadar* [Kir+16] system and the geometry are listed in Tab. 3.2. The reconstructed SAR image has $8\,192 \times 8\,192$ pixels with a spacing of $8.75\text{ cm} \times 8.75\text{ cm}$. The synthetic aperture consists of 8 192 aperture positions with a spacing of 14 cm. To confirm that our estimated maximal relative image error \hat{e}_{som} is close to the true e_{true} , we simulate in this example again synthetic data from many point scatterers uniformly distributed over the entire image. This guarantees that the results do not depend highly on the image content. Since the maximal relative image error of a real data scenario is much lower than the image error using simulated data, the results of many perfect point reflectors can be interpreted as a kind of worst case scenario. The GBP image of all distributed perfect point reflectors and its FBP image are show in Fig. 3.16(a) and Fig. 3.16(b).

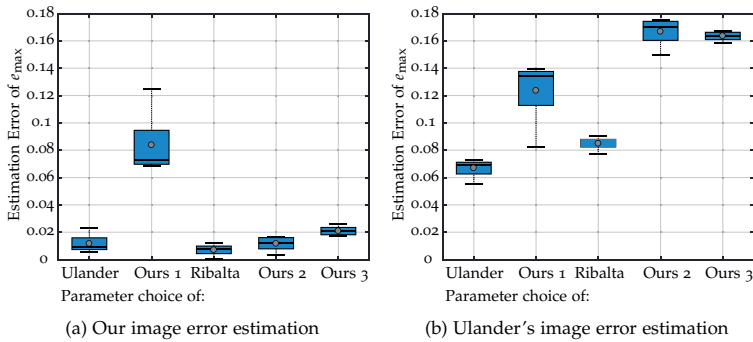
The factorization parameters from Ulander's, Ribalta's and our parameter choice rules as well as their results are listed for $\bar{e}_{\text{max}} = 0.15$ in Tab. 3.5 and for $\bar{e}_{\text{max}} = 0.10$ in Tab. 3.6, respectively. The results are given by the maximal relative image error \hat{e}_{ula} estimated by Ulander and the maximal relative image error \hat{e}_{som} estimated by us as well as the true maximal relative image error e_{true} . The theoretical speed-up factor \hat{S} describes the computational costs with regard to the GBP algorithm. Again each column in Tab. 3.5 and Tab. 3.6 shows the results of a constant aperture factorization of 3 and 4 as well as our non-constant aperture factorization. It can be seen in both tables that in all ten cases our estimation \hat{e}_{som} is closer to the true e_{true} than \hat{e}_{ula} . Furthermore, the estimation errors of the estimated maximal relative image errors as well as their variances presented in Fig. 3.14 and Fig. 3.15 confirm that our estimation errors are lower than the state-of-the-art [UHS03; Rib12] estimation errors.

This second real data scenario shows that our estimation is not only valid for different levels of the relative image error. It is also valid for various scenes including highly squinted scenarios.

In some cases our maximal relative image error estimation \hat{e}_{som} is lower than the true e_{true} . The reason is that the arising ghost targets from different simulated perfect point reflectors might be located at the same

Table 3.5: Results of synthetic scenario [Kir+16] with $\bar{e}_{\max} = 0.15$.

	Ulander	Ours 1	Ribalta	Ours 2	Ours 3
F_{apt}	(4, 4, 4, 4)	(4, 4, 4, 4)	(3, 3, 3, 3, 3)	(3, 3, 3, 3, 3)	(3, 3, 3, 4, 4)
$F_{\text{img}}^{\text{az}}$	(8, 4, 4, 4)	(4, 4, 4, 4)	(6, 3, 3, 3, 3)	(3, 3, 3, 3, 3)	(3, 3, 3, 4, 4)
$F_{\text{img}}^{\text{rg}}$	(4, 4, 4, 4)	(1, 4, 4, 4)	(3, 3, 3, 3, 3)	(1, 3, 3, 3, 3)	(1, 3, 3, 4, 4)
\hat{e}_{ula}	0.1524	0.3106	0.1380	0.2761	0.2899
\hat{e}_{som}	0.0739	0.1033	0.0599	0.1178	0.1204
e_{true}	0.0855	0.1870	0.0522	0.1093	0.1310
\hat{S}	113	170	127	166	227

Figure 3.14: Box plots of our estimation errors in (a) and of Ulander's estimation errors in (b). The box plots visualize the mean, the median, the minimum, the maximum and the variance of the estimation errors. Both figures are related to the Tab. 3.5 and to the case $\bar{e}_{\max} = 0.15$.

location. Hence, their intensity sums up such that the FBP image has a large error in comparison with the GBP image. However, this happens in practice very rarely.

The FBP image in Fig. 3.17(b) and especially the errors images in Fig. 3.18(a) and Fig. 3.18(b) show artifacts due to image errors. The typical ghosts targets and the typical white noise artifacts can clearly be seen in Fig. 3.18 (b). These error stripes verify that the range errors are maximal at the boundary at the subimages and minimal at their centers. Hence, a given maximal relative image error of $\bar{e}_{\max} = 0.05$ might be the better choice if a high-quality SAR image is needed.

Table 3.6: Results of synthetic scenario [Kir+16] with $\bar{e}_{\max} = 0.10$.

	Ulander	Ours 1	Ribalta	Ours 2	Ours 3
F_{apt}	(4, 4, 4, 4)	(4, 4, 4, 4)	(3, 3, 3, 3, 3)	(3, 3, 3, 3, 3)	(3, 3, 3, 4, 4)
$F_{\text{img}}^{\text{az}}$	(12, 4, 4, 4)	(5, 4, 4, 4)	(9, 3, 3, 3, 3)	(4, 3, 3, 3, 3)	(4, 3, 3, 4, 4)
$F_{\text{img}}^{\text{rg}}$	(4, 4, 4, 4)	(1, 4, 4, 4)	(3, 3, 3, 3, 3)	(1, 3, 3, 3, 3)	(1, 3, 3, 4, 4)
\hat{e}_{ula}	0.1035	0.2485	0.0920	0.2071	0.2174
\hat{e}_{som}	0.0359	0.0957	0.0421	0.0935	0.0959
e_{true}	0.0560	0.1476	0.0347	0.0812	0.0968
\hat{S}	102	157	103	151	196

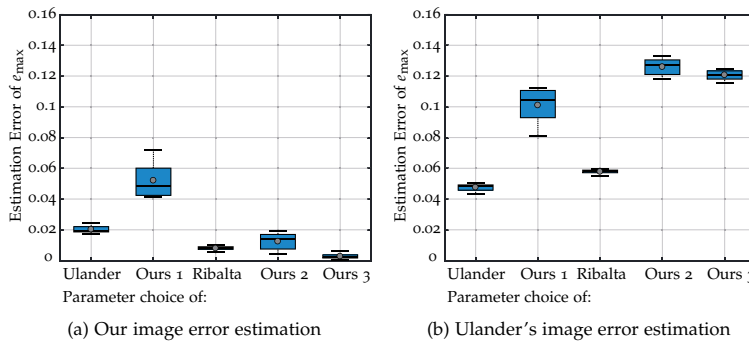


Figure 3.15: Box plots of our estimation errors in (a) and of Ulander’s estimation errors in (b). The box plots visualize the mean, the median, the minimum, the maximum and the variance of the estimation errors. Both figures are related to the Tab. 3.6 and to the case $\bar{e}_{\max} = 0.10$.

In summary, using the exact range errors instead of its estimates leads to a better estimation of the image error. Using a variable aperture factorization makes the computation faster, whereas the image quality stays the same. In practice, considering a constant aperture factorization is sufficient, because it reduces the factorization parameters to N_{apt} , N_{az} , N_{rg} and L with the drawback of a slower computation.

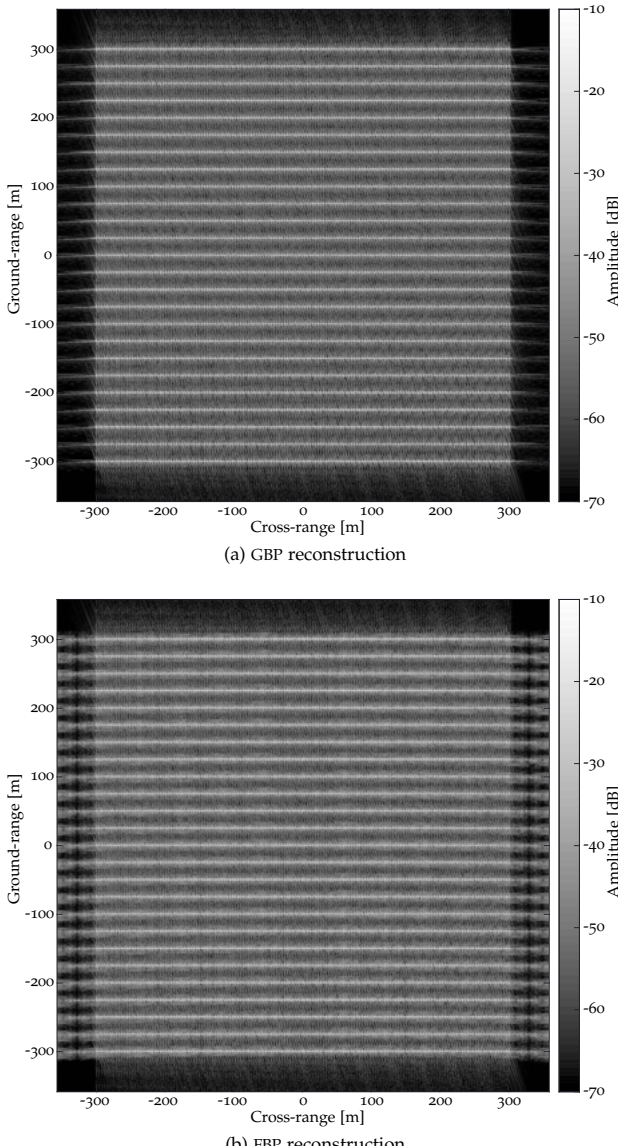


Figure 3.16: Original SAR image reconstructed by the GBP algorithm in (a) and FBP reconstruction in (b). The scene consists of several equidistant distributed perfect point reflectors.

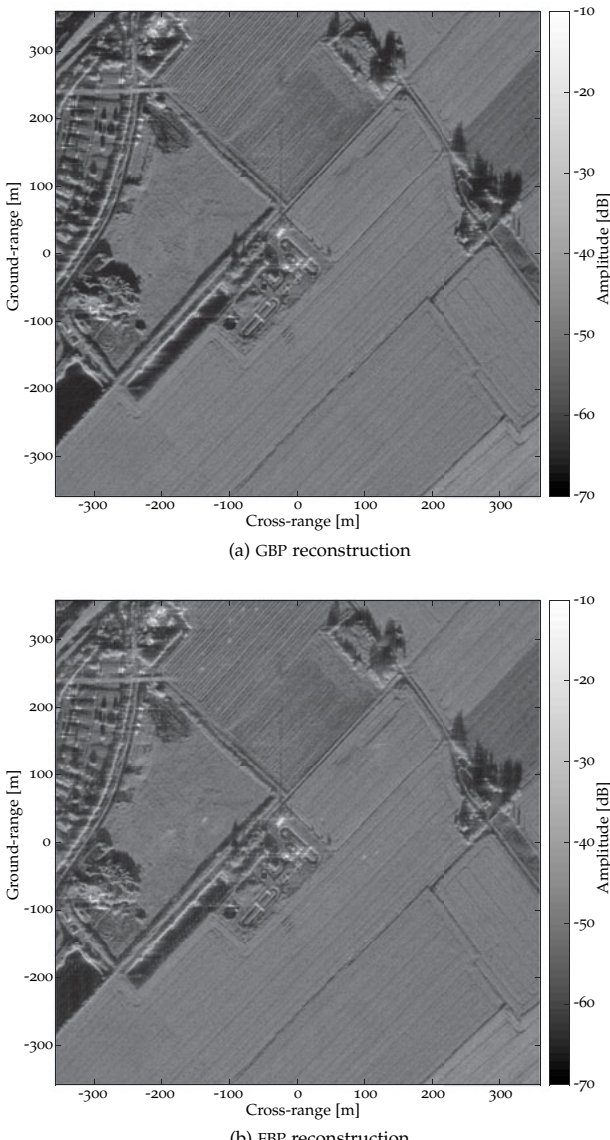
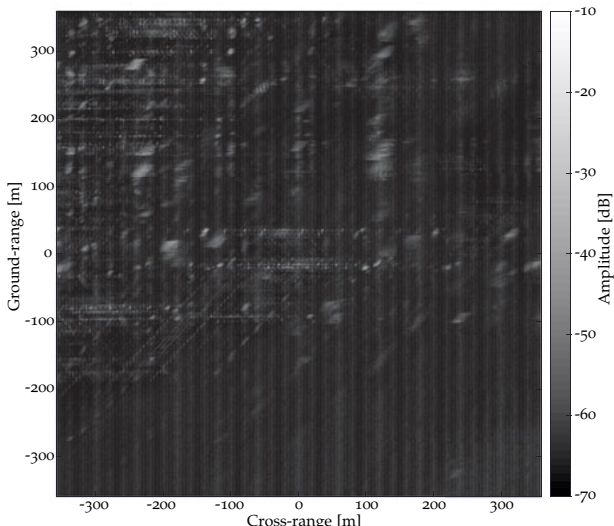
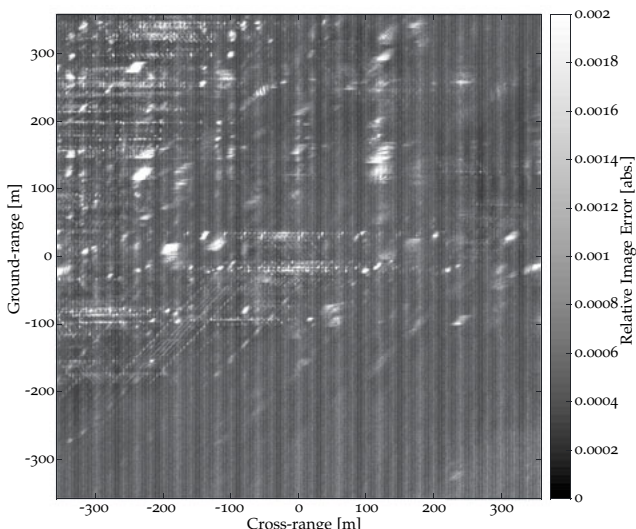


Figure 3.17: Original SAR image reconstructed by the GBP algorithm in (a) and FBP reconstruction using $F_{\text{apt}} = (3, 3, 3, 4, 4)$, $F_{\text{img}}^{\text{az}} = (4, 3, 3, 4, 4)$ and $F_{\text{img}}^{\text{rg}} = (1, 3, 3, 4, 4)$ in (b). The image reconstructed from the airborne X-band data set [Kir+16] shows a landscape. Some artifacts resulting from the FBP reconstruction are visible in (b).



(a) Error image of FBP reconstruction in decibel



(b) Error image of FBP reconstruction in absolute values

Figure 3.18: Error images of FBP reconstruction in (a) in decibel and in (b) in absolute values. In (b), the colormap is cropped in order to visualize the true error more clearly. The factorization parameters $F_{\text{apt}} = (3, 3, 3, 4, 4)$, $F_{\text{img}}^{\text{az}} = (5, 3, 3, 4, 4)$ and $F_{\text{img}}^{\text{rg}} = (1, 3, 3, 4, 4)$ result in a maximal relative image error of 0.0540.

4

AUTOFOCUS OF LARGE SHIPS WITH ARBITRARY MOTION

In the previous chapter, we showed how the *fast factorized backprojection* (FBP) algorithm [UHS03] has to be configured in order to reconstruct a high-quality *synthetic aperture radar* (SAR) image as fast as possible. This is necessary for the context of all real-time maritime surveillance applications. The most interesting application in maritime surveillance is the monitoring of maritime traffic in all-weather conditions. For this application, a large SAR image of the open sea is used for ship detection and classification. However, large ships with arbitrary motions are smeared, shifted and deformed in an airborne SAR image due to their non-linear motions including deformations, rotations and translations. This makes a classification or even an identification only based on SAR images very difficult. Additional, unknown antenna position errors of the *antenna phase center* (APC), which result from a non-perfectly working *inertial navigation system* (INS), lower the image quality further. Using an autofocus algorithm for the entire image would not improve the image quality, because every ship moves differently and thus has to be treated individually. These image quality degradations are caused by the unknown arbitrary motions of ships during the long observation time of several seconds.

All state-of-the-art autofocus techniques like the phase gradient algorithm [HEGJJ89], the mapdrift autofocus [MS81], the backprojection autofocus [Ash12] and the image-contrast-based technique [MBH05] require an almost linear and uniform motion of the ship without rotations. This is only true, either if the observation time is short, which results in a coarse azimuth resolution and low image quality, or if the sea is almost flat, which happens very rarely. Until today, no autofocus technique is able to estimate the non-linear motion of a ship independent of the sea state and for a long observation time to offer the necessary image quality for the classification of maritime objects.

In this chapter¹, we propose an extended autofocus technique, which focuses arbitrarily moving and maneuvering ships with high quality.

¹ This chapter contains text, results and images from publications [SO18; SO19], which have been previously published.

Our technique uses the framework of the *global backprojection* (GBP) algorithm [Faw85; And88; GM10] and the idea of estimating phase errors by maximizing image sharpness similar to Ash [Ash12]. In contrast to Ash, we divide the image into small subimages and estimate pulse-by-pulse the relative distances between the aperture positions and all subimages by maximizing subimage sharpness. This approach enables us to do a range correction for each pixel and for each pulse individually as well as to compensate unknown antenna position errors simultaneously. In contrast to state-of-the-art algorithms, we are able to reconstruct a focused SAR image of a large ship with arbitrary motion including deformations, rotations and translations using data from a long observation time, which improves the image quality immensely such that details on deck of the ship become visible.

This chapter is organized as follows: Sec. 4.1 explains how ships are detected by the constant false alarm rate detector and how their locations are estimated in a SAR image. In Sec. 4.2, we extend the signal model of a static scene given in Sec. 2.2 to the case where only one ship moves arbitrarily including deformations, rotations and translations. Afterwards, we show by synthetic data that arbitrarily moving ships appear smeared, shifted and deformed in radar images and explain the reasons for these effects in Sec. 4.3. All of these effects can be compensated if the motion of the ship is known exactly and if the GBP algorithm uses a moving and deforming grid to include the motion into the image reconstruction algorithm, which is shown in Sec. 4.4. Typically, the motion of a ship is unknown and has to be estimated. How the unknown motion is estimated by the state-of-the-art backprojection autofocus method by Ash [Ash12] and by the state-of-the-art image-contrast-based technique by Martorella et al. [MBH05] is explained in Sec. 4.5. Our proposed autofocus algorithm, which estimates range errors for several subimages by maximizing subimage sharpness, is presented in Sec. 4.6. This chapter ends with the experimental results of real data scenarios in Sec. 4.7. The results of our proposed autofocus algorithm considering three moving ships and one static scene, illuminated by a real airborne single-channel X-band radar system, are compared with the results of the two state-of-the-art techniques by Ash [Ash12] and by Martorella et al. [MBH05].

4.1 SHIP DETECTION AND LOCATION ESTIMATION

Let us assume that a SAR image of the entire scene has been successfully reconstructed for example by the FBP algorithm [UHS03] or by the Omega-K algorithm [CW05]. It can be an image in full resolution or a kind of preview image, which consists only of a few large pixels. Reconstructing the latter saves computational costs. In both cases, we have a two-dimensional amplitude image as input data of the ship detection algorithm.

In general, a detector decides, whether the cell under test belongs to a target or to the background. In detail, it checks if the amplitude of the cell is lower or greater than a simple threshold value. This decision is made for all cells in the image. A cell can be a group of pixels or just a single pixel. In SAR images, the noise and the clutter are not homogeneous for the entire image as shown by a one-dimensional example in Fig. 4.1 (a). Thus a simple threshold detection could fail.

The most common detector in radar literature is the *constant false alarm rate* (CFAR) detector [AR14]. It uses a dynamic threshold to overcome the problem of the non-homogeneous noise always present in SAR images. In contrast to classical detectors, the threshold value of the CFAR detector depends on the noise level of the neighborhood. This noise level is estimated in training cells located around the cell under test. Guard cells between the cell under test and the training cells ensure that if the target is larger than one cell, the threshold is not influenced by the target itself. An adjustable desired false alarm rate probability gives the detector its name.

Three parameters of the CFAR detector have to be defined a-priory: the band size of the guard cells, the band size of the training cells and the false alarm rate probability. The band size of the guard cells and the band size of the training cells are defined according to Fig. 4.1 (b). The false alarm rate probability P_{fa} is typically chosen to be 10^{-3} in radar applications. If N_{cfar} test cells are chosen, the noise power estimate is [AR14]

$$\hat{P}(x_i) = \frac{1}{N_{cfar}} \sum_{j=1}^{N_{cfar}} \mathcal{A}(x_j) \quad (4.1)$$

based on the amplitude \mathcal{A} evaluated at pixels x_j for $j = 1, \dots, N_{cfar}$. The desired false alarm rate P_{fa} defines the threshold factor [AR14]

$$\alpha_{cfar} = N_{cfar} \left(P_{fa}^{-1/N_{cfar}} - 1 \right),$$

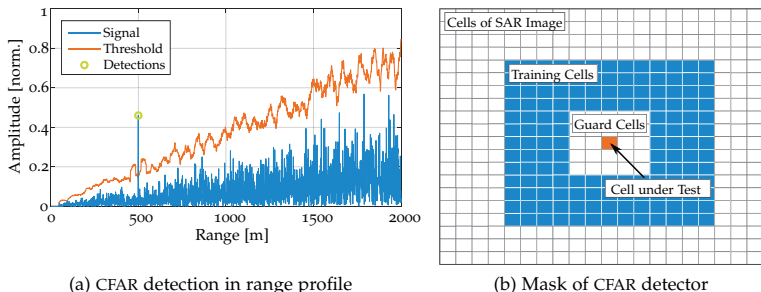


Figure 4.1: Visualization of CFAR detector.

which is used together with the noise power estimate $\hat{P}(x_i)$ to determine the threshold

$$T(x_i) = \alpha_{\text{cfar}} \hat{P}(x_i)$$

and finally to make the decision

$$\text{CFAR}(x_i) = \begin{cases} 1, & \text{if } \mathcal{A}(x_i) \geq T(x_i), \\ 0, & \text{else.} \end{cases}$$

The output of the CFAR detector is a binary image, where the value one indicates a target, in our case a ship. The value zero indicates the background. Extended versions of the CFAR detector use the maximum or the minimum, or even a statistical model, instead of the mean operation to compute the noise power estimate \hat{P} in Eq. (4.1). We use the standard implementation since the ship detection part is not the main part of this thesis. The case, where two or more ships are close to each other is not considered. Other state-of-the-art ship detection algorithms can be found in the literature [Cha+19; PLG10; Han+10].

By using simple morphological open and close operations, the output of the CFAR detector can be stabilized and each pixel, which belongs to a ship, can be identified. The a-priory knowledge that a ship does not extend the size of 300 m, helps to separate all ships from each other and to estimate their coarse center locations. This is sufficient since the proposed autofocus algorithm of large ships assumes that only one ship is inside the local image. It is not necessary that the ship is located exactly in the middle of the local SAR image.

4.2 SIGNAL MODEL OF A MOVING SHIP

In this section, we draw our attention to the range-compressed data of a moving ship. In order to formulate the signal model of a single ship with arbitrary motion, we extend the range-compressed data of the static scene, which was described in Sec. 2.2, to the non-static case.

Let the APC of an airborne single-channel X-band SAR system move along an arbitrary flight path $\gamma : \mathcal{L} \rightarrow \mathbb{R}^3$. We assume that the reflectivity function \mathcal{R} depends not only on \mathbf{x} , but also on the slow-time s . Then, the extended formulation

$$d(t, s) \approx \int_{\Omega} F_{\text{ant}}(\mathbf{x}, s) \mathcal{R}(\mathbf{x}, s) \text{ si}(\pi B(t - 2/c \cdot \|\gamma(s) - \mathbf{x}\|_2)) \cdot \exp(-4\pi i f_c/c \cdot \|\gamma(s) - \mathbf{x}\|_2) d\mathbf{x} \quad (4.2)$$

of the range-compressed data [CW05] for fast-time $t \in \mathcal{T}$ and slow-time $s \in \mathcal{L}$ is equivalent to the formulation in Eq. (2.8) except of the function $\mathcal{R} : \Omega \times \mathcal{L} \rightarrow \mathbb{C}$. Here, the surface $\Omega \subset \mathbb{R}^3$, especially each $\mathbf{x} \in \Omega$, represents the surface of the sea together with the three-dimensional shape of the ships. Remember that $F_{\text{ant}} : \Omega \times \mathcal{L} \rightarrow [0, 1]$ is the antenna footprint, the si-function is the point-spread function, B the chirp bandwidth, c the speed of light and f_c the carrier frequency.

In the following, we restrict the general signal model of the range-compressed data d , formulated in Eq. (4.2), to the case, where only one moving ship is illuminated. For this purpose, we firstly reduce the area of interest from the illuminated sea surface Ω to the subarea $\mathcal{S} \subset \Omega$, which contains only the three-dimensional shape of the ship. Additionally, we consider only that part of the entire observation time interval \mathcal{L} , where the ship is completely illuminated by the sensor, which we call *coherent processing interval* (CPI) $\mathcal{L}_{\text{CPI}} \subset \mathcal{L}$ of the ship. In the case of a spotlight scenario, the CPI of the ship and the entire observation time interval \mathcal{L} coincides. Both restrictions enable us to neglect the antenna footprint F_{ant} in Eq. (4.2), since the ship is illuminated during the entire CPI, which means

$$F_{\text{ant}}(\mathbf{x}, s) = 1 \quad \text{for } \mathbf{x} \in \mathcal{S}, s \in \mathcal{L}_{\text{CPI}}.$$

Moreover, we assume that for $s \in \mathcal{L}_{\text{CPI}}$ the reflectivity \mathcal{R} of the considered ship does not depend on the aspect angle. In other words, we assume that the amplitude of the reflected signal of one point reflector is the same for all angles. Hence, the reflectivity \mathcal{R} is only influenced by the motion of the ship, especially by the deformation $D : \mathcal{S} \times \mathcal{L}_{\text{CPI}} \rightarrow \mathbb{R}^3$, by the rotation $\mathbf{R} : \mathcal{S} \times \mathcal{L}_{\text{CPI}} \rightarrow \mathbb{R}^3$ and by the translation $\mathbf{T} : \mathcal{S} \times \mathcal{L}_{\text{CPI}} \rightarrow \mathbb{R}^3$.

The ship moves in azimuth, in range and in height. It additionally turns around pitch, roll and yaw and suffers deformations, which altogether are influenced by its velocity, its track and the sea waves. We introduce a variable substitution

$$x = (T \circ R \circ D)(\tilde{x}, s) = R(D(\tilde{x}, s), s) + t(s) =: M(\tilde{x}, s),$$

where \tilde{x} belongs to the reference Cartesian coordinate system with origin at the ship center at slow-time $s = 0$. Here, $M : \mathcal{S} \times \mathcal{L}_{\text{CPI}} \rightarrow \mathbb{R}^3$ describes the motion of the ship including deformations, rotations and translations and $t : \mathcal{L}_{\text{CPI}} \rightarrow \mathbb{R}^3$ represents the translation T , which does not depend on the space. Thus, the reflectivity \mathcal{R} of the ship can be rewritten in

$$\mathcal{R}(x, s) = \mathcal{R}(M(\tilde{x}, s), s) = \mathcal{R}(\tilde{x}, 0) =: \mathcal{R}_0(\tilde{x}),$$

where now $\mathcal{R}_0(\tilde{x})$ is static in time [SO18]. The interpretation of this variable substitution is the following: let us consider a reference three-dimensional grid, where \tilde{x} describes the shape of the ship, i.e., the surface of the ship at time $s = 0$. Then, the current position and the current shape of the ship, which is deformed, rotated and translated, can be computed for an arbitrary $s \in \mathcal{L}_{\text{CPI}}$ from the static reference grid by applying the non-linear motion M , i.e., the non-linear coordinate transformation. By considering only the area $\mathcal{S} \subset \Omega$, the interval $\mathcal{L}_{\text{CPI}} \subset \mathcal{L}$ and the static reflectivity \mathcal{R}_0 , the range-compressed data in Eq. (4.2) reduces to

$$\begin{aligned} d(t, s) \approx \int_{\mathcal{S}} \mathcal{R}_0(\tilde{x}) \operatorname{si}(\pi B(t - 2/c \cdot r(\tilde{x}, s))) \\ \cdot \exp(-4\pi i f_c/c \cdot r(\tilde{x}, s)) d\tilde{x} \end{aligned} \quad (4.3)$$

for $t \in \mathcal{T}$ and $s \in \mathcal{L}_{\text{CPI}}$, where the distance r is defined by

$$r(\tilde{x}, s) := \|\gamma(s) - M(\tilde{x}, s)\|_2. \quad (4.4)$$

In summary, Eqs. (4.3) and (4.4) describe how we generate range-compressed data of a single ship with arbitrary motion including deformations, rotations and translations. It can also be seen from Eqs. (4.3) and (4.4) that the arbitrary motion of a ship impacts only the relative distances between the sensor and the moving object. In the next section, we present the effects of an arbitrary motion of a large tanker on the reconstructed SAR image.

4.3 EFFECTS OF ARBITRARY MOTION ON SAR IMAGES

We show in this section that moving ships are displayed smeared, shifted and deformed in a SAR image depending on their specific motion. In the case of a small moving target, which has a size of approximately a few meters, only the smearing and the shift are discussed in the literature. It is usually assumed that the target moves linearly during the CPI, i.e., with constant velocity in a certain direction parallel to the ground plane. In such a case, the smearing results from the azimuth motion and the shift comes from the linear motion in range. If accelerations occur, this separation cannot be done anymore. The situation differs from this case if the object is larger than a few meters. In such a scenario, the large object is deformed due to its motion.

In the following, we analyze the shift, the smearing and the deformation by showing the effects of typical ship motions on SAR images using synthetic data. For this purpose, we simulate synthetic data of a large maneuvering tanker using Eq. (4.3) and show the resulting images, one for each kind of motion. We simulate a single-channel X-band SAR system with parameters listed in Tab. 4.1. The simulated system is similar to the *SmartRadar* [Kir+16] described in Sec. 2.6, which is later used for the evaluation of our proposed autofocus method. We simulate a straight flight path and do not consider antenna position errors of the INS in this section.

Table 4.1: Parameter of simulated X-band SAR system.

Parameter	Value
Carrier Frequency	9.6 GHz
Chirp Bandwidth	200 MHz
Pulse Duration	50 μ s
Sampling Frequency	400 MHz
Pulse Repetition Frequency	830 Hz
Squint Angle	0.0°
Depression Angle	20.0°
Slant Range	21 200 m
Coherent Processing Time	2 s
Aircraft Velocity	100 m/s

The simulated tanker in Fig. 4.2 has a length of 200 m as well as a width of 60 m and is described point-wise by 274 perfect point reflectors. Its front looks directly to the radar such that its direction of motion is orthogonal to the flight path.

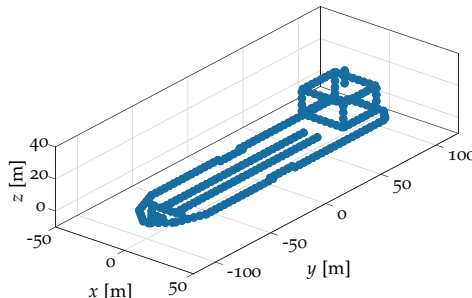


Figure 4.2: Three-dimensional model of simulated tanker. Each dot acts as a perfect point reflector. The synthetic data is simulated by Eq. (4.3).

If the ship runs at full speed, its translational motion is almost linear for a short CPI of 2 s. In the case of a rough sea with high waves, the rotational motion and the deformations are non-linear, i.e., sinusoidal. That is why we simulate a linear translational motion as well as a sinusoidal rotation and a sinusoidal deformation in time together with a quadratic deformation along the ship in space, named a hogging deformation. These motions are typical for large tankers in the case of a rough sea [WD12; LDC14]. We chose a roll, pitch and yaw period of 8 s such that the ship suffers one quarter of the sinusoidal rotation during the CPI [WD12]. The simulated translational velocities and the simulated rotations are given in Tab. 4.2. Thus these rotations and the deformations contain accelerations, whereas the translational motion has a constant velocity.

Table 4.2: Typical values of motion parameters.

Surge	Sway	Heave	Roll	Pitch	Yaw	Hogging
3 m/s	3 m/s	1 m/s	5°/s	2°/s	2°/s	2°/s

Fig. 4.3 shows four SAR images, one of the static tanker as the reference and three of the tanker with a linear motion in each of the three directions, respectively. The results of the rotational motions and the deformations are depicted in Fig. 4.4. A perfectly focused SAR image, see Fig. 4.3 (a), is reconstructed if the ship does not move. If the ship drives at full speed with 3 m/s directly in range direction, which is called a surge motion, it is shifted by 600 m along the azimuth axis as shown in Fig. 4.3 (b). The visible slight turn occurs since the ship is larger than a few meters. Strictly speaking, each point reflector has a marginal different radial

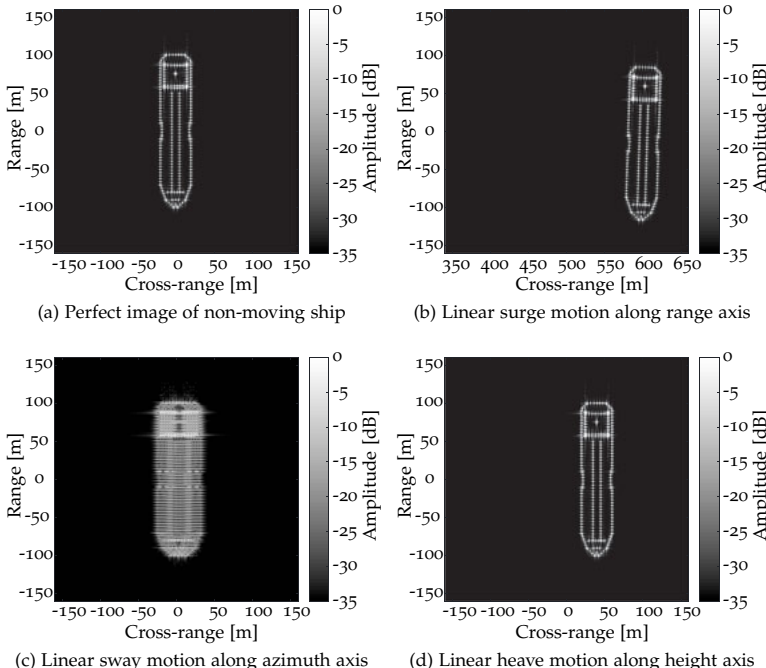


Figure 4.3: SAR images of a simulated moving tanker. In (a) the ship does not move. The images (b) – (d) consider a linear motion along range, along azimuth and along height, respectively. The motion in range and in height lead to a shift and a slight turn. The motion in azimuth smears the image.

motion component, such that each reflector has a marginal different shift, resulting in a slight turn of the ship. A linear motion of 3 m/s in azimuth direction, called sway motion, results in Fig. 4.3 (c), where the typical smearing can be seen. Fig. 4.3 (d) shows the result of a heave motion, i.e., a linear motion with 1 m/s in height. This motion leads to a small shift along azimuth and a marginal turn, similar to the surge motion.

In summary, all of these effects can be explained by the following well-known rule: since a radar sensor measures basically the radial distance to an object, only the radial component of the motion effects the resulting image. A linear radial motion of a point reflector results in a shift. Higher order radial motions of a point reflector result in smearings. If an object is larger than a few meters, the different radial motion components of

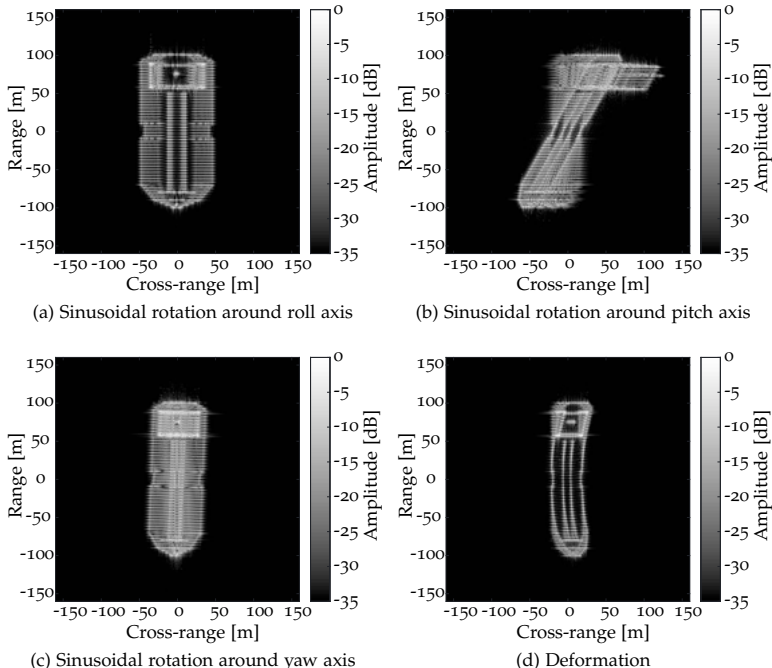


Figure 4.4: SAR images of a sinusoidal rotation and deforming tanker. In (a) – (c) the ship rotates around roll, pitch and yaw. In (d) the ship suffers deformations. In each image the size of the ship does not coincide with its true size. All images are partly smeared.

different parts of the object lead to different shifts in azimuth and thus to a deformation.

A little bit different is the situation in Fig. 4.4, where sinusoidal rotational motions are considered. Since each sinusoidal rotation and the sinusoidal deformation contain radial accelerations, all four images are partly smeared. The $5^\circ/\text{s}$ sinusoidal roll motion results in a change of the width of the ship and strong smearings in Fig. 4.4 (a). The $2^\circ/\text{s}$ rotation around the pitch axis leads to a deformation as well as to a turn of the ship and some smearings in Fig. 4.4 (b). If the ship turns $2^\circ/\text{s}$ around yaw, the effect is similar to the effect from a roll rotations, see Fig. 4.4 (c). The real deformation results in a visible deformation in Fig. 4.4 (d).

However, usually all kinds of motions are present in practice, such that the image is often smeared, shifted and deformed. A SAR image of a ship, where all considered motions are present is shown later in Fig. 4.5 (a).

Hence, the width and the length of a ship in a SAR image is not always equal to the true width and the true length of the ship. It can clearly be seen, that without any adjustments to the reconstruction algorithm, i.e., the GBP algorithm, the type of the ship cannot be identified reliably, since it is heavily smeared.

4.4 OPTIMAL FOCUS USING TRUE MOTION

We show in this part of the thesis that a perfect reconstruction of a moving ship is possible, if and only if the motion of the ship is known exactly and if additionally the reconstruction algorithm takes this motion into account. The GBP algorithm is perfectly suited to this task, because it has the capability to translate, to rotate and to deform the image grid for each slow-time sample individually. Hence, the GBP algorithm is able to project the data onto an arbitrarily moving grid, which is one of the most important differences to frequency-domain algorithms. In order to get a focused image, the image grid has to move exactly the same way the ship moves.

In the following, we give a precise formulation of how to include the motion of a ship into the GBP algorithm. We remind the reader that the core of the GBP algorithm is the equation

$$\mathcal{R}(x_i) = \sum_{m=1}^M d_m(2/c \cdot r_m(x_i)) \exp(4\pi i f_c/c \cdot r_m(x_i)), \quad (4.5)$$

where the range distances are originally computed by

$$r_m(x_i) = \|\gamma_m - x_i\|_2. \quad (4.6)$$

Equation (4.5) is equivalent to Eq. (2.10) in Sec. 2.3. In Eq. (4.5), the complex valued reflectivity \mathcal{R} is computed at the fix three-dimensional pixel-coordinates x_i for $i = 1, \dots, N_{\text{pix}}$. It is computed by the sum of M interpolated and phase corrected range profiles d_m , where c is the speed of light, f_c the carrier frequency and γ_m the aperture positions for $m = 1, \dots, M$. Since we do not know the three-dimensional shape of the ship, we assume that its image and thus the ship itself is flat with height $z = 0$.

We showed in Sec. 4.2 that deformations, rotations and translations of the ship affect only the radial distances between the APC and each part of the ship. With regard to our proposed autofocus technique, which use small range corrections to refocus a SAR image, we model the deformations, the rotations and the translations of the ship by the relative changes in the radial distances between the APC and the moving ship.

Hence, we model a moving and deforming grid in the GBP algorithm as a change in the radial distance between the aperture position γ_m and each reference pixel coordinate \tilde{x}_i for $i = 1, \dots, N_{\text{pix}}$. We show in the following that adjusting the radial distances due to the motion of the ship leads to a perfectly focused ship.

Let us assume that a local area $\mathcal{M} \subset \Omega$ around a single ship as well as the interval $\mathcal{L}_{\text{CPI}} \subset \mathcal{L}$ have been identified previously by the CFAR detector as described in Sec. 4.1. Let us additionally assume that the aperture positions γ_m are known exactly for all $m = 1, \dots, M$. Then, the distances r_m in Eq. (4.6) can be expressed by the sum of the estimated distance \hat{r}_m and the change in radial distance r_m^ϵ . Hence, the constant reflectivity \mathcal{R}_0 at \tilde{x}_i is computed by

$$\begin{aligned} \mathcal{R}_0(\tilde{x}_i) = & \sum_{m=1}^M d_m \left(2/c \cdot (\hat{r}_m(\tilde{x}_i) + r_m^\epsilon(\tilde{x}_i)) \right) \\ & \cdot \exp \left(4\pi i f_c/c \cdot (\hat{r}_m(\tilde{x}_i) + r_m^\epsilon(\tilde{x}_i)) \right) \end{aligned} \quad (4.7)$$

using the GBP algorithm. The first term

$$\hat{r}_m(\tilde{x}_i) = \|\hat{\gamma}_m - \tilde{x}_i\|_2$$

describes the static distance from the measured aperture position $\hat{\gamma}_m$ to the i th pixel. The second term represents the range errors $r_m^\epsilon(\tilde{x}_i)$ and is defined by

$$r_m^\epsilon(\tilde{x}_i) = \|\hat{\gamma}_m - \gamma_m^\epsilon - \tilde{x}_i\|_2 - \|\hat{\gamma}_m - \mathbf{R}_m \mathbf{D}_m(\tilde{x}_i) - \mathbf{t}_m\|_2, \quad (4.8)$$

where \mathbf{D}_m is the discretized deformation, \mathbf{R}_m the rotation and \mathbf{t}_m the translation. The range errors $r_m^\epsilon(\tilde{x}_i)$ include the non-linear motion of the ship and the correction of the antenna position errors γ_m^ϵ of the INS. Both terms, or at least the resulting errors $r_m^\epsilon(\tilde{x}_i)$, have to be known exactly for all $m = 1, \dots, M$ and all $i = 1, \dots, N_{\text{pix}}$ in order to reconstruct a perfectly focused image. This is the way we include the non-linear motion of the ship into the GBP algorithm.

To show that the proposed formulation above leads indeed to a focused SAR image, we present results of the simulated arbitrarily moving tanker from Sec. 4.3. The resulting SAR image of the GBP algorithm without any adjustments is shown in Fig. 4.5(a). It is heavily deformed and smeared, such that the type of the ship cannot be identified. Even the size of the ship is different to its true size. Taking the true motion of the ship modeled by the changes of the radial distances into account, results in the SAR image in Fig. 4.5(b). The deck of the ship, which is the main part, is perfectly focused. Only the superstructures, i.e., the driver's cabin and

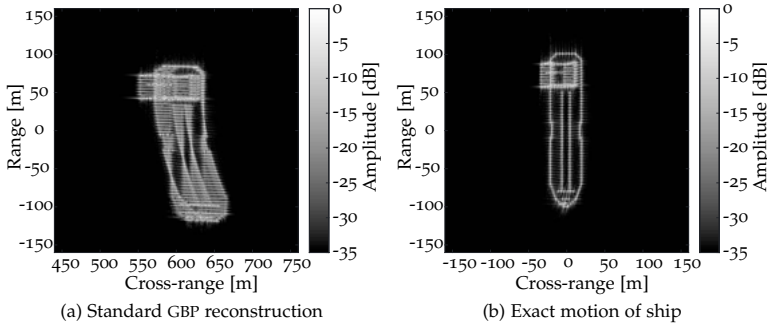


Figure 4.5: SAR images of the simulated moving ship. In (a) no adjustments on the algorithm are made. The image in (b) is reconstructed by using the exact simulated motion to the ship. Only the driver's cabin is still smeared.

the mast in front of the ship, are smeared. The reason is their different motions in comparison to the deck due to their height.

In summary, if the deformations D_m , the rotations R_m and the translations t_m of the ship as well as the antenna position errors γ_m^ϵ are perfectly known, the range errors $r_m^\epsilon(\tilde{x}_i)$ can be computed exactly for all $m = 1, \dots, M$ and $i = 1, \dots, N_{\text{pix}}$. In such an ideal scenario, the entire ship, which lies on a plane except their superstructure, can be reconstructed perfectly. However, the range errors $r_m^\epsilon(\tilde{x}_i)$ are usually unknown in practice and have to be estimated automatically. The task of estimating and correcting these range errors can be treated as an autofocus problem, where the range errors are usually much larger than one-half of the range-resolution and they additionally depend not only on the slow-time m , but also on the pixel locations \tilde{x}_i . How state-of-the-art autofocus techniques [MBH05; Ash12] estimate the range errors $r_m^\epsilon(\tilde{x}_i)$ and which approximations they do is described in the next section.

4.5 STATE-OF-THE-ART AUTOFOCUS OF SHIPS

Many different autofocus techniques exist in the literature [HEGJJ89; DL13; MS81; Ash12; Wer+90; MBH05; NFM15]. Some of them have been invented for classical SAR applications and some have been invented especially to focus moving ships. However, most of them are connected to frequency-domain algorithms such that they are only able to estimate low-order phase terms or they are limited to straight flight path scenarios. For example, the phase gradient algorithm [HEGJJ89] requires linear platform

motion and isolated bright targets [DL13]. The mapdrift autofocus [MS81] is only able to compensate low-order phase terms [DL13] and can only be applied to data aquired along a straight flight path [DL13]. The prominent point processing [Wer+90] is able to estimate rotational motions [DL13]. However, it requires continuously visible prominent points on the ship, which can rarely be found in practice. Hence, the classical autofocus techniques cannot be used to focus ships with arbitrary motions.

The autofocus algorithms, which have been invented to refocus the images of moving ships, usually describe their motion by two parameters, i.e., their radial velocity and their radial acceleration. Martorella et al. [MBH05] estimate the radial velocity and the radial acceleration by maximizing image contrast. A similar approach is taken by Noviello et al. [NFM15]. They estimate the Doppler centroid and the Doppler rate as representatives of the radial velocity and the radial acceleration of a ship. Both methods assume that the radial motion of a ship can be described by a second order polynomial. However, they do not consider rotational motions and their algorithms are connected to frequency-domain algorithms and thus limited to straight flight path scenarios.

Another class of SAR autofocus techniques is the class of methods for time-domain reconstruction algorithms, especially for the GBP algorithm. They preserve full flexibility and avoid limitations on the flight path. A well known state-of-the-art time-domain autofocus algorithm is the backprojection autofocus by Ash [Ash12], which we described in Sec. 2.5 in detail. It allows the estimation of one-dimensional arbitrary phase functions and the processing of data received along arbitrary flight paths. A similar but slower approach is given by Duersch et al. [DL13].

In the following, we describe the autofocus of ships by Martorella et al. [MBH05] and recap the idea of the autofocus by Ash [Ash12]. The backprojection autofocus by Ash [Ash12] improves the focus by estimating phase errors based on maximizing image sharpness. Ash assumes that the range errors $r_m^\epsilon(\tilde{x}_i)$ in Eq. (4.8) are equal for all $i = 1, \dots, N_{\text{pix}}$ pixels and additionally less than one-half of the range-resolution for all $m = 1, \dots, M$. Thus, the range errors $r_m^\epsilon(\tilde{x}_i)$ can be approximated by phase errors ϕ_m^ϵ in the following way:

$$r_m^\epsilon(\tilde{x}_i) \approx r_m^\epsilon = \frac{c}{4\pi f_c} \cdot \phi_m^\epsilon.$$

Hence, only M phase errors ϕ_m^ϵ instead of $M \cdot N_{\text{pix}}$ range errors $r_m^\epsilon(\tilde{x}_i)$ have to be estimated in order to correct the smeared SAR image. The main idea of the Ash autofocus [Ash12] is the estimation of each component

of the stacked phase error vector $\phi^\epsilon = (\phi_1^\epsilon, \dots, \phi_M^\epsilon)^\top$ sequentially by solving the non-linear least squares problem

$$\hat{\phi}_m^\epsilon = \arg \max_{\phi_m^\epsilon \in (-\pi, \pi]} S(\phi_m^\epsilon) \quad (4.9)$$

for all $m = 1, \dots, M$, where $S : (-\pi, \pi] \rightarrow \mathbb{R}_+$ is the image sharpness cost function

$$S(\phi_m^\epsilon) = \sum_{i=1}^{N_{\text{pix}}} |\mathcal{I}(\tilde{\mathbf{x}}_i, \phi_m^\epsilon)|^2. \quad (4.10)$$

Ash [Ash12] was able to formulate a closed-form solution of the non-linear Eq. (4.9). This autofocus method yields good results, if the range errors are less than one-half of the range-resolution and if the estimated flight path is a good estimate. However, ships on the open sea move usually more than one-half of the range-resolution of a few centimeters within the SAR observation time of several seconds. This makes the reconstruction of a sharp SAR image of a moving ship using the backprojection autofocus by Ash [Ash12] difficult.

The image-contrast-based technique (ICBT) by Martorella et al. [MBH05] is a well-consolidated method for refocusing moving ships [NFM15]. Thus, it serves in this thesis as the state-of-the-art reference algorithm. The general idea of the algorithm is to estimate one radial velocity value v_r and one radial acceleration value a_r of the motion of the ship for the entire CPI by maximizing image contrast, see Sec. 2.4. To be precise, the optimization problem

$$(\hat{v}_r, \hat{a}_r) = \arg \max_{v_r, a_r} \text{IC}(v_r, a_r) \quad (4.11)$$

has to be solved, where the image contrast IC depends on the radial velocity v_r and the radial acceleration a_r and is defined by

$$\text{IC}(v_r, a_r) = \frac{\sqrt{\frac{1}{N_{\text{pix}}} \sum_{i=1}^{N_{\text{pix}}} (\mathcal{I}(\tilde{\mathbf{x}}_i, v_r, a_r) - \frac{1}{N_{\text{pix}}} \sum_{i=1}^{N_{\text{pix}}} \mathcal{I}(\tilde{\mathbf{x}}_i, v_r, a_r))^2}}{\frac{1}{N_{\text{pix}}} \sum_{i=1}^{N_{\text{pix}}} \mathcal{I}(\tilde{\mathbf{x}}_i, v_r, a_r)} \quad (4.12)$$

equivalent to Eq. (2.12). The ICBT autofocus algorithm by Martorella et al. [MBH05] was originally implemented in the framework of frequency-domain algorithms. To use the ICBT in our backprojection framework, we test several radial velocity values and several radial acceleration values and chose the pair, which results in the highest image contrast. Hence, no qualitative statements about the computational costs of the ICBT are

given in this thesis. However, the ICBT algorithm is much faster than all GBP autofocus algorithms, because the frequency-domain image reconstruction algorithms are much faster than the GBP image reconstruction algorithm.

Altogether, all state-of-the-art autofocus techniques require an almost linear motion of the ship or data of prominent points on the ship. However, linearly moving ships and prominent points can rarely be found in practice. One possibility to deal with this problem is to process only data from a short CPI, such that the motion of the ship is almost linear. The drawback of this strategy is that the short CPI lowers the resolution in azimuth and thus the image quality drastically. Until now, no autofocus technique is able to estimate non-linear motions of a ship for a long CPI to offer the necessary image quality for a robust classification of maritime objects.

4.6 EXTENDED AUTOFOCUS ALGORITHM OF LARGE SHIPS

In this section, we propose an extended autofocus technique, which focuses large arbitrarily moving and maneuvering ships with high quality. Our technique uses the framework of the GBP algorithm [And88; GM10] and the idea of estimating phase errors by maximizing image sharpness similar to Ash [Ash12]. In contrast to Ash, we divide the image into small subimages and estimate pulse-by-pulse one phase error for each subimage by maximizing subimage sharpness. An iterative Gauss–Newton optimization together with a minimum curvature regularization allows us to estimate smooth continuous phase functions on subimage level. A polynomial regression transfers the pulse-by-pulse estimated subimage phase errors to a smooth phase error function based on each pixel. We additionally propose to use the estimated phases of the currently considered pulse to estimate the global radial motion of the ship. This error propagation allows us to estimate an arbitrary motion of a ship without any limitations on their velocity.

Since the concept of our ship autofocus algorithm is to estimate pulse-by-pulse the distances from each aperture position to all pixels in the SAR image, we divide the CPI into two parts, see Fig. 4.6. The first part is used to generate an initial SAR image $\bar{\mathcal{R}}_0$ of the ship by the standard GBP algorithm, see Sec. 2.3. This image serves as a registration basis for all subsequent pulses. The first time interval should be very short, for example 0.5 s, because our autofocus method in the second part works best if the motion of the ship is almost linear in the first part. The second part of the CPI is used to estimate and to correct pulse-by-pulse the phases

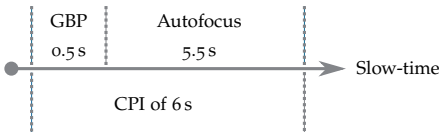


Figure 4.6: Decomposing of CPI into GBP part and autofocus part.

of all backprojected range profiles such that they fit perfectly to the initial image \bar{R}_0 .

An overview of the proposed autofocus algorithm is visualized in the flow-chart in Fig. 4.7. We take the initial SAR image \bar{R}_0 and decompose it into K subimages. The subimages which belong to the ship and not to the background are identified by an amplitude threshold decision such that K_0 relevant subimages are used further on. The range correction is only applied, if previous phase errors have been estimated. The core of the autofocus algorithm is the subimage phase error estimation, where for each subimage one phase error is estimated by maximizing subimage sharpness. These phase errors are additionally forced to be smooth between the subimages. Next, these estimated phase errors are interpolated to all pixels by quadratic regression and applied to the backprojected pulse in the phase correction block. These phase corrections are converted to range corrections to correct the distances from all subsequent aperture positions to all pixels. This range corrections are applied, before the next pulse is considered.

In contrast to our method, the backprojection autofocus by Ash [Ash12] consists only of the pulse-by-pulse phase error estimation based on the unfocused SAR image and the phase correction part. Thus, nearly every block of the flow-chart in Fig. 4.7, which we explain in detail in the following, is an extension to the Ash autofocus [Ash12].

Let the initial SAR image \bar{R}_0 has been reconstructed by the GBP algorithm for N_{pix} pixels using 0.5s of the data. We decompose the local image area \mathcal{M} in K disjoint subareas $\mathcal{M}_1, \dots, \mathcal{M}_K$ with $\mathcal{M}_k \cap \mathcal{M}_l = \emptyset$ for $k \neq l$ and $k, l = 1, \dots, K$. Here, we choose rectangular subareas as visualized in Fig. 4.8 so that each subarea \mathcal{M}_k has the center $\tilde{x}_{\text{ctr}}^{(k)}$ and consists of N_{sub} pixels located at $\tilde{x}_1^{(k)}, \dots, \tilde{x}_{N_{\text{sub}}}^{(k)}$. By simply identifying the K_0 subimages, which have a maximum intensity greater than a specified threshold, computing their convex hull and using the open and closing morphological operations on the block image, the subareas which cover the ship are obtained. The center subarea is determined by computing the center of all relevant subarea centers $\tilde{x}_{\text{ctr}}^{(k)}$ for $k = 1, \dots, K_0$. This cen-

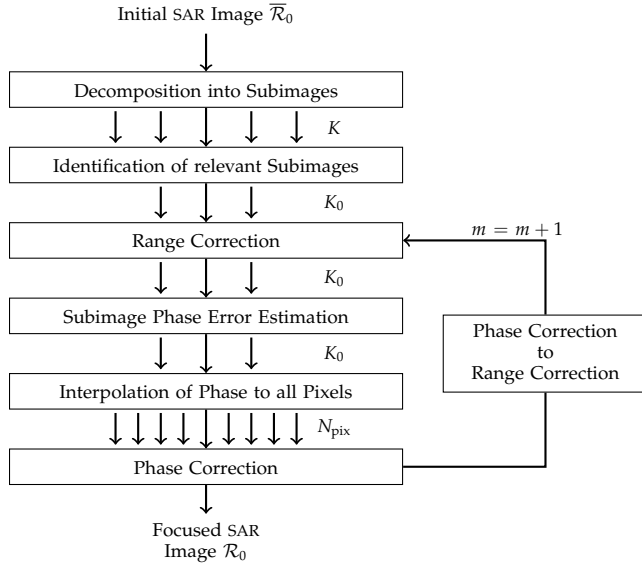


Figure 4.7: Overview of proposed ship autofocus algorithm.

ter subarea serves as a reference coordinate of the ship for the range correction described further below.

Similar to the backprojection autofocus by Ash [Ash12], we estimate the phase errors by maximizing image sharpness. However, we do it for each subimage separately instead of for the entire image. Thus, we find the estimated phase error vector $\hat{\phi}_m = (\hat{\phi}_m^{(1)}, \dots, \hat{\phi}_m^{(K_0)})^T$ by solving the non-linear least squares problem

$$\hat{\phi}_m = \arg \min_{\phi_m \in (-\pi, \pi]^{K_0}} \left\{ \frac{1}{2} \|S(\phi_m)\|_2^2 + \frac{\alpha}{2} \|D\phi_m\|_2^2 \right\}. \quad (4.13)$$

The non-linear vector function $S : (-\pi, \pi]^{K_0} \rightarrow \mathbb{R}_+^{K_0}$ measures the sharpness of each of the K_0 subimages when applying the phase corrections $\phi_m = (\phi_m^{(1)}, \dots, \phi_m^{(K_0)})^T$ to the image. In contrast to Ash, we use the negative sign of the sharpness function to formulate a minimization problem

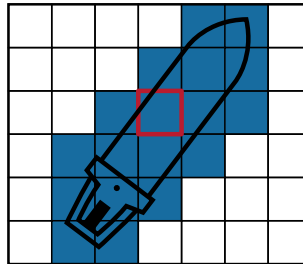


Figure 4.8: Decomposition of guard area \mathcal{M} into subareas \mathcal{M}_k . The blue filled subareas belong to the ship. The red bordered subarea indicates the center subarea.

instead of a maximization problem, compare Eq. (4.9). To be precise, our sharpness function in vector representation is

$$S(\phi_m) = \begin{pmatrix} v_m^{(1)} - a_m^{(1)} \cos(\phi_m^{(1)}) - b_m^{(1)} \sin(\phi_m^{(1)}) \\ \vdots \\ v_m^{(K_0)} - a_m^{(K_0)} \cos(\phi_m^{(K_0)}) - b_m^{(K_0)} \sin(\phi_m^{(K_0)}) \end{pmatrix} \quad (4.14)$$

for $\phi_m \in (-\pi, \pi]^{K_0}$. The vector function S is shortly denoted by $S(\phi_m) = (S_1(\phi_m^{(1)}), \dots, S_{K_0}(\phi_m^{(K_0)}))^T$. The values $a_m^{(k)}$, $b_m^{(k)}$ and $v_m^{(k)}$ are computed for all $k = 1, \dots, K_0$ subimages by

$$\begin{aligned} a_m^{(k)} &= \sum_{i=1}^{N_{\text{sub}}} 2 \operatorname{Re}(\mathcal{R}_m^C(\tilde{x}_i^{(k)}) \mathcal{R}_m^*(\tilde{x}_i^{(k)})), \\ b_m^{(k)} &= \sum_{i=1}^{N_{\text{sub}}} (-2) \operatorname{Im}(\mathcal{R}_m^C(\tilde{x}_i^{(k)}) \mathcal{R}_m^*(\tilde{x}_i^{(k)})), \\ v_m^{(k)} &= \sum_{i=1}^{N_{\text{sub}}} (|\mathcal{R}_m^C(\tilde{x}_i^{(k)})|^2 + |\mathcal{R}_m(\tilde{x}_i^{(k)})|^2). \end{aligned} \quad (4.15)$$

The matrix $D \in \mathbb{R}^{K_0 \times K_0}$ works as second order derivative of the phase corrections ϕ_m and ensures that the estimated phases between the subimages are smooth. It is implemented by the second order finite difference matrix according to a 5-point scheme. For the boundary subareas of all subareas, which cover the considered ship, we implement the first order finite difference matrix. We give here a simple example for a better

understanding. If an image is decomposed into 3×3 subimages, the matrix D reads

$$D = \begin{pmatrix} 2 & -1 & 0 & -1 & 0 & 0 & 0 & 0 & 0 \\ -1 & 3 & -1 & 0 & -1 & 0 & 0 & 0 & 0 \\ 0 & -1 & 2 & 0 & 0 & -1 & 0 & 0 & 0 \\ -1 & 0 & 0 & 3 & -1 & 0 & -1 & 0 & 0 \\ 0 & -1 & 0 & -1 & 4 & -1 & 0 & -1 & 0 \\ 0 & 0 & -1 & 0 & -1 & 3 & 0 & 0 & -1 \\ 0 & 0 & 0 & -1 & 0 & 0 & 2 & -1 & 0 \\ 0 & 0 & 0 & 0 & -1 & 0 & -1 & 3 & -1 \\ 0 & 0 & 0 & 0 & 0 & -1 & 0 & -1 & 2 \end{pmatrix}.$$

The regularization parameter $\alpha \in \mathbb{R}_+$ controls the tradeoff between stability and approximation. In our case it controls how well the phase corrections ϕ_m fit into a plane. Hence, by adjusting α and the number of subareas K_0 the true deformation of a large ship can be taken into account. Without the regularization controlled by α , a discontinuous phase correction between the subimages would result in unrecognizable SAR images.

We solve the non-linear Eq. (4.13) using iterative Gauss-Newton optimization. It is an iterative method based on the Taylor expansion, where in our case the system of linear equations

$$\begin{aligned} (J(\phi_m)^T J(\phi_m) + \alpha D^T W D + \mu W) \mathbf{h} = \\ - (J(\phi_m)^T S(\phi_m) + \alpha D^T W D \phi_m) \end{aligned} \quad (4.16)$$

is solved iteratively. Here, $J(\phi_m)$ is the Jacobian matrix, D the second order finite difference matrix, μ the update parameter, W a weighting matrix and \mathbf{h} the update term. The Jacobian matrix

$$J(\phi_m) = \begin{pmatrix} \frac{\partial S_1(\phi_m^{(1)})}{\partial \phi_m^{(1)}} & \mathbf{0} \\ & \ddots \\ \mathbf{0} & \frac{\partial S_{K_0}(\phi_m^{(K_0)})}{\partial \phi_m^{(K_0)}} \end{pmatrix}$$

is a diagonal matrix and has for $k = 1, \dots, K_0$ the entries

$$\frac{\partial S_k(\phi_m^{(k)})}{\partial \phi_m^{(k)}} = b_m^{(k)} \cos(\phi_m^{(k)}) - a_m^{(k)} \sin(\phi_m^{(k)}).$$

For a computational effective implementation, the vectors and the sparse matrices should be assembled during iteration, instead of using matrix multiplications. Therefore, the k th diagonal entry of the squared matrix $J(\phi_m)^T J(\phi_m)$ is

$$\begin{aligned} (J(\phi_m)^T J(\phi_m))_{kk} = \\ (a_m^{(k)} \sin(\phi_m^{(k)}))^2 + (b_m^{(k)} \cos(\phi_m^{(k)}))^2 \\ - 2 a_m^{(k)} b_m^{(k)} \sin(\phi_m^{(k)}) \cos(\phi_m^{(k)}). \end{aligned}$$

The k th entry of the vector $J(\phi_m)^T S(\phi_m)$ is given by

$$\begin{aligned} (J(\phi_m)^T S(\phi_m))_k = \\ a_m^{(k)} b_m^{(k)} (\cos^2(\phi_m^{(k)}) - \sin^2(\phi_m^{(k)})) \\ + ((b_m^{(k)})^2 - (a_m^{(k)})^2) \sin(\phi_m^{(k)}) \cos(\phi_m^{(k)}) \\ + a_m^{(k)} v_m^{(k)} \sin(\phi_m^{(k)}) - b_m^{(k)} v_m^{(k)} \cos(\phi_m^{(k)}). \end{aligned}$$

Furthermore, the values $a_m^{(k)}$, $b_m^{(k)}$ and $v_m^{(k)}$ can be computed for each pulse $m = 1, \dots, M$ and each subimage $k = 1, \dots, K_0$ in the preprocessing of the iterative Gauss-Newton algorithm by Eq. (4.15), because they do not depend on the phase ϕ_m . We run the iterative Gauss-Newton solver with a fix $\mu \in \mathbb{R}_+$. This step size control in combination with the weighting matrix W ensure that the estimated phases $\hat{\phi}_m$ are in $(-\pi, \pi]^{K_0}$. To balance all terms of Eq. (4.16), we choose the weighting matrix $W = J(\phi_m)^T J(\phi_m)$. We use the termination conditions

$$\begin{aligned} \|\mathbf{h}\|_2 \leq \varepsilon_0 (\|\phi_m\|_2 + \varepsilon_0), \\ k < k_{\max} \end{aligned}$$

with $\varepsilon_0 = 10^{-4}$ and $k_{\max} = 500$. The resulting phase errors $\hat{\phi}_m$ are visualized in Fig. 4.9.

Once, the estimation of the phase errors $\hat{\phi}_m$ for a fixed slow-time sample m is done, they are used to correct the phases of the current backprojected pulse. In order to avoid phase discontinuities at the boundaries of all subareas, we compute the phase corrections $\tilde{\phi}_m = (\tilde{\phi}_m^{(1)}, \dots, \tilde{\phi}_m^{(N_{\text{pix}})})^T$ for all pixels of the entire image from the estimated phase corrections $\hat{\phi}_m$ of all subimage using second order least squares polynomial regression. We use second order regression, because it allows us to describe and correct the real deformation of a ship by quadratic polynomials. Let $\mathbf{X}_{\text{sub}} = (\tilde{x}_{\text{ctr}}^{(1)}, \dots, \tilde{x}_{\text{ctr}}^{(K_0)})^T$ and $\mathbf{Y}_{\text{sub}} = (\tilde{y}_{\text{ctr}}^{(1)}, \dots, \tilde{y}_{\text{ctr}}^{(K_0)})^T$ be the x - and y -coordinates of the subarea centers and let $\mathbf{X} = (\tilde{x}_1, \dots, \tilde{x}_{N_{\text{pix}}})^T$ and

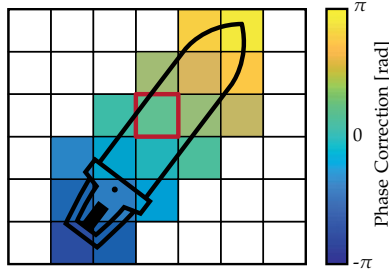


Figure 4.9: Smooth estimated phase errors on subimage level. The subimage with the red border represents the center of the ship.

$\mathbf{Y} = (\tilde{y}_1, \dots, \tilde{y}_{N_{\text{pix}}})^T$ be the vectors, which contain the coordinates of all pixels in the entire image grid. Then

$$\begin{aligned} \mathbf{A} &:= (\mathbf{1}, \mathbf{X}_{\text{sub}}, \mathbf{Y}_{\text{sub}}, \mathbf{X}_{\text{sub}}^2, \mathbf{Y}_{\text{sub}}^2), \\ (\alpha_0, \dots, \alpha_4)^T &= (\mathbf{A}^T \mathbf{A})^{-1} \cdot (\mathbf{A}^T \hat{\boldsymbol{\phi}}_m), \\ \tilde{\boldsymbol{\phi}}_m &= \alpha_0 + \alpha_1 \mathbf{X} + \alpha_2 \mathbf{Y} + \alpha_3 \mathbf{X}^2 + \alpha_4 \mathbf{Y}^2 \end{aligned}$$

give the interpolated phase corrections $\tilde{\boldsymbol{\phi}}_m = (\tilde{\phi}_m(\tilde{\mathbf{x}}_1), \dots, \tilde{\phi}_m(\tilde{\mathbf{x}}_{N_{\text{pix}}}))^T$ for all pixels. So far, we showed how to compensate small motions of a ship by multidimensional phase corrections.

However, a ship moves usually more than a few centimeters within the CPI of several seconds. Hence, phase corrections are not enough to compensate large motions in practice. Phase wrapping effects make the estimation of an optimal phase correction very complex. For example, if the rotation of a ship is large, the front of the ship moves differently than the back of the ship. Thus the phase errors between the front and the back can be larger than 2π . To avoid these phase wrappings or phase discontinuities and to ensure that $\tilde{\boldsymbol{\phi}}_m \in (-\pi, \pi]^{N_{\text{pix}}}$ holds for all $m = 1, \dots, M$, we convert the estimated phase corrections of the current pulse into range corrections and use them to correct the global radial motion of the ship. Correcting the radial motion is equivalent to adjusting the range distances $r_m^e(\tilde{\mathbf{x}}_i)$ from the aperture position $\hat{\mathbf{y}}_m$ to all pixels at $\tilde{\mathbf{x}}_i$ for $i = 1, \dots, N_{\text{pix}}$. Therefore, the phase corrections $\tilde{\phi}_m(\tilde{\mathbf{x}}_i)$ are converted to range corrections by

$$r_{m+1}^e(\tilde{\mathbf{x}}_i) = r_m^e(\tilde{\mathbf{x}}_i) + \frac{c}{4\pi f_c} \cdot \tilde{\phi}_m(\tilde{\mathbf{x}}_i)$$

for all $i = 1, \dots, N_{\text{pix}}$ pixels. This error propagation allows to adjust the orientation and the translation of a moving grid. This idea of continuously

updating the ranges from the aperture positions to all pixels could run into instabilities, which can be avoided by updating the range only periodically instead of pulse-by-pulse. In summary, the proposed ship autofocus technique allows us to reconstruct sharp images of moving ships even if they have a large non-linear motion.

4.7 EXPERIMENTAL RESULTS AND EVALUATION

We use real data to evaluate the behavior of the proposed autofocus algorithm for large ships and to compare its results with the results of the two state-of-the-art autofocus techniques by Martorella et al. [MBH05] and by Ash [Ash12]. The real data was recorded by the *SmartRadar*² (scalable modular aero-space radar technology) [Kir+16] system, which is the same airborne single-channel X-band SAR system as used for the real data example in Sec. 2.6. Some characteristic parameters of the data set and some parameters of the geometry are listed in Tab. 4.3. The main difference to Sec. 2.6 is the reduced chirp bandwidth of 210 MHz and thus the reduced range-resolution of 71 cm, which is typical for maritime SAR applications for the sake of robustness. The radar was operating in stripmap mode.

Table 4.3: Parameters of data set [Kir+16] and stripmap geometry.

Parameter	Value
Carrier Frequency	9.6 GHz
Chirp Bandwidth	210 MHz
Pulse Duration	56 μ s
Sampling Frequency	300 MHz
Pulse Repetition Frequency	1790 Hz
Squint Angle	0.2°
Depression Angle	32.3°
Slant Range	20 000 m
Aircraft Velocity	154 m/s

In order to compare and evaluate our proposed algorithm with the two described state-of-the-art autofocus algorithms by Martorella et al. [MBH05] and by Ash [Ash12], we use the peak power value, the image contrast, the image entropy and the computational costs. All of these image quality metrics have been introduced in Sec. 2.4. A high peak

² Data was kindly provided by the Hensoldt Sensors GmbH (formerly AIRBUS - Defence and Space)

power value indicates a well-focused scatterer. A well-focused image has a large image contrast, which means that the difference between dark and bright pixels is large. On the contrary, a low image entropy suggests a well-focused image. Furthermore, we normalize the computational costs by the computational costs of the GBP algorithm. For example, costs of 1.5 mean that the entire reconstruction including the autofocus needs 1.5 times the costs of the GBP. Since the ICBT autofocus [MBH05] was integrated into the backprojection framework, no qualitative statements about its original computational costs are given in this evaluation. However, the ICBT autofocus is much faster than the GBP autofocus algorithms.

4.7.1 *Autofocus of a Large Tanker*

In this first case study, we reconstruct a SAR image of a large tanker, which belongs to the Amundsen class [Amu09] and has a length of 250 m as well as a width of 42 m. It drove with approximately 6.8 m/s away from the sensor. The sea state was rough with sea state code 5 and 2.5 – 4 m high waves on the day of the flight campaign.

We choose an image grid of 800×800 pixels with a spacing of 30×30 cm, which is divided into 20×20 subareas. It turned out that 20 subareas in each dimension are suitable for all scenarios. Too many subareas would result in unrealistic and degenerated images. Too few subareas would prevent the algorithm from estimating the non-linearity of the phase corrections. Furthermore, we use a CPI of 6 s, which is relatively long for the application of imaging maritime objects, because during 6 s the motion of a ship is mostly non-linear. The GBP algorithm implemented in Matlab took 10 min and 20 s on a work station with a 3.6 GHz 8-Core processor and 64 GB RAM in single-thread mode. Thus, 10 min and 20 s is in this case the GBP reference time.

The result of the state-of-the-art ICBT autofocus by Martorella et al. [MBH05] and the result of the backprojection autofocus by Ash [Ash12] are shown in Fig. 4.10 and in Fig. 4.11, respectively. Details about their implementations are described above in Chap. 4.5. Our proposed ship autofocus leads to the result in Fig. 4.12.

From a visual point of view, only Fig. 4.12 is well focused, because details on deck like the bollards are visible only in this figure. In Fig. 4.11 only the driver's cabin is almost focused, whereas in Fig. 4.10 the whole ship is smeared. The front and the back of the ship are overlayed by noise in all three cases. The noise comes from different motions of superstructures in comparison with the deck and from multipath propagations.

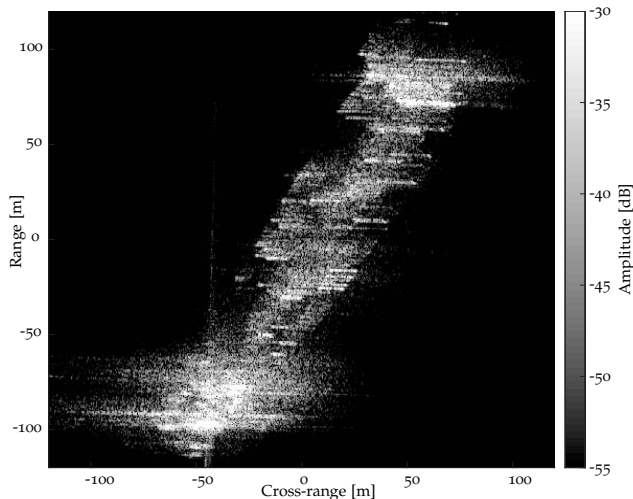


Figure 4.10: Result of tanker at speed 6.8 m/s from case study A using the ICBT autofocus by Martorella et al. [MBH05].

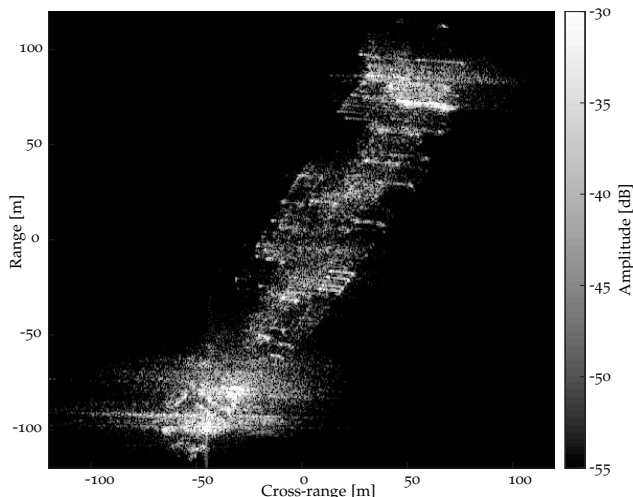


Figure 4.11: Result of tanker at speed 6.8 m/s from case study A using the back-projection autofocus by Ash [Ash12].

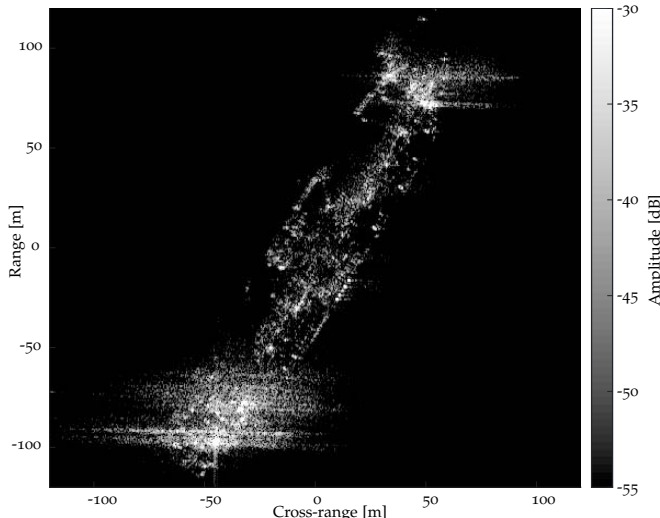


Figure 4.12: Result of tanker at speed 6.8 m/s from case study A using our proposed autofocus.

The numerical evaluation in Tab. 4.4 confirms that the image in Fig. 4.12 is much better focused than the images in Fig. 4.10 and 4.11. The peak power, the image contrast and the image entropy show a significant improvement of image quality using our method. In particular, only our algorithm leads to the accuracy, which is necessary for the characterization of the ship type on a windy day.

Table 4.4: Numerical results of case study A (large tanker).

	No	ICBT	Ash	Ours
Peak Power	455	2 713	4 196	5 075
Contrast	2.64	3.96	3.98	4.57
Entropy	9.92	7.89	7.48	6.81
Costs (norm.)	1	—	3.17	1.31

4.7.2 Autofocus of a Large Bulk Carrier

In this second case study, we consider a large bulk carrier, which has a length of 218 m and a width of 32 m. The sea state was slight meaning 0.5 – 1.25 m high waves and the ship lied at anchor. Thus, the motion of the ship is less than the considered motion in the first case study, such that we choose again a long CPI of 6 s. The reconstructed SAR image, which is divided again into 20×20 subareas, has 800×600 pixels with a spacing of again 30×30 cm. The reference GBP reconstruction took 8 min and 10 s.

The SAR images of the two state-of-the-art autofocus techniques [Ash12; MBHo5] and the result of our ship autofocus algorithm are shown in Fig. 4.13 – 4.15. It seems that the quality of all three images is similar, since the class of the ship can be identified in each image. However, the values of the quality metrics in Tab. 4.5 indicate that the ship, reconstructed by the proposed autofocus technique, is again better focused. The peak power, the image contrast and the entropy values are better in our case. A detailed look clarifies that the widespread background noise is lower in Fig. 4.15 than the noise in the images 4.13 and 4.14 and the front of the ship is sharper than in the two state-of-the-art reconstructions.

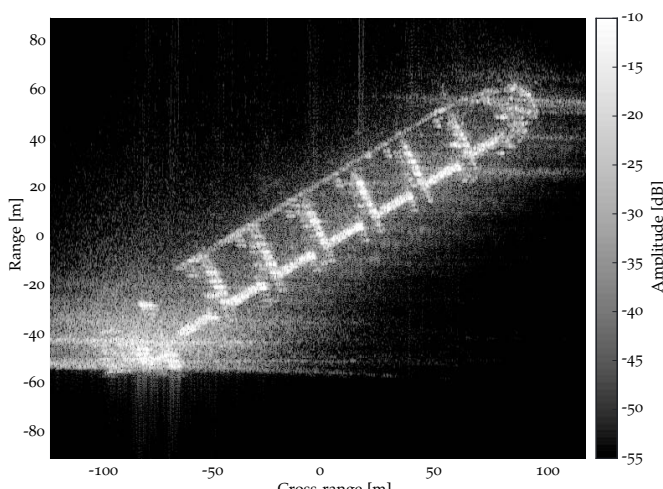


Figure 4.13: Result of an anchored bulk carrier at speed 0 m/s from case study B using the ICBT autofocus by Martorella et al. [MBHo5].

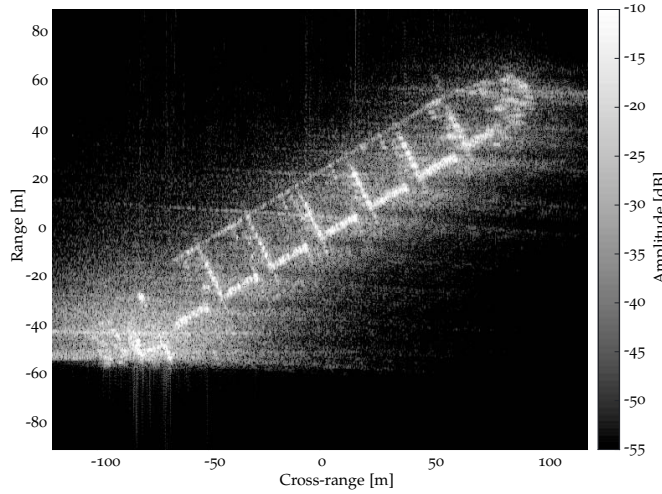


Figure 4.14: Result of an anchored bulk carrier at speed 0 m/s from case study B using the backprojection autofocus by Ash [Ash12].

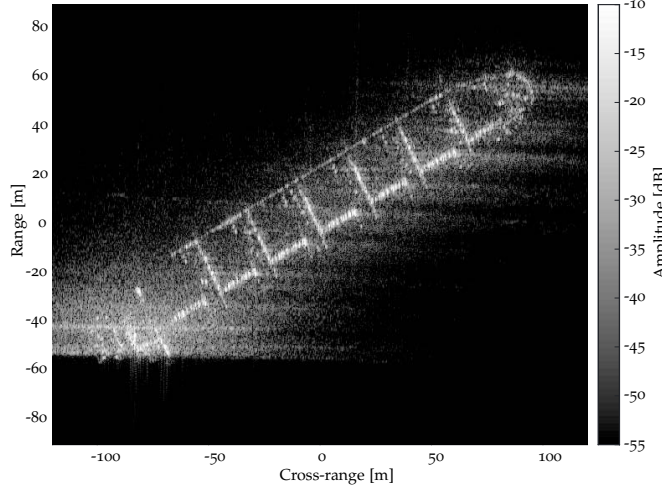


Figure 4.15: Result of an anchored bulk carrier at speed 0 m/s from case study B using our proposed autofocus.

In all three images, the driver's cabin is shifted in range due to its height, which comes from the SAR principle and the large depression angle. The clearly visible hatches identify the ship as bulk carrier in all three images.

Table 4.5: Numerical results of case study B (large bulk carrier).

	No	ICBT	Ash	Ours
Peak Power	174	362	432	685
Contrast	2.39	3.61	3.46	3.96
Entropy	10.55	9.23	9.05	8.42
Costs (norm.)	1	—	3.16	1.47

In summary, our algorithm reconstructs an image, where more details are visible than in the other two images. The type of the ship can be identified even in the image focused by state-of-the-art techniques [Ash12; MBH05], since the sea was almost flat in this case study.

4.7.3 Autofocus of a Self-Discharging Bulk Carrier

Now we consider a third ship, a self-discharging bulk carrier. The vessel has a length of 175 m as well as a width of 26 m and is thus smaller than the ships in both other case studies. It drove with 5.6 m/s in the direction of the flight path, where the sea state was rough again with 2.5 – 4 m high waves. We initialize the SAR image of this third ship by 800×600 pixels with a spacing of 30×30 cm and 20×20 subareas. In this case, we choose a short CPI of 3 s, because the ship has a highly non-linear motion due to its small size and the rough sea. The reference reconstruction of the SAR image using the GBP algorithm took exactly 5 min.

Fig. 4.16 – 4.18 show the results of all three techniques. It can be seen that both state-of-the-art autofocus techniques [Ash12; MBH05] result in smeared images, whereas our algorithm focuses the ship a little bit better. However, the onboard belt unloading system is still hard to identify in our reconstruction. The numerical results in Tab. 4.6 confirm the slight quality improvement in terms of peak power, image contrast and entropy using our method.

We want to point out that the results of all autofocus algorithms depend on the length of the used CPI and on its starting position inside the entire observation time. Both parameters determine indirectly how non-linear the motion of the ship is inside the CPI.

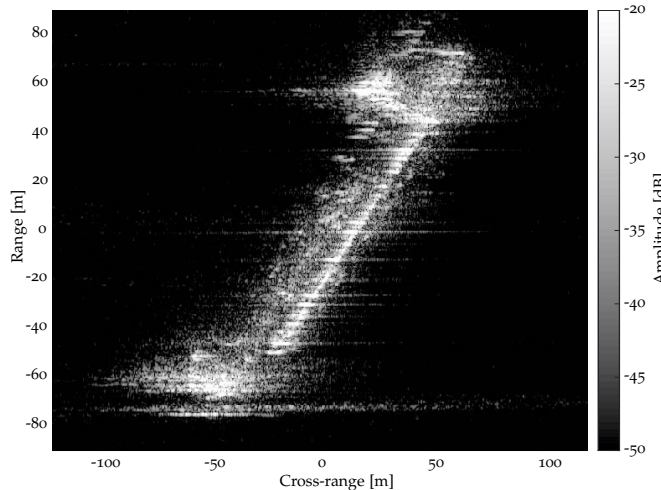


Figure 4.16: Result of a self discharging bulk carrier at speed 5.6 m/s from case study C using the ICBT autofocus by Martorella et al. [MBH05].

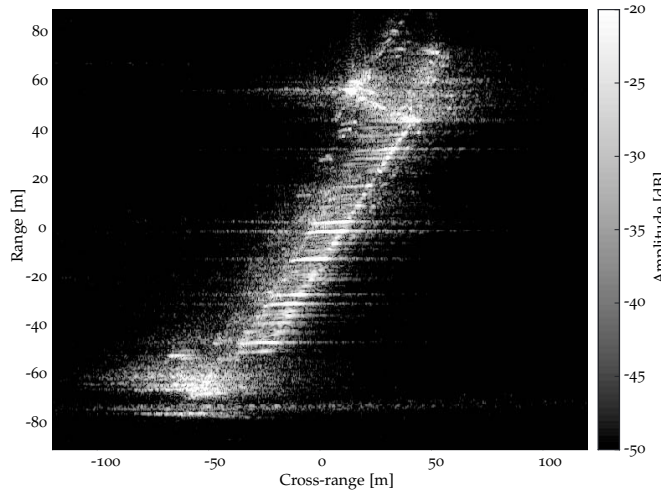


Figure 4.17: Result of a self discharging bulk carrier at speed 5.6 m/s from case study C using the backprojection autofocus by Ash [Ash12].

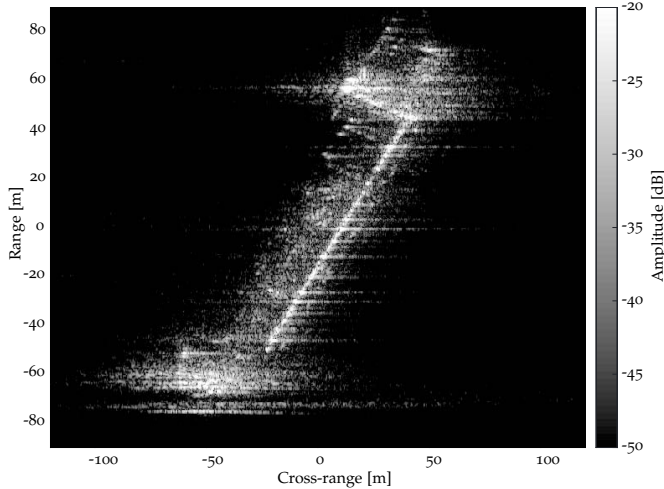


Figure 4.18: Result of a self discharging bulk carrier at speed 5.6 m/s from case study C using our proposed autofocus.

Table 4.6: Numerical results of case study C (self discharging bulk carrier).

	No	ICBT	Ash	Ours
Peak Power	233	798	962	1126
Contrast	1.90	3.26	2.99	3.27
Entropy	10.66	8.89	9.15	8.49
Costs (norm.)	1	—	3.17	1.43

Thus, both parameters have a large impact on the image quality, which means that they have to be chosen carefully. In order to prove this, we reconstructed several SAR images of the ship from this case study using different CPI lengths and different CPI intervals. In the following two figures, we present the results using those parameters, which lead to the highest image contrast. The reconstructed images from a badly chosen CPI interval and the results of an optimal chosen CPI interval are shown in Fig. 4.19 and 4.20. In both cases, we use an empirically determined optimal CPI length of 5 s, which leads to a peak power of 418, a contrast of 2.60 and an entropy of 9.06 for the not perfectly focused image in Fig. 4.19. The well-focused image in Fig. 4.20 has a peak power of 1507, a contrast of 3.54 and an entropy of 8.33. The different shapes of the same ship in Fig. 4.19 and 4.20 are caused by the different motions during the chosen CPI intervals.

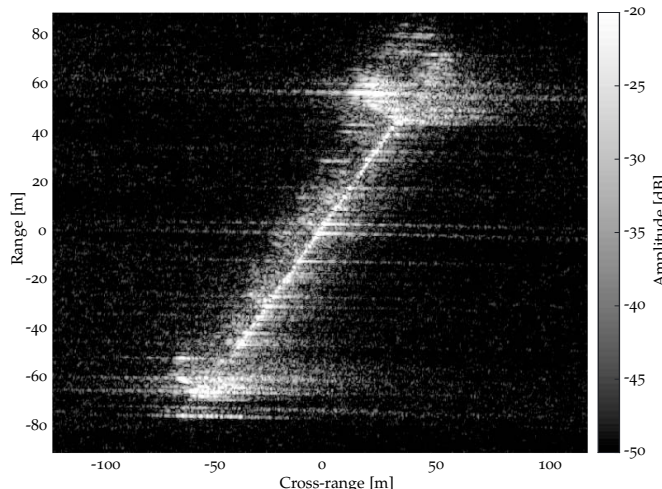


Figure 4.19: Results of our autofocus using a badly chosen CPI.

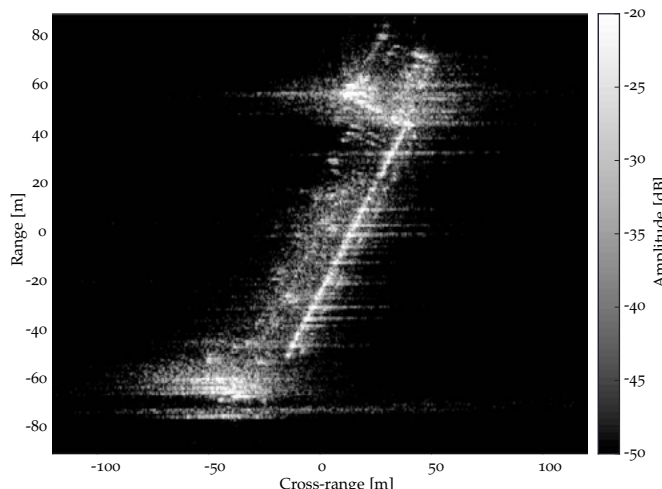


Figure 4.20: Results of our autofocus using a well chosen CPI.

Limits of the Proposed Autofocus Algorithm of Large Ships

Our algorithm leads to a perfectly focused SAR image of a moving ship if the shape of the ship is almost planar. This is mostly true for large ships longer than approximately 150 m. However, the superstructures, for example at the front and the back of a large ship, have different motions than the deck. Since only the motions of the main planar part, the deck, is estimated by the proposed algorithm, superstructures are displayed smeared. Hence, small ships like fishing boats or tugboats, which are not planar objects, would appear unfocused in most cases. The following applies: the smaller the ship and the higher the waves, the more non-linear is its motion. Additionally, the smaller the ship, the less significant reflectors are visible in the corresponding SAR image, which makes the autofocus problem more complex.

4.7.4 *Autofocus of a Static Scene with Low-Cost INS*

Finally, we show that our proposed ship autofocus algorithm is not only able to focus non-linearly moving ships automatically. It is also able to focus static scenes in high quality automatically even if a low-cost INS sensor is used, which measures the flight path coarsely. State-of-the-art autofocus techniques do not offer the possibility to use a low-cost INS instead of an expensive high-quality INS sensor. We show the validity of this statement again based on the *SmartRadar* data [Kir+16] and the geometry from the experimental data in Sec. 2.6 and in Sec. 3.7.

Usually, state-of-the-art autofocus techniques are only able to correct antenna position errors of up to approximately one-half of the range-resolution, which is in our case roughly 12 cm for a 660 MHz chirp bandwidth. Larger antenna position errors would reduce the image quality and could cause ghost targets due to ambiguities. To show the effectiveness of our autofocus algorithm, we generate an artificial approximated flight path from the originally measured flight path and evaluate our proposed ship autofocus algorithm and the backprojection autofocus algorithm by Ash [Ash12] using the approximated flight path. We generate an artificial horizontal antenna position error of a quadratic drift, which has an increasing deviation to the original flight path of more than 3 m since the real measured flight path is almost accurate. This 3 m drift is typical for much cheaper and less accurate low-cost INS sensors [DL13]. The approximated flight path is composed of the original flight path and the added antenna position errors. Fig. 4.21 shows the top view of both flight paths. The approximated flight path is visualized as a red dashed curve and the original flight path is depicted by a blue solid curve. The

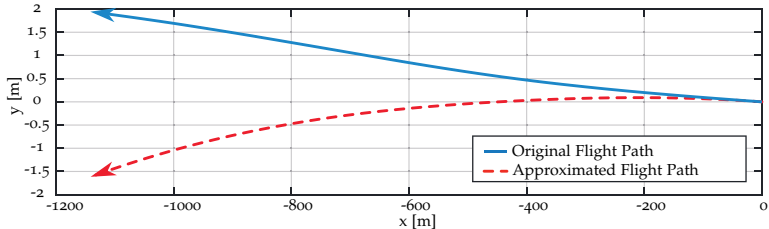


Figure 4.21: Original (blue solid) and approximated (red dashed) flight path. The antenna position error is maximal 4 m in y -direction.

approximated flight path is only similar to the original flight path at the beginning of the flight.

We initialize the GBP reconstruction by an image grid of $8\,192 \times 8\,192$ pixels, where each pixel has a spacing of approximately 9 cm in each dimension. In this example, we use 20×20 subareas. We process 8 192 range profiles from an observation time of approximately 10 s to get high azimuth resolution and use the data from the first 0.6 s to reconstruct the initial image, before we start our integrated autofocus, explained in Sec. 4.6.

The original image, reconstructed from the real data [Kir+16] as well as the original flight path using the GBP algorithm and the backprojection autofocus by Ash [Ash12] is shown in Fig. 4.22. This figure is identical to Fig. 2.14 in Sec. 2.6. A sewage treatment plant, some fields, a few houses and some parking cars can clearly be seen in the focused image. This original image is treated as the reference image. Furthermore, using the approximated flight path instead of the original one and no autofocus technique leads to the image in Fig. 4.23. This image is completely smeared and useless for image interpretation tasks. The results of the GBP algorithm in combination with the backprojection autofocus by Ash [Ash12] using the approximated flight path is shown in Fig. 4.24. This image shows in principle the same scene as the reference image in Fig. 4.22, but it is smeared and overlayed by noise. The reason is that the assumption of a maximal antenna position error of one-half of the range-resolution, here 12 cm, does not hold in this scenario. On the contrary, our proposed autofocus algorithm is able to correct antenna position errors much larger than 12 cm and leads to the well-focused image presented in Fig. 4.25. From a visual point of view, the image is much better focused than the state-of-the-art reconstruction and as good as the original image. However, the entire image is shifted by a few pixels in azimuth and not visibly scaled. The reason is that the approximated

flight path in the first 0.6 s has a marginally different direction and a marginally different curvature than the original flight path. This shifts and scales the image. In summary, our reconstructed image in Fig. 4.25 is much better focused than the image in Fig. 4.24 reconstructed by the state-of-the-art backprojection autofocus by Ash [Ash12].

This is confirmed by the numerical results presented in Tab. 4.7. The reconstructed image using our ship autofocus algorithm leads to a similar peak power, a similar image contrast and a similar image entropy as the reference image. Besides that, it is much better focused than the image reconstructed by the backprojection autofocus by Ash [Ash12]. This shows that our proposed ship autofocus algorithm is able to focus SAR image in high quality from extreme coarsely measured flight paths, such that it enables the usage of low-cost INS sensors instead of high precision systems to reduce costs and weight of the INS for example in the case of UAV–SAR applications.

Table 4.7: Numerical results of case study D.

	Reference	No	Ash	Ours
Peak Power	2 753	183	1 487	2 724
Contrast	1.35	0.92	1.21	1.33
Entropy	14.01	16.24	14.95	14.07

The computational time of the GBP algorithm was 11 h and 40 min on our 3.6 GHz 8-Core processor with 64 GB RAM work station. The Ash autofocus needed additionally 26 h and 5 min resulting in the total costs of 37 h and 45 min. Our proposed autofocus was much faster and took only 2 h and 50 min and thus in total 14 h and 30 min.

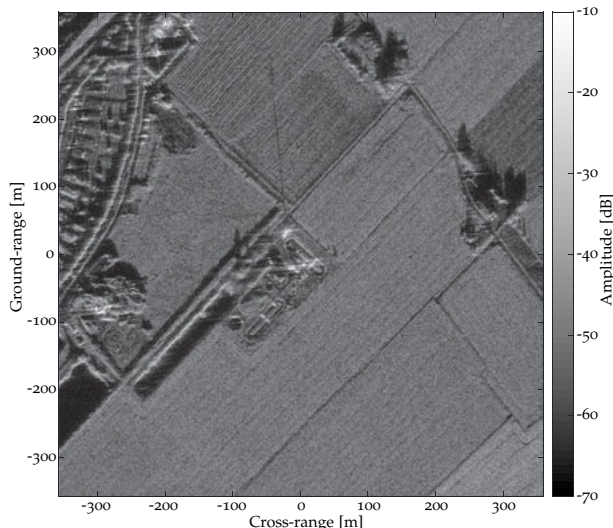


Figure 4.22: Original image of case study D using the original flight path.

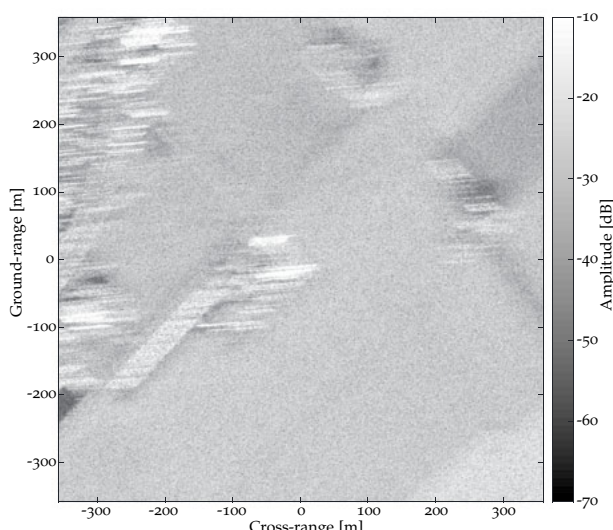


Figure 4.23: Result of case study D without any autofocus technique using the approximated flight path.

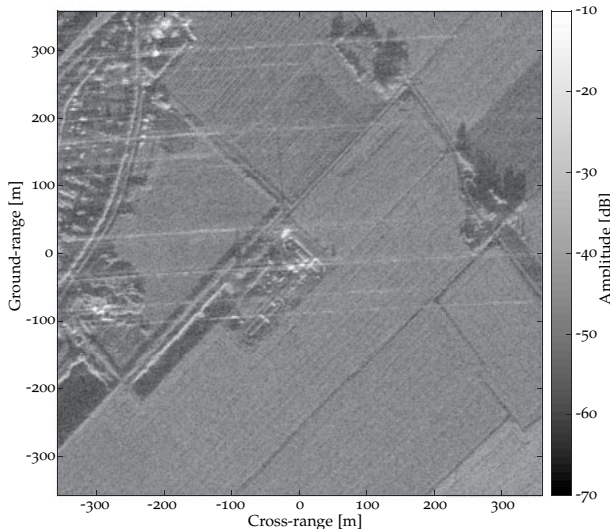


Figure 4.24: Result of case study D using the backprojection autofocus technique by Ash [Ash12] and the approximated flight path.

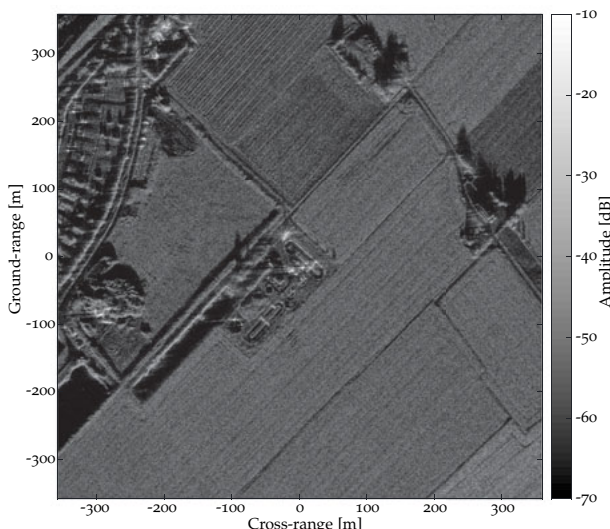


Figure 4.25: Result of case study D using our proposed autofocus technique and the approximated straight flight path.

5

CONCLUSIONS

A major long term goal of the research in maritime surveillance is the development of an autofocus algorithm of ships, which computes high-quality *synthetic aperture radar* (SAR) images on board of an *unmanned aerial vehicle* (UAV). To be precise, this goal consists of two interim goals, which have been attained in this thesis. The first one is the generation of high-resolution SAR images of the illuminated area as fast as possible on board of a small airplane or an UAV. This image is used to detect all ships in the scene and to estimate their locations. The second goal is the generation of high-quality and high-resolution SAR images of each ship individually and robustly for all sea states. We tackled both problems in this thesis by using the *fast factorized backprojection* (FBP) algorithm for the fast image reconstruction and by proposing an extended autofocus technique based on pulse-by-pulse image sharpness maximization. In detail, we developed a parameter choice rule, which takes the exact range errors instead of its estimates into account and calculates near-optimal factorization parameters for the FBP algorithm. The calculated parameters lead to the optimal trade-off between image quality and computational costs. We additionally developed an extended autofocus algorithm, which estimates time- and location-depending range errors by maximizing subimage sharpness to focus SAR images of ships with arbitrary motions robustly for all sea states.

The well known FBP algorithm combines similar range profiles iteratively such that the final SAR image is reconstructed from a much smaller number of range profiles. This approach leads to a huge improvement of the computational costs in comparison to the original computational expensive *global backprojection* (GBP) algorithm. However, combining range profiles causes range errors and thus a peak amplitude loss and ghost targets of all objects, which result in a loss of image quality. This loss can be controlled by dividing the image into subimages, which again let the computational effort increase. The question, which is answered by this thesis, is about the configuration of the FBP algorithm. Until today it was not clear which factorization parameters are optimal in order to reach the optimal trade-off between quality and costs.

In this thesis, we analyzed the factorization parameters of the FBP algorithm regarding computational costs and SAR image quality. In order to estimate the image quality more precisely than state-of-the-art methods, we compute the exact range errors, which are the reasons for the image quality loss, instead of estimating them. By taking the exact range errors into account, we were able to include the flight path, the squint angle, the depression angle and the image size as well as the resulting peak amplitude loss and the ghost targets into our image quality estimation. This precise image quality estimation enabled us to analyze the factorization parameters, especially the effects of variable factorization parameters on the image quality and on the computational costs in each stage.

We conclude that the aperture factorization of three or four define the speed-up factor and the image factorization in azimuth in the first stage controls the image quality. All other parameters depend on these two values. Furthermore, we found out that a variable aperture factorization results in a faster computation in comparison to constant factorization parameters. However, the optimal compromise between quality and costs is achieved if the aperture factorization of three or four is piecewise constant with one increasing step. Moreover, the image factorizations in azimuth and in range have to be equal to the aperture factorizations in each stage except the first one. The first stage has a specific objective. It is essential for reducing the range errors since an error in the first stage cannot be corrected in the subsequent stages. Hence, the azimuth image factorization in the first stage controls the image quality. The image factorization in range ensures in general that the range errors in all azimuth lines are almost equal. In the first stage, the range image factorization defines the dimensions of the subimages. Both image factorizations in azimuth and in range in the first stage have to be adjusted to the size of the SAR image. The optimal number of stages depends on the aperture factorizations. The aperture factorization of three requires, for example, five stages and the aperture factorization of four requires four stages. However, the more stages are used, the larger are the accumulated range errors and the lower is the image quality.

We summarized the results of our analysis in a parameter choice rule and evaluated it using a real data airborne X-band example. The evaluation showed that a variable factorization of $F_{apt} = (3, 3, 3, 4, 4)$, $F_{img}^{az} = (4, 3, 3, 4, 4)$ and $F_{img}^{rg} = (1, 3, 3, 4, 4)$ result in a theoretical speed-up of 196 in comparison to the GBP algorithm, where the true maximal relative image error is only 0.054.

Our analysis clarified the effects of the factorization parameters on the costs and on the quality in the framework of the FBP algorithm. We showed how these parameters have to be configured a-priory to

get near-optimal results. The results of this thesis enable a fast SAR image reconstruction onboard of UAVs using the optimal configured FBP algorithm. By only adjusting the number of pixels as well as the pixel size and the factorization parameters, large SAR images with arbitrary resolution and arbitrary quality can be reconstructed by the FBP algorithm onboard of UAVs. This flexibility is a major advantage of the usage of the FBP algorithm on UAVs, which are usually vulnerable to wind gusts. SAR on UAVs might be an interesting civil or military application in maritime surveillance since it enables a fast reaction time in order to monitor wide areas of the open sea and to reconstruct SAR image of landscapes.

Moreover, if a SAR image of the open sea has been reconstructed, for example by the optimal configured FBP algorithm, usually most of the ships appear smeared, shifted and deformed in the image. The reason is their non-linear motion during the long observation time of several seconds, which is influenced by their tracks as well as by their velocities and by the current sea waves. Indeed, based on the SAR image, all ships can be detected, for example, by the *constant false alarm rate* (CFAR) detector and a local image of each ship can be computed individually. However, the ship type can still not be identified reliably. State-of-the-art autofocus techniques are only successful, either if a short *coherent processing interval* (CPI) is used, which leads to reduced azimuth resolution, or if the sea is almost flat. Until today, no state-of-the-art autofocus technique was able to focus arbitrarily moving and maneuvering ships in high-quality using a long CPI for all sea states robustly.

In this thesis, we proposed an extended autofocus approach, which reconstructs high-quality SAR images of large arbitrarily moving and maneuvering ships robustly for all sea states and a long CPI of several seconds. By simulating synthetic data of a moving tanker including translations, rotations and deformations, we confirmed that a non-linear motion leads to a smeared, a shifted and a deformed SAR image. The results show that its radial velocity causes a shift in azimuth and its radial acceleration leads to a smearing. Since ships are large objects, both kinds of motion are always present such that a SAR image deformation occurs additionally to the small deformation of the real ship. The reason is that each part of the ship has a different radial motion and thus a different shift in azimuth. Hence, the size of a ship in a SAR image usually does not coincide with the real size of the ship. Theoretically, if the motion of a ship is known exactly, it can be included in the GBP algorithm such that a perfectly focused SAR image can be reconstructed. However, superstructures like the driver's cabins are still smeared. Since this motion is unknown in reality, it has to be estimated. Our proposed autofocus algorithm of large ships estimates the arbitrary motion of a ship such

that we are able to generate sharp SAR images. The algorithm divides the image into subimages and estimates pulse-by-pulse a phase error of each subimage separately by maximizing subimage sharpness. These estimated phase errors are forced to be smooth using an iterative Gauss-Newton regularization framework. The computed subimage phase errors are interpolated to all pixels by quadratic polynomial regression such that multidimensional phase error functions, i.e., time-dependent and location-dependent phase errors, can be estimated by our algorithm. We propose to use these estimated phases of each pixel of the currently considered pulse to correct the range distances from all subsequent aperture positions to all pixels such that no limitations and no assumptions on the motions of the ships have to be made.

The effectiveness of the proposed autofocus algorithm has been proven by real experimental data from an airborne single-channel X-band SAR system. The results show that our algorithm improves the image quality of a focused ship significantly in terms of peak power, image contrast and image entropy in all considered case studies. The additional computational effort of our autofocus technique is negligible compared to the costs of the GBP itself. We showed in our experiments that for a CPI of for example 4s the ship can be treated as a rigid moving object in many cases. However, compensating for the deformations of the ship instead of treating the ship as a rigid object yields a little bit better results. In summary, our autofocus algorithm is able to reconstruct sharp images of moving ships, where the bollards on the deck can be counted. In the same scenario, state-of-the-art algorithms generate images, where the type of the ship cannot be identified.

The proposed autofocus algorithm of large moving ships is important since usually the SAR image quality of arbitrarily moving ships does not provide the necessary quality for classification tasks. Human operators are in most cases not sure, which type of a ship is visible in the SAR image. However, especially SAR is well suited for the application of identifying the type of ships on the open sea, since it provides wide-area coverage in high-resolution independently of weather conditions or daytime. Of particular interest are maritime surveillance applications using UAVs, since human operators on board of a ship could safely use drones to check their surroundings in all weather conditions. To conclude, our technique might enable an automatic ship classification based on SAR images and thus an *automatic identification system* (AIS) verification in the future.

This work increases the body of knowledge in maritime SAR. The factorization parameters of the FBP algorithm have been analyzed as well as optimized by considering exact range errors and the autofocus of

large ships with arbitrary motions has been considerably improved. Both topics may be extended in the future in a variety of ways, for example by the following:

We showed in Chap. 3 that a variable aperture factorization for each stage leads to better results regarding computational costs and image quality. However, we set the aperture factorization to be constant for all aperture blocks. A variable aperture factorization in each block might improve the results further because the aperture factorization depends on the instantaneous radial image width and thus on the instantaneous squint angle, which varies from block to block. Moreover, a variable subimage size might also lead to improved image quality, since the range errors are larger at the boundary of the SAR image than at its center. Hence, large subimages in the middle of the image and small subimage at its boundaries might reduce the range error further and thus might improve the image quality.

Furthermore, we suggested in Chap. 4 that the choice of the CPI within the observation time is very important for the resulting SAR image quality. Let us, for example, consider sinusoidally rotations of a ship on a rough sea with high waves. Then, time intervals exist, where the motion of the ship is less non-linear than during other time intervals. Of course, an operator could watch a sequence of SAR images to identify the one, where the type of the ship can clearly be identified. However, optimizing the CPI parameter automatically and supporting the human operator by a confidence value or by automatic detection of those images with the highest quality might improve the reliability of the image interpretation.

In Chap. 4 we showed by synthetic and by real data that the proposed ship autofocus technique, which treats the ship as a two-dimensional object, works excellent for large ships. However, driver's cabins and masts are still smeared due to their different motion in comparison to the main parts of the ships, the decks. To focus these superstructures, or even to focus small ships like fishing boats, which consist only of superstructures, the three-dimensional shapes of the ships should be taken into account. This challenging problem might be solved by using multi-channel SAR systems.

Finally, we designed in Chap. 4 our proposed ship autofocus algorithm in a way that it uses subimages in order to estimate the non-linear motion of a ship. The image of the ship is nevertheless reconstructed by the computational expensive GBP algorithm. However, the FBP algorithm, presented in Chap. 3, uses subimages in a similar way. A combination of both, using the FBP algorithm for the SAR image reconstruction of a single ship might improve the computational effort of our ship autofocus algorithm.

A

APPENDIX

This appendix proofs that Eq. (2.18) is equivalent to Eq. (2.19). In general, equivalent equations have the same solution. The advantage of solving Eq. (2.19) instead of Eq. (2.18) is that the equation has no complex values. This proof is a detailed version of the proof done by Ash [Ash12]. We proof that the equation

$$S(\phi_m^\epsilon) = \sum_{i=1}^{N_{\text{pix}}} |\mathcal{R}(x_i, \phi_m^\epsilon) \mathcal{R}^*(x_i, \phi_m^\epsilon)|^2 \quad (\text{A.1})$$

is equivalent to

$$S(\phi_m^\epsilon) = \|\mathbf{a}_m \cos(\phi_m^\epsilon) + \mathbf{b}_m \sin(\phi_m^\epsilon) + \mathbf{v}_m\|^2 \quad (\text{A.2})$$

for $\phi_m^\epsilon \in (-\pi, \pi]$. The function $S : (-\pi, \pi] \rightarrow \mathbb{R}_+$ is the *image sharpness* cost function depending on the m th phase error ϕ_m^ϵ . In Eq. (A.1), the sharpness S is computed by the sum of all reflectivity values $\mathcal{R}(x_i, \phi_m^\epsilon) \in \mathbb{C}$ to the power of four, for all $i = 1, \dots, N_{\text{pix}}$ pixel located at $x_i \in \mathbb{R}^3$. In Eq. (A.2), the sharpness S is computed by the Euclidean norm of vectors $\mathbf{a}_m, \mathbf{b}_m, \mathbf{v}_m \in \mathbb{R}^{N_{\text{pix}}}$ to the power of two. In order to proof the equivalence for a fixed and arbitrary m , the reflectivity \mathcal{R} can be decomposed into

$$\begin{aligned} \mathcal{R}(x_i, \phi_m^\epsilon) &= \sum_{j=1}^M \hat{b}_j(x_i) \exp(-i\phi_j^\epsilon) \\ &= \underbrace{\sum_{\substack{j=1 \\ j \neq m}}^M \hat{b}_j(x_i) \exp(-i\phi_j^\epsilon)}_{=: \mathcal{R}_m^C(x_i)} + \hat{b}_m(x_i) \exp(-i\phi_m^\epsilon), \end{aligned} \quad (\text{A.3})$$

where M is the number of slow-time samples and \hat{b}_j the j th backprojected range profile in high-frequency band. This decomposition is useful since the phases $(\phi_1^\epsilon, \dots, \phi_{m-1}^\epsilon, \phi_{m+1}^\epsilon, \dots, \phi_M^\epsilon)$ are fixed and known. Only the phase error ϕ_m^ϵ is variable. The image \mathcal{R}_m^C is basically the phase corrected reflectivity image without pulse m . The term \mathcal{R}_m represents the reflectivity at the image grid, backprojected only from the data of pulse m

without any phase correction. The decomposition (A.3) including the complement reflectivity \mathcal{R}_m^C , the reflectivity \mathcal{R}_m of the m th range profile and its phase error ϕ_m^ϵ is used to simplify Eq. (A.1) in the following way:

$$\begin{aligned}
 \mathcal{R}(\phi_m^\epsilon, \mathbf{x}_i) \mathcal{R}^*(\phi_m^\epsilon, \mathbf{x}_i) &= (\mathcal{R}_m^C(\mathbf{x}_i) + \mathcal{R}_m(\mathbf{x}_i) \exp(-i\phi_m^\epsilon)) \\
 &\quad \cdot ((\mathcal{R}_m^C)^*(\mathbf{x}_i) + \mathcal{R}_m^*(\mathbf{x}_i) \exp(i\phi_m^\epsilon)) \\
 &= |\mathcal{R}_m^C(\mathbf{x}_i)|^2 + |\mathcal{R}_m(\mathbf{x}_i)|^2 \\
 &\quad + 2 \operatorname{Re}(\mathcal{R}_m^C(\mathbf{x}_i) \mathcal{R}_m^*(\mathbf{x}_i) \exp(i\phi_m^\epsilon)) \\
 &= \underbrace{|\mathcal{R}_m^C(\mathbf{x}_i)|^2 + |\mathcal{R}_m(\mathbf{x}_i)|^2}_{:= v_m^{(i)}} \\
 &\quad + \underbrace{2 \operatorname{Re}(\mathcal{R}_m^C(\mathbf{x}_i) \mathcal{R}_m^*(\mathbf{x}_i)) \cdot \cos(\phi_m^\epsilon)}_{:= a_m^{(i)}} \\
 &\quad + \underbrace{(-2) \operatorname{Im}(\mathcal{R}_m^C(\mathbf{x}_i) \mathcal{R}_m^*(\mathbf{x}_i)) \cdot \sin(\phi_m^\epsilon)}_{:= b_m^{(i)}},
 \end{aligned}$$

where $(\cdot)^*$ is the complex conjugation, $\operatorname{Re}(\cdot)$ gets the real value and $\operatorname{Im}(\cdot)$ gets the imaginary component. Thus, Eq. (A.1) can finally be rewritten by

$$\begin{aligned}
 S(\phi_m^\epsilon) &= \sum_{i=1}^{N_{\text{pix}}} |\mathcal{R}(\mathbf{x}_i, \phi_m^\epsilon) \mathcal{R}^*(\mathbf{x}_i, \phi_m^\epsilon)|^2 \\
 &= \sum_{i=1}^{N_{\text{pix}}} |a_m^{(i)} \cos(\phi_m^\epsilon) + b_m^{(i)} \sin(\phi_m^\epsilon) + v_m^{(i)}|^2 \\
 &= |\mathbf{a}_m \cos(\phi_m^\epsilon) + \mathbf{b}_m \sin(\phi_m^\epsilon) + \mathbf{v}_m|^2 \quad \text{for } \phi_m^\epsilon \in (-\pi, \pi]
 \end{aligned}$$

and the vectors $\mathbf{a}_m = (a_m^{(1)}, \dots, a_m^{(N_{\text{pix}})})^T$, $\mathbf{b}_m = (b_m^{(1)}, \dots, b_m^{(N_{\text{pix}})})^T$ and $\mathbf{v}_m = (v_m^{(1)}, \dots, v_m^{(N_{\text{pix}})})^T$. The parameters $a_m^{(i)}, b_m^{(i)}, v_m^{(i)} \in \mathbb{R}$ are computed for $i = 1, \dots, N_{\text{pix}}$ by

$$\begin{aligned}
 a_m^{(i)} &= 2 \operatorname{Re}(\mathcal{R}_m^C(\mathbf{x}_i) \mathcal{R}_m^*(\mathbf{x}_i)), \\
 b_m^{(i)} &= -2 \operatorname{Im}(\mathcal{R}_m^C(\mathbf{x}_i) \mathcal{R}_m^*(\mathbf{x}_i)), \\
 v_m^{(i)} &= |\mathcal{R}_m^C(\mathbf{x}_i)|^2 + |\mathcal{R}_m(\mathbf{x}_i)|^2.
 \end{aligned} \tag{A.4}$$

This proofs the equivalence of Eq. (A.1) and Eq. (A.2). \square

BIBLIOGRAPHY

[AR14] Mark A. Richards. *Fundamentals of Radar Signal Processing*. 2nd ed. McGraw-Hill Education Ltd, 2014.

[Amuo9] Amundsen. “Fact sheet of amundsen class tanker.” In: <https://www.gbamarine.no/> (2009).

[And88] Lars-Erik Andersson. “On the Determination of a Function from Spherical Averages.” In: *SIAM Journal on Mathematical Analysis* 19.1 (Jan. 1988), pp. 214–232.

[Ash12] J. N. Ash. “An Autofocus Method for Backprojection Imagery in Synthetic Aperture Radar.” In: *IEEE Geoscience and Remote Sensing Letters* 9.1 (Jan. 2012), pp. 104–108.

[BMG16] Fabrizio Berizzi, Marco Martorella, and Elisa Giusti. *Radar Imaging for Maritime Observation*. 1st ed. CRC Press, 2016.

[Ber19] Torsten Bertram. *Fahrerassistenzsysteme 2018*. 1st ed. Springer Vieweg, 2019.

[Bru+11] S. Brusch, S. Lehner, T. Fritz, M. Soccorsi, A. Soloviev, and B. van Schie. “Ship Surveillance With TerraSAR-X.” In: *IEEE Transactions on Geoscience and Remote Sensing* 49.3 (Mar. 2011), pp. 1092–1103.

[CPR91] Ciro Cafforio, Claudio Prati, and Fabio Rocca. “SAR Data Focusing using Seismic Migration Techniques.” In: *IEEE Transactions on Aerospace and Electronic Systems* 27.2 (Apr. 1991), pp. 194–207.

[CGM95] Walter G. Carrara, Ron S. Goodman, and Ronald M. Majewski. *Spotlight Synthetic Aperture Radar: Signal Processing Algorithms*. Boston: Artech House, 1995.

[Cha+19] Yang-Lang Chang, Amare Anagaw, Lena Chang, Yi Chun Wang, Chih-Yu Hsiao, and Wei-Hong Lee. “Ship Detection Based on YOLOv2 for SAR Imagery.” In: *Remote Sensing* 11.7 (Apr. 2019), p. 786.

[CBo9] Margaret Cheney and Brett Borden. *Fundamentals of radar imaging*. Philadelphia: Society for Industrial and Applied Mathematics (SIAM), 2009.

[Cho+17] Fabian Cholewa, Matthias Wielage, Peter Pirsch, and Holger Blume. "Synthetic Aperture Radar with Fast Factorized Back-projection: A Scalable, Platform Independent Architecture for Exhaustive FPGA Resource Utilization." In: *International Conference on Radar Systems (Radar)*. Oct. 2017, pp. 1–6.

[CW05] I. A. Cumming and F. H. Wong. *Digital Processing of Synthetic Aperture Radar Data - Algorithms and Implementation*. 1st ed. Artech House, Boston, 2005.

[DBM16] Armin Doerry, Edward E. Bishop, and John A. Miller. *Basics of Backprojection Algorithm for Processing Synthetic Aperture Radar Images*. Tech. rep. Sandia National Laboratories, Feb. 2016.

[DL13] Michael I. Duersch and David G. Long. "Backprojection Autofocus for Synthetic Aperture Radar." In: *2010 International WaterSide Security Conference*. 2013.

[Faw85] John A. Fawcett. "Inversion of N-Dimensional Spherical Averages." In: *SIAM Journal on Applied Mathematics* 45.2 (Apr. 1985), pp. 336–341.

[FM03] J. R. Fienup and J. J. Miller. "Aberration correction by maximizing generalized sharpness metrics." In: *Journal of the Optical Society of America. A, Optics, Image Science, and Vision* 20.4 (Apr. 2003), pp. 609–620.

[FUo06] Per-Olov Frolind and Lars M. H. Ulander. "Evaluation of angular interpolation kernels in fast back-projection SAR processing." In: *IEE Proceedings - Radar, Sonar and Navigation* 153.3 (June 2006), pp. 243–249.

[GM10] Leroy A. Gorham and Linda J. Moore. "SAR image formation toolbox for MATLAB." In: *Proceedings of SPIE - The International Society for Optical Engineering* 7699 (Apr. 2010).

[HEGJJ89] P. H. Eichel, D. C. Ghiglia, and C. V. Jakowatz Jr. "Speckle Processing Method for Synthetic Aperture Radar Phase Correction." In: *Optics Letters* 14.1 (Jan. 1989), pp. 1–3.

[Han+10] T. N. Hannevik, Ø. Olsen, A. N. Skauen, and R. Olsen. "Ship detection using high resolution satellite imagery and space-based AIS." In: *2010 International WaterSide Security Conference*. Nov. 2010, pp. 1–6.

[Her87] Heinrich Hertz. "Ueber sehr schnelle electrische Schwingungen." In: *Annalen der Physik* 267.7 (1887), pp. 421–448.

[Hüo4a] Christian Hülsmeyer. *Verfahren, um entfernte metallische Gegenstände mittels elektrischer Wellen einem Beobachter zu melden.* Patentiert im Deutschen Reiche DE165546. Apr. 30. 1904.

[Hüo4b] Christian Hülsmeyer. *Verfahren zur Bestimmung der Entfernung von metallischen Gegenständen (Schiffen o. dgl.), deren Gegenwert durch das Verfahren nach Patent 165546 festgestellt wird.* Patentiert im Deutschen Reiche DE169154. Nov. 1. 1904.

[Kir+16] M. Kirscht, J. Mietzner, B. Bickert, A. Dallinger, J. Hippler, J. Meyer-Hilberg, R. Zahn, and J. Boukamp. "An Airborne Radar Sensor for Maritime and Ground Surveillance and Reconnaissance—Algorithmic Issues and Exemplary Results." In: *IEEE Journal of Selected Topics in Applied Earth Observations and Remote Sensing* 9.3 (Mar. 2016), pp. 971–979.

[KH99] Helmut Klausing and Wolfgang Holpp. *Radar mit realer und synthetischer Apertur.* 1st ed. De Gruyter Oldenbourg, 1999.

[LDC14] C. Livingstone, M. Dragosevic, and S. Chu. *Ship detection and measurement of ship motion by multi-aperture Synthetic Aperture Radar.* Tech. rep. Defence Research and Development, June 2014.

[MS+09] Steven M. Scarborough, Curtis H. Casteel Jr, Leroy Gorham, Michael J. Minardi, Uttam Majumder, Matthew G. Judge, Ed Zelnio, Michael Bryant, Howard Nichols, and Douglas Page. "A challenge problem for SAR-based GMTI in urban environments." In: *Proc. SPIE - The International Society for Optical Engineering* 7337 (May 2009), pp. 7337–7347.

[MS81] C. E. Mancill and J. M. Swiger. "A Mapdrift Autofocus Technique for Correcting Higher Order SAR Phase Errors." In: *27th Annual Tri-Service Radar Symposium Record.* 1981, pp. 391–400.

[MM93] Antonio Martinez and Jean L. Marchand. "SAR Image Quality Assessment." In: *Revista de teledetección* (1993).

[MBH05] M. Martorella, F. Berizzi, and B. Haywood. "Contrast Maximisation based Technique for 2-D ISAR Autofocusing." In: *IEE Proceedings - Radar, Sonar and Navigation* 152.4 (Aug. 2005), pp. 253–262.

[Max61] James C. Maxwell. "On Physical Lines of Force." In: *Philosophical Magazine* 21 & 23.4 (Mar. 1861), pp. 161–175.

[MR96] John W. McCorkle and Martin Rofheart. "An Order $N^2 \log(N)$ Backprojection Algorithm for Focusing wide-angle wide-bandwidth arbitrary-motion Synthetic Aperture Radar." In: *In SPIE AeroSense Conference*. Vol. 2747. Orlando, Florida, Apr. 1996, pp. 25–36.

[Mcm+09] Douglas McMakin, Paul Keller, David M. Sheen, and Thomas Hall. "Dual-surface dielectric depth detector for holographic millimeter-wave security scanners." In: *Proceedings of SPIE - The International Society for Optical Engineering* 7309 (May 2009).

[Nato01] Frank Natterer. *The Mathematics of Computerized Tomography*. 2nd ed. Society for Industrial and Applied Mathematics (SIAM), June 2001, p. 222.

[NA13] Minh Phuong Nguyen and Samer Ben Ammar. "Second Order Motion Compensation for Squinted Spotlight Synthetic Aperture Radar." In: *Asia-Pacific Conference on Synthetic Aperture Radar (APSAR)*. Tsukuba, Japan, Sept. 2013, pp. 202–205.

[Nil97] Stefan Nilsson. "Application of Fast Backprojection Techniques for some Inverse Problems of Integral Geometry." Dissertations No. 499. PhD thesis. Department of Mathematics, Linköping University, Sweden, 1997.

[NFM15] C. Noviello, G. Fornaro, and M. Martorella. "Focused SAR Image Formation of Moving Targets Based on Doppler Parameter Estimation." In: *IEEE Transactions on Geoscience and Remote Sensing* 53.6 (June 2015), pp. 3460–3470.

[PLG10] Rafael Paes, Joao Lorenzzetti, and Douglas Gherardi. "Ship detection using terra-SAR-X images in the Campos Basin (Brazil)." In: *IEEE Geoscience and Remote Sensing Letters* 7 (July 2010), pp. 545–548.

[Pfi+13] M. Pfitzner, F. Cholewa, P. Pirsch, and H. Blume. "FPGA based architecture for real-time SAR processing with integrated motion compensation." In: *Conference Proceedings of 2013 Asia-Pacific Conference on Synthetic Aperture Radar (APSAR)*. Sept. 2013, pp. 521–524.

[Rib12] Angel Ribalta. "Optimizing the Factorisation Parameters in the Fast Factorized Backprojection Algorithm." In: *9th European Conference on Synthetic Aperture Radar (EUSAR)*. Nürnberg, Germany: VDE, Apr. 2012.

[RZ19] Alexander V. Ryzhkov and Dusan S. Zrnic. *Radar Polarimetry for Weather Observations*. 1st ed. Springer International Publishing, 2019.

[Sch14] Michael Schuster. "Collision Avoidance for Vessels Using a Low-Cost Radar Sensor." In: *IFAC Proceedings Volumes* 47.3 (2014), pp. 9673–9678.

[SHH98] O. Seger, M. Herberthson, and H. Hellsten. "Real-time SAR Processing of low Frequency ultra wide band Radar Data." In: *2nd European Conference on Synthetic Aperture Radar (EUSAR)*. Friedrichshafen, Germany, May 1998, pp. 489–492.

[SNO15] Aron Sommer, Minh P. Nguyen, and Jörn Ostermann. "Comparison of Omega-K and backprojection regarding spatial resolution for squinted spotlight SAR with motion errors." In: *IEEE 5th Asia-Pacific Conference on Synthetic Aperture Radar (APSAR)*. Singapore, Singapore, Sept. 2015, pp. 143–147.

[SO18] Aron Sommer and Jörn Ostermann. "Backprojection Autofocus of Moving Ships for Synthetic Aperture Radar." In: *IEEE 15th European Radar Conference (EuRAD)*. Sept. 2018, pp. 146–149.

[SO19] Aron Sommer and Jörn Ostermann. "Backprojection Subimage Autofocus of Moving Ships for Synthetic Aperture Radar." In: *IEEE Transactions on Geoscience and Remote Sensing* 57.11 (Nov. 2019), pp. 8383–8393.

[SO16] Aron Sommer and Jörn Ostermann. "Explicit Motion Compensation for Backprojection in Spotlight SAR." In: *17th International Radar Symposium (IRS)*. Krakow, Poland, May 2016, pp. 1–4.

[Sou96] M. Soumekh. "Reconnaissance with slant plane circular SAR imaging." In: *IEEE Transactions on Image Processing* 5.8 (Aug. 1996), pp. 1252–1265.

[Sti+14] George W. Stimson, Hugh D. Griffiths, Chris J. Baker, and Dave Adamy. *Stimson's Introduction to Airborne Radar*. 3rd ed. SciTech Publishing Inc, 2014, p. 774.

[UHS03] L. M. H. Ulander, H. Hellsten, and G. Stenstrom. "Synthetic-aperture radar processing using fast factorised back-projection." In: *IEEE Transactions on Aerospace and Electronic Systems* 39.3 (July 2003), pp. 760–776.

- [WD12] Armin W. Doerry. "What Maritime ISAR Designers should know about Ship Dynamics." In: *Proc. SPIE Radar Sensor Technology XVI* 8361.2 (May 2012), pp. 194–207.
- [Wat18] Simon Watts. *Airborne Maritime Surveillance Radar, Volume 1*. 1st ed. 2053-2571. Morgan and Claypool Publishers, 2018.
- [Wer+90] S. Werness, W. Carrara, L. Joyce, and D. Franczak. "Moving Target Imaging Algorithm for SAR Data." In: *IEEE Transactions on Aerospace and Electronic Systems* 26.1 (Jan. 1990), pp. 57–67.
- [Wes+18] Birgit Wessel, Martin Huber, Christian Wohlfart, Ursula Marschalk, Detlev Kosmann, and Achim Roth. "Accuracy assessment of the global TanDEM-X Digital Elevation Model with GPS data." In: *ISPRS Journal of Photogrammetry and Remote Sensing* 139.4 (May 2018), pp. 171–182.
- [Wie19] Matthias Wielage. *Design Space Exploration von Architekturen zur echtzeitfähigen Implementierung schneller Backprojection-Verfahren*. 1st ed. Dr. Hut Verlag, 2019.
- [Yeg99] Ali F. Yegulalp. "Fast Backprojection Algorithm for Synthetic Aperture Radar." In: *1999 IEEE Radar Conference*. Waltham, MA, USA, Apr. 1999, pp. 60–65.
- [Zha+18] M. Zhao, T. Li, M. A. Alsheikh, Y. Tian, H. Zhao, A. Torralba, and D. Katabi. "Through-Wall Human Pose Estimation Using Radio Signals." In: *2018 IEEE/CVF Conference on Computer Vision and Pattern Recognition*. June 2018, pp. 7356–7365.

Aron SOMMER

PERSONAL DATA

YEAR OF BIRTH: 1986

PLACE OF BIRTH: Berlin, Germany

EMAIL: sommer@tnt.uni-hannover.de

WORK EXPERIENCE

Current RESEARCH ASSOCIATE at the **Leibniz University Hannover**, Germany,

Institut für Informationsverarbeitung,

MAIN FOCUS: Electrical Engineering, Computer Science and Radar,

THESIS: "Backprojection Autofocus of Large Ships with Arbitrary Motion for Synthetic Aperture Radar" | Advisor: Prof. Dr.-Ing. Jörn OSTERMANN

EDUCATION

APR 2013 Diploma in **TECHNOMATHEMATICS**, DIPL.-MATH. TECHN., **Karlsruhe Institute of Technology – KIT**, Karlsruhe, Germany,

Institute of Applied and Numerical Mathematics,

MAIN FOCUS: Analysis, Numerical Analysis, Communication Engineering and Applied Computer Science,

THESIS: "Passive Airborne Oil Exploration – Theory and Numerical Analysis of a Linear Inverse Problem" | Advisor: Prof. Dr. Andreas HELFRICH-SCHKARBANENKO

JUNE 2006 HIGHER EDUCATION ENTRANCE QUALIFICATION, **Gymnasium Ganderkesee**, Germany

Werden Sie Autor im VDI Verlag!

Publizieren Sie
in „Fortschritt-
Berichte VDI“



Veröffentlichen Sie die Ergebnisse Ihrer interdisziplinären technikorientierten Spitzenforschung in der renommierten Schriftenreihe **Fortschritt-Berichte VDI**. Ihre Dissertationen, Habilitationen und Forschungsberichte sind hier bestens platziert:

- **Kompetente Beratung und editorische Betreuung**
- **Vergabe einer ISBN-Nr.**
- **Verbreitung der Publikation im Buchhandel**
- **Wissenschaftliches Ansehen der Reihe Fortschritt-Berichte VDI**
- **Veröffentlichung mit Nähe zum VDI**
- **Zitierfähigkeit durch Aufnahme in einschlägige Bibliographien**
- **Präsenz in Fach-, Uni- und Landesbibliotheken**
- **Schnelle, einfache und kostengünstige Abwicklung**

PROFITIEREN SIE VON UNSEREM RENOMMEE!
www.vdi-nachrichten.com/autorwerden

VDI verlag

Die Reihen der Fortschritt-Berichte VDI:

- 1 Konstruktionstechnik/Maschinenelemente
- 2 Fertigungstechnik
- 3 Verfahrenstechnik
- 4 Bauingenieurwesen
- 5 Grund- und Werkstoffe/Kunststoffe
- 6 Energietechnik
- 7 Strömungstechnik
- 8 Mess-, Steuerungs- und Regelungstechnik
- 9 Elektronik/Mikro- und Nanotechnik
- 10 Informatik/Kommunikation
- 11 Schwingungstechnik
- 12 Verkehrstechnik/Fahrzeugtechnik
- 13 Fördertechnik/Logistik
- 14 Landtechnik/Lebensmitteltechnik
- 15 Umwelttechnik
- 16 Technik und Wirtschaft
- 17 Biotechnik/Medizintechnik
- 18 Mechanik/Bruchmechanik
- 19 Wärmetechnik/Kältetechnik
- 20 Rechnerunterstützte Verfahren (CAD, CAM, CAE CAQ, CIM ...)
- 21 Elektrotechnik
- 22 Mensch-Maschine-Systeme
- 23 Technische Gebäudeausrüstung

ISBN 978-3-18-386710-3